UNIVERSITAT DE BARCELONA

Exploring the Universe with Quasar Absorption Spectra: correlations among tracers of the mass density field and the impact of ionizing background intensity fluctuations

Satya Gontcho A Gontcho

UNIVERSITAT DE BARCELONA

Department of Quantum Physics and Astrophysics
Institute of Cosmos Sciences

Doctoral Thesis
Doctoral Program in Physics

Exploring the Universe with Quasar Absorption Spectra: correlations among tracers of the mass density field and the impact of ionizing background intensity fluctuations.

---

by

Satya Gontcho A Gontcho

Supervisor:	Jordi Miralda-Escudé	Institute of Cosmos Sciences
Tutor:	Alberto Manrique	Institute of Cosmos Sciences

Resum de la tesi

El treball que presentem en aquesta tesi versa sobre l'ús d'espectres de quàsars per a investigar l'Univers. Els sistemes d'absorció produïts per l'hidrogen intergalàctic en l'espectre electromagnètic de quàsars llunyans i brillants ens permeten explorar la distribució de gas en l'Univers. Atès que la llum dels quàsars es decala cap al roig a mesura que viatja a través de l'Univers, els fotons emesos amb una energia superior a la de la transició Lyα són absorbits (en realitat, rebotats per àtoms d'hidrogen) al llarg del seu viatge, just al punt on la seva longitud d'ona coincideix amb la línia de ressonància Lyα a 1216 Å. El resultat és el que denominem bosc Lyα , un camp d'absorció variable al llarg de l'espectre que reflecteix la densitat d'hidrogen neutre en funció de la posició al llarg de la línia de visual del quàsar. Estudis similars poden realitzar-se a la part de l'espectre cap al blau de la línia d'emissió del carboni triplement ionitzat (CIV), en què apareix absorció per part del CIV intergalàctic. La distribució d'aquest gas ionitzat a escales cosmològiques ens permet rastrejar el camp de densitat de matèria subjacent, i al mateix temps obtenir una visió de l'estat tèrmic del medi intergalàctic mitjançant l'estudi de les correlacions a petita escala de l'absorció Lyα .

La part I de la tesi, Introducció a l'Univers, ens introdueix les nocions físiques i observacionals necessàries per a la comprensió d'aquest treball doctoral. En el capítol 1, posem en context el camp de la cosmologia i les seves motivacions, i presentem el model estàndard que ha assolit un consens com *la millor descripció del nostre Univers* en l'actualitat. Seguidament, el capítol 2 presenta el formalisme i les nocions de cosmologia emprades en els següents capítols. A l'annex A hi ha aclariments addicionals pel lector interessat. A continuació, el capítol 3 presenta conceptes útils sobre l'ús dels espectres de quàsars per estudis cosmològics.

La part II comença amb el capítol 4, titolat **sobre l'efecte del fons ionitzant en la funció d'autocorrelació del bosc Lyα** . Aquest treball desenvolupa un marc analític per a comprendre els efectes d'una intensitat fluctuant del fons còsmic ionitzant sobre les correlacions de l'absorció en el bosc Lyα mesurades en espectres de quàsars. En absència d'aquestes fluctuacions d'intensitat, i en el límit d'escales grans en què el règim lineal és aplicable, l'espectre de potència del bosc Lyα ha de ser proporcional a l'espectre de potència de la massa en la teoria estàndard de matèria fosca freda esperada, amb les

conegudes distorsions de decalatge al vermell del règim lineal, i està totalment caracteritzat per un factor de biaix b_δ i un paràmetre de distorsió per decalatge β. Aquests dos paràmetres poden evolucionar amb el temps però són independents de l'escala. En el nostre treball trobem que les fluctuacions d'intensitat introdueixen una dependència d'escala tant en b_δ como en β, però mantenint el seu producte $b_\delta\beta$ fix. També mostrem que aquestes fluctuacions d'intensitat no esbiaixen de manera sistemàtica les mesures de l'escala d'oscilůlacions acústiques bariòniques (BAO) del bosc Lyα , la qual s'utilitza per indagar la presència d'energia fosca a l'Univers a les diverses èpoques en què podem mesurar aquesta escala. Només l'amplitud de l'autocorrelació Lyα es veu afectada.

El capítol 5 es titula **Creu-Correlació quàsars - bosc CIV**. De forma semblant a com el bosc Lyα s'utilitza per a sondar els núvols d'hidrogen neutre, hem utilitzat les característiques d'absorció del CIV per traçar estructures en l'interval de decalatge $1.4 < z < 4.2$, sondant el gas enriquit en metall i correlacionant-lo amb els quàsars. a. Gràcies a les dades del cartografiat complet de BOSS i al gran nombre de quàsars que inclou, hem pogut mesurar la creu-correlació de l'absorció de CIV amb quàsars amb precisió suficient per obtenir la primera mesura dels factors de biaix dels absorbidors de CIV. El resultat d'aquesta mesura pel factor de biaix de la fracció transmesa per CIV a un decalatge de $z = 2.3$ és: $(1 + \beta_{CIV})b_{CIV} = -0.024 \pm 0.003$, amb un error més gran per mesurar el factor de distorsió β_{CIV} i b_{CIV} separadament.

Resumen de la tesis

El trabajo que presentamos en este manuscrito gira en torno al uso de espectros de cuasar para investigar el Universo. Las características de absorción en el espectro electromagnético de los cuasares distantes brillantes por el hidrógeno ionizado nos dan acceso a la distribución de gas en el Universo. Debido a que la luz de cuásares distantes es redshifted a medida que viaja a través del Universo, los fotones emitidos con una energía por debajo de la transición Lyα serán absorbidos a lo largo de su viaje, en el punto donde su longitud de onda ha sido redshifted a la transición de longitud de onda de 1216 Å. Como resultado, un espectro observado y sus características, denominado Bosque Lyα , dependen de la densidad del hidrógeno neutro en función de la posición a lo largo de la línea de visión a partir del cuásar. Estudios similares pueden realizarse con fotones hacia el azul de la línea de emisión del carbono ionizado triple. El estudio de la distribución de este gas ionizado en las escalas cosmológicas nos permite rastrear el campo de densidad de materia subyacente, mientras que al mismo tiempo obtener una visión sobre el estado térmico del medio intergaláctico mediante el estudio de las correlaciones a pequeña escala de la absorción de Lyα .

La parte I de este manuscrito, **Introducción al Universo**, introduce todas las nociones físicas y observacionales necesarias para la comprensión de este trabajo doctoral. En el capítulo 1, ponemos en contexto el campo de la cosmología y sus motivaciones, así como nos acostumbramos a los modelos estándares que hicieron del consenso como *la mejor descripción de nuestro Universo* en este momento. El capítulo 2 presenta el formalismo y las nociones de cosmología utilizadas en los siguientes capítulos. En el apéndice A se encuentran aclaraciones adicionales para el lector interesado. Por último, el capítulo 3 presenta conceptos útiles para el uso de cuásares y sus espectros como observables para estudios cosmológicos.

La parte II comienza con el capítulo 4, **Sobre el efecto del fondo ionizante en la función de autocorrelación del bosque Lyα** . En este trabajo se presenta un marco analítico para comprender los efectos de una intensidad fluctuante del fondo ionizante cósmico sobre las correlaciones de la fracción de transmisión de Lyα bosque medido en espectros de cuasar. En ausencia de fluctuaciones de intensidad, y en el límite de grandes escalas en las que el régimen lineal es aplicable, el espectro de potencia Lyα debería tener el espectro de potencia de materia oscura fría esperada con distorsiones de

desplazamiento al rojo en el régimen lineal, con un factor de sesgo b_δ y un parámetro de distorsión de desplazamiento al rojo β que dependen del desplazamiento al rojo pero son independientes de la escala. Encontramos que las fluctuaciones de intensidad introducen una dependencia de escala tanto en b_δ como en β, pero manteniendo su producto $b_\delta\beta$ fijo. También mostraron que estas fluctuaciones no sesgo actual o futuras mediciones de la oscilación acústica barión (BAO) escala de Bosque Lyα . Sólo la amplitud de la autocorrelación Lyα se ve afectada, la posición del pico BAO no lo es.

El capítulo 5 se titula **Cuasar - CIV bosque correlación cruzada**. De manera similar, el bosque de Lyα se utiliza para probar las nubes de hidrógeno neutras, utilizamos las características de absorción del carbono ionizado triple (CIV) para (a) sondar el gas enriquecido en metal a cambio de rojo $1.4 < z < 4.2$, (b) $z < 2$ que no eran accesibles con el bosque Lyα . Gracias a los datos proporcionados por la encuesta completa de BOSS, existe un aumento suficiente en la densidad del número de cuásar, en comparación con los conjuntos de datos anteriores disponibles, para contrarrestar la menor sensibilidad del bosque CIV. Como resultado, hemos hecho la primera detección usando el método de transmisión continua de una señal de la correlación cruzada del bosque Cuasar-CIV. Esta detección permite medir el factor de sesgo de transmisión CIV al desplazamiento al rojo $z = 2.3$: $(1 + \beta_{CIV})b_{CIV} = -0.024 \pm 0.003$.

Abstract

The work we present in this manuscript revolves around the use of quasar spectra to probe the Universe. Absorption features in the electromagnetic spectrum of bright distant quasars by ionized hydrogen give us access to the distribution of gas in the Universe. Because the light from distant quasars is redshifted as it travels through the Universe, photons emitted with an energy below the Lyα transition will be absorbed along their journey, at the point where their wavelength has been redshifted to the transition wavelength of 1216 Å. As a result, an observed spectrum and its features, referred to as Lyα Forest, depend on the density of neutral hydrogen as a function of position along the line of sight from the quasar. Similar studies can be made with photons blueward of the emission line of the triply ionized carbon. Studying the distribution of this ionized gas on cosmological scales allows us to trace the underlying matter density field while at the same time gaining insight on the thermal state of the intergalactic medium by studying the small-scale correlations of the Lyα absorption.

Part I of this manuscript, **Introduction to the Universe** introduces all the physical and observational notions necessary for the understanding of this doctoral work. In chapter 1, we put in context the field of cosmology and its motivations as well as acquaint ourselves with the standard models that made consensus as *best describing our Universe* at this time. Chapter 2 presents the formalism and notions of cosmology used in the following chapters. Additional clarifications are available for the interested reader in appendix A. Chapter 3 introduces useful concepts for the use of quasars and their spectra as observables for cosmological surveys.

Part II starts with chapter 4, **On the effect of the ionizing background on the Lyα forest autocorrelation function**. In this work, we present an analytical framework to understand the effects of a fluctuating intensity of the cosmic ionizing background on the correlations of the Lyα Forest transmission fraction measured in quasar spectra. In the absence of intensity fluctuations, , and in the limit of large scales at which the linear regime is applicable, the Lyα power spectrum should have the expected cold dark matter power spectrum with redshift distortions in the linear regime, with a bias factor b_δ and a redshift distortion parameter β that depend on redshift but are independent of scale. We found that the intensity fluctuations introduce a scale dependence in both b_δ and β, but keeping their product $b_\delta\beta$ fixed. We also showed that these fluctuations do

not bias current or future measurements of the baryon acoustic oscillation (BAO) scale from Lyα Forest. Only the amplitude of the Lyα autocorrelation is affected, the position of the BAO peak is not.

Chapter 5 is titled **Quasar - CIV Forest cross-correlation**. In a similar fashion that the Lyα Forest is used to probe neutral hydrogen clouds, we use the absorption features of triply ionized carbon (CIV) to (a) probe metal enriched gas at redshift $1.4 < z < 4.2$, (b) trace structures at $z < 2$ that were not accessible with the Lyα Forest. Thanks to the data provided by the full BOSS survey, there is a sufficient increase in quasar number density, compared to previous data sets available, to offset the lower sensitivity of the CIV Forest. As a result, we have made the first detection using the continuum transmission approach of a signal from the Quasar - CIV forest cross-correlation. This detection allows to measure the transmission CIV bias factor at redshift $z = 2.3$: $(1 + \beta_{CIV})b_{CIV} = -0.024 \pm 0.003$.

Acknowledgements

Les mots me manquent pour exprimer l'étendue de la gratitude que j'éprouve à l'égard de ma famille. À mon père, Hubert, et ma mère, Catherine, merci de m'avoir fait don de l'excellente éducation que j'ai reçu depuis mon plus jeune âge. À mes grand-parents, Marie-Jeanne et Pierre, et aux matriarches de notre famille, Dame Jeanne et Dame Eugénie, merci de votre soutien tout au long de ces années.

To my PhD supervisor, Professor Jordi Miralda-Escudé, I would like to express my most sincere gratitude for his supervision and the great learning opportunities he has provided me with. Moltes gràcies ! Your dedication to your field is jaw-droppingly admirable.

I am extremely thankful to Andreu Font-Ribéra for his involvement these past couple of years. His input has been invaluable.

Un grand merci à Nicolas Busca pour s'être rendu disponible à plusieurs reprises et pour le soutien qu'il m'a apporté durant ma thèse. Chaque discussion a valu son pesant d'or.

I would like to acknowledge the wonderfully propitious environment of the "Lyα working group" of the BOSS/SDSS-III. Fruitful collaboration and discussions with Julian Bautista, Daniel Margala, David Kirkby, Stephen Bailey and Michael Blomqvist have, without a doubt, added to the quality of the work I produced. Also, thank you to David Schlegel and K.G. Lee for the kindness they have shown me on the few occasions our paths crossed.

My heartfelt gratitude goes to Isabelle Paris and Licia Verde for offering me their guidance and experience. I have learned a great deal from both of you.

During my time working at the University of Barcelona, my days were made brighter by a few people that I would like to recognize: Emilio Bellini, Lluis Mas-Ribas, Erika Antiche, Victor Moreno de la Cita, Fergus Simpson, Antonio Cuesta and Alvise Racanelli. Also, many thanks to JR Rodriguez, Eva Notario and Anna Bertolín for their help in navigating through the administrative mayhem. I would also like to give a special thank you to Olga Mena and Carlos Peña of the University of Valencia.

This doctoral work brings to an end 10^+ years of academical endeavors as a student. I would not be where I am today without Professor Emeritus Gérard Smadja. I had the good fortune of meeting him during my internship the summer between my first and second year at the University of Lyon when I was just seventeen. He has supervised me, provided me with great advice all through my academic career, and has helped me to

life changing opportunities. Gérard, votre rigueur, votre dévouement et votre attention aux détails a donné le ton pour la suite de mon parcours universitaire. Je vous suis extrêmement reconnaissante de la bienveillance dont vous avez fait preuve à mon égard.

Some of the fondest memories of my academical career, I have made while studying at the University of Lyon. Of course, I should start with the myriad hours spent at the IPNL with Yannick Copin, Emmanuel Gangler, the Nicolas (×2) and Patrick Nédélec – who gave me my first internship. A huge thank you to the SuperNovae group and the ALICE group. I must give an honorable mention to Mr Caldéro (all of my undergrad algebra classes as a math major), Mr Gence (all of my undergraduate classical mechanics classes but one) and Mr Chanfray (analytical mechanics). It was just an absolute delight to attend your classes, even the ones starting at 7:45 am sharp... Philippe Caldéro, merci de votre soutien et de m'avoir donner la possibilité de faire un TIPE. Votre naturel joyeux et bienveillant a toujours été grandement apprécié. Enfin, l'émulation produite par le groupe d'irréductibles de la licence de mathématiques est, jusqu'à ce jour, grandement appréciée. Alors Raph, Antoine, Yoann, Marie-Lianne, Oliv...merci!

From my time at the Orsay Magisterium, I am grateful to have met Renaud Parentani (mathematical physics, general relativity and cosmology) and Mathieu Langer (cosmology and "using order of magnitude tools to solve physical problems"). The amount of after class hours they offered me and a handful of other passionate students – every week – was simply out of this world. I believe this amount of dedication in and out of the classrooms is how you mold the future generations of scientists. Thank you to JB and Stahl for their undying eagerness to join me in questioning professors after class. I would like to give an honorable mention to Grégory Moreau for his class on classical electrodynamics...I was truly enthused by the course and the enthusiasm, dedication and care with which it was taught. Finally I am very grateful to Yann Mambrini. I rarely met someone with such an ability to explain flawlessly and with such clarity any concept or theory of physics. I have come to respect him immensely and I appreciate the continued mentoring since I have met him. Bryan Zaldivar-Montero, estoy muy agradecido. Me enseñaste enormemente en muy poco tiempo.

Dr Isha Savani, thank you for the moral support and the safe space you have provided me with ever since I met you, but especially during my PhD. The countless discussions we have had has informed the didactical approach I chose to take for Part I of my thesis manuscript.

Lluís, gràcies per ajudar-me amb espanyol i català. Güngur Arts family, thank you for making Barcelona home and grounding me during the past 4 years. Ahmad, thank you for continuing our Paris debating traditions and founding The Chameleon discussion salon with me. Alyshah, thank you for making your californian home mine

and chauffeuring me around. This undoubtedly facilitated my visits to Berkeley Lab – those visits have enormously contributed to the successful completion of this doctoral work. Remha, your friendship is a gem and our exchanges have always lifted me up. Enky, merci pour ton soutien au cours de ces dernières années.

Thank you to David Weinberg, Nicolas Busca and Nicholas Ross for making me the honor to be my jury.

Finally, to conclude these admittedly lengthy acknowledgments, I would like to state that my academic career has been a succession of benevolent encounters, for which I am extremely grateful. To all the professors, post-docs, grad-students and other students at my full time universities (Lyon, Paris XI, Paris VI and Barcelona), and temporary ones (CERN, Berkeley), thank you, my life is richer for having met you.

Contents

List of Figures

List of Tables

◇

Ce travail est dédié à Hubert, Catherine, Eugène, Totondo et Indou.
Vous avez ma gratitude la plus sincère pour me rappeler, jours après jours, la personne que j'aspire à être.

◇

Part I.

Introduction to the Universe

Chapter 1

Prelude

Within the remembrance of man, humanity has always struggled to understand the world around it and its place in it. As evidenced by our recovered knowledge from the Indus Valley Civilization, the Ancient Greeks or the Ancient Chinese amongst others, the concept of Universe has always been existing, as was the intent to make sense of it. Universe, from the latin *uni-* `"one"` + *-versus* `"turned"` → *universus* `"combined into one/whole"`, is a concept that encompasses all space and time, as well as its content (i.e. matter and energy). The effort to understand the Universe gave birth to one of the ever-fundamental scientific disciplines of contemporary times: physics. Derived from the ancient greek *φυσική* - *phusiké* - `"knowledge of nature"`, itself derived from *φύσις* – *phúsis* – `"nature"`, physics is the study of nature's most basic components and their interactions through space and time. The language developed to manipulate physical concepts are the mathematics, from the ancient greek *μάθημα* – *máthēma* – `"what one learns"`. As of now, our understanding of the Universe can be reduced to a theory of gravitation (General Relativity, GR), quantum mechanics, and a standard model of elementary particles (also referred to as the standard model of particle physics). By making the elementary particles interact with each other in a manner consistent with GR and the fundamental forces described by the standard model of particle physics, we are able to describe most of what we observe. In this chapter, we will expand on the standard models of particle physics and cosmology as it pertains to the doctoral work developed in this manuscript.

1.1 Standard Model of Particles Physics

The ***Standard Model of Particle Physics*** is the theory describing three of the four known fundamental forces – electromagnetic, weak, and strong, as well as classifying all known elementary particles. It has been verified experimentally with great accuracy. The latest of such experimental verifications occurred with the detection of the Higgs boson at CERN in 2012.

1.1.1 Fundamental forces

Electroweak interaction Electromagnetism and weak interaction, though they appear to be different at nowadays low energies and are modeled by two distinct theories, can be merged into a single electroweak force for energy above 100 GeV. Electroweak theory is important for modern cosmology, since shortly after the Big Bang, the temperature was above $\sim 10^{15}$ Kelvin. ***Electromagnetism*** is the force that acts between electrically charged particles. This phenomenon includes the electrostatic force acting between charged particles at rest, and the combined effect of electric and magnetic forces acting between charged particles moving relative to each other. The ***weak interaction*** or ***weak nuclear force*** concerns radioactive decays, which play an essential role in nuclear fission. See table 1.1 to compare properties of fundamental interactions.

Strong interaction or ***strong nuclear force***, is interesting in the way that it varies with distance. Indeed, at distances greater than 10^{-15} meters, the strong force is practically unobservable. It holds only inside the atomic nucleus.

Gravity is best described by the general theory of relativity, proposed by Albert Einstein in 1915. This theory describes gravity not as a force, but as a consequence of the curvature of space-time caused by the uneven distribution of mass-energy. The most extreme example of the curvature of space-time is a black hole. Nothing can escape out of it once its event horizon is crossed, not even light.

Interaction	Theory	Mediator	Relative Strength	Behaves as	Range (m)
Weak	EWT	W, Z	10^{25}	$\frac{1}{r}e^{-m_{\mathrm{W,Z}}r}$	10^{-18}
Strong	QCD	g	10^{38}	1	10^{-15}
Electromagnetic	QED	γ	10^{36}	$\frac{1}{r^2}$	∞
Gravitation	GR	–	1	$\frac{1}{r^2}$	∞

TABLE 1.1: Inventory of the four fundamental interactions

1.1.2 Particles

The *spin* of a particle is an intrinsic form of angular momentum. The first distinction between elementary particles comes from their spin: **fermions** have a spin 1/2, while **bosons** have a spin 1.

Fermions The standard model includes 12 fermions, and their 12 antiparticles. A particle and its antiparticle are oppositely *charged*. Fermions respect the Pauli exclusion principle, i.e. no two fermions can occupy the same quantum state within the same quantum system at the same time. Fermions are classified according to how they interact (i.e., by what type of *charge* they carry). There are six **quarks** (up, down, charm, strange, top, bottom), and six **leptons** (electron, electron neutrino, muon, muon neutrino, tau, tau neutrino). Pairs from each classification are grouped together to form a generation, see figure 1.1. Quarks are defined by the fact that they carry a *color charge*, in other words, they interact via strong interaction. A phenomenon called color confinement results in quarks being very strongly bound to one another, forming color-neutral composite particles (*hadrons*) containing either a quark and an antiquark (*mesons*) or three quarks (*baryons*). The familiar proton and neutron are the two baryons having the smallest mass. Quarks also carry *electric charge* and *weak isospin*. Hence, they interact with other fermions both electromagnetically and via the weak interaction. The remaining six fermions do not carry color charge and are called leptons. The three neutrinos do not carry electric charge either, so their motion is directly influenced only by the weak nuclear force, which makes them notoriously difficult to detect. However, because they carry an electric charge, the electron, muon, and tau all interact electromagnetically. Each member of a generation has greater mass than the corresponding particles of lower generations. The first generation charged particles do not decay; hence all ordinary (in other words, ***baryonic***) matter is made of such particles. Specifically, all atoms consist of electrons orbiting around an atomic nuclei, ultimately constituted of up and down quarks. Second and third generation charged particles, on the other hand, decay with very short half lives, and are observed only in very high-energy environments (early Universe, particle accelerators,...). Neutrinos of all generations also do not decay, and spread through the Universe, but rarely interact with baryonic matter.

Bosons also referred to as ***gauge bosons*** are defined as *force carriers* that mediate the strong, weak, and electromagnetic fundamental interactions. Since their spin is an integer, they do not follow the Pauli exclusion principle that constrains fermions. As a consequence, bosons do not have a theoretical limit on their spatial density. ***Photons*** mediate the electromagnetic force between electrically charged particles. The photon is massless and is well-described by the theory of quantum electrodynamics (QED). The

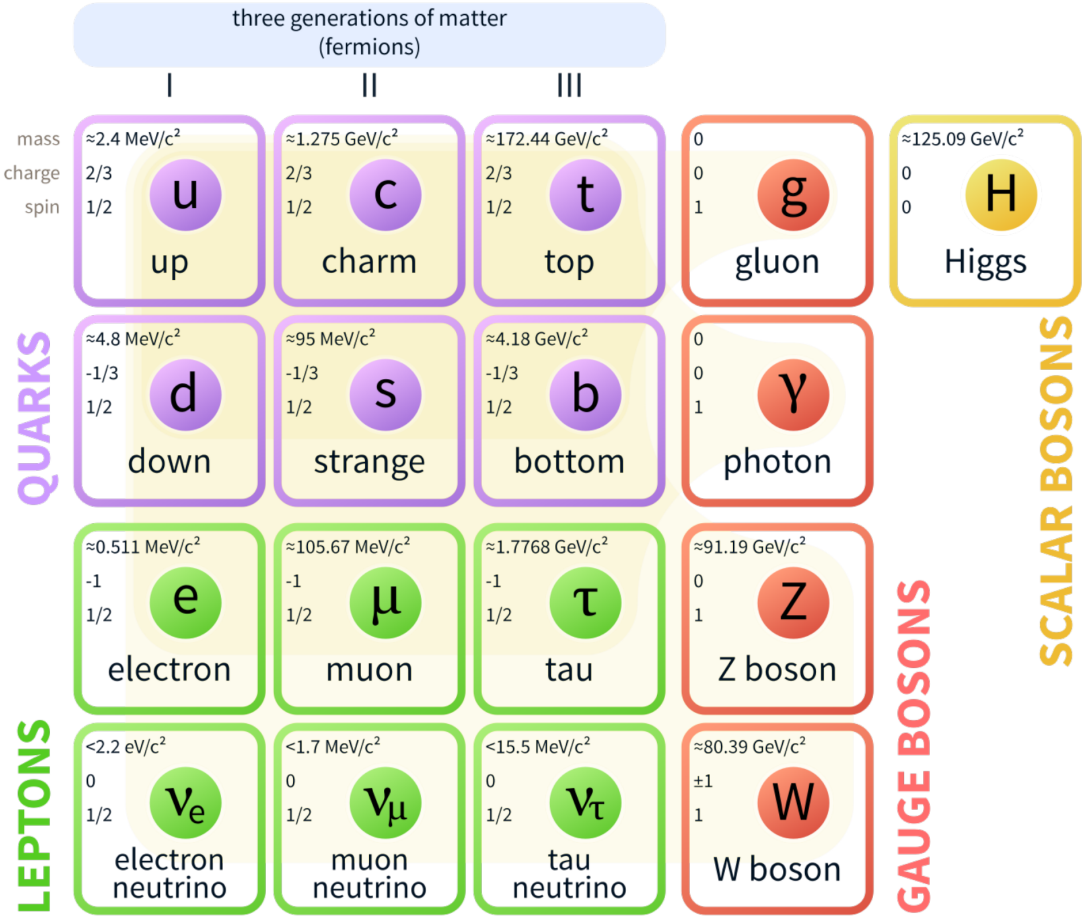

Source: *Fermilab, Office of Science, United States Department of Energy, Particle Data Group*

FIGURE 1.1: Standard model of elementary particles: the 12 fundamental fermions and 4 fundamental bosons.

W+, ***W-***, and ***Z*** gauge bosons mediate the weak interactions between particles (quark, leptons) of different *flavors*. They are massive, with the Z being more massive than the $W_{\pm}$. The $W_{\pm}$ carries an electric charge of ± 1 and couples to the electromagnetic interaction described by the electroweak theory (EWT). These three gauge bosons along with the photons are grouped together, as collectively mediating the electroweak interaction. The eight gluons mediate the strong interactions between color charged particles (the quarks). Gluons are massless. Because the gluons have an effective color charge, they can also interact among themselves. The gluons and their interactions are described by the theory of quantum chromodynamics (QCD). Finally, the ***Higgs particle*** is a massive scalar elementary particle theorized by Peter Higgs in 1964. It has no intrinsic spin, and for that reason is classified as a boson. The Higgs boson plays a unique role in the standard model, by explaining why the other elementary particles do, or do not, have a mass.

1.2 Standard Model of Cosmology

Let us first establish the definitions of the disciplines that provide the framework of this thesis: *astronomy*, *astrophysics* and *cosmology*. **Astronomy**, from the ancient greek *άστρον* – *ástron* – `"star"` + *νόμος* – *nómos* – `"arranging"`, is the study of celestial objects and phenomena. It deals with mathematics, physics, and chemistry, in an effort to explain the origin of celestial objects and phenomena, as well as to explain their evolution. **Astrophysics** is the branch of astronomy that employs the principles of physics and chemistry to ascertain the nature of celestial bodies, rather than their positions or motions in space. Finally, **cosmology**, from the ancient greek *κόσμος* – *kosmos* – `"world"` + *λογία* – *logia* – `"the study of"`, is the study of the origin, evolution, and eventual fate of the Universe.

The standard model of cosmology, also referred to as ΛCDM model, is the simplest model that provides a good account for our observations of the Universe.

The pillars of the so called ΛCDM model

Hypothesis 1:

Gravitation is described by Einstein's theory of General Relativity.

Hypothesis 2:

The Universe is filled with radiation, matter (baryonic + dark) and dark energy.

Hypothesis 3:

The topology of our Universe is trivial.

Hypothesis 3 means that we make the choice to work in a simply connected 4D space. In other words, if 2 events take place at the same moment in time and space, they are the same event.

Cosmological principle:

The Universe is homogeneous and isotropic on large scales ($\mathcal{O}(100)$ Mpc).

Copernican principle:

There is no privileged point in space in the Universe.

At last, we can simply say that the ***Standard Model of Cosmology*** = (Hypothesis 1 + Hypothesis 2 + Hypothesis 3 + Cosmological principle + Copernican principle) with knowledge of the intrinsic properties of the fundamental particles from the *standard model of particle physics*.

A word on *dark energy*

The cosmological constant Λ was introduced by Albert Einstein as an addition to his theory of General Relativity to satisfy his view that the Universe should be static. When Edwin Hubble observed in 1929 that all galaxies outside of the Local Group – our neighborhood of the Universe – are moving away from each other, the concept was temporarily put aside. It was reintroduced in the 1990s, following the realization that the expansion of the Universe is accelerating and that about 70% of the content of the Universe can only be described by its 3 main characteristics: (1) it functions as anti-gravity, in other words, its pressure is negative (2) if it clusters, it does so at a rate much weaker than that of matter and finally (3) it dilutes extremely slowly in the expanding Universe. Because of its mysterious nature, it was christened *dark energy*, also referred to as *vacuum energy*. General Relativity predicts that Λ has a density that decreases very slowly or stays constant and exerces a pressure $P < -\frac{1}{3}\rho$. The former prediction explains why its term has become prevalent only in the late times of the expansion of the Universe.

A word on *dark matter*

Studies of the XXth century have demonstrated the existence of a form of matter that is responsible for most of the matter budget in the Universe and does not emit luminous radiation. Because of this latter characteristic, it was christened *dark matter*. The first pointer as to the existence of dark matter came with the study presented by Zwicky in 1933 who analyzed the motion of the galaxies in the cluster Coma. Subsequently, other independent observations have indicated the presence of dark matter from the kinematics of virally systems and rotating spiral galaxies. See the work of Vera Rubin and Kent Ford in 1970 for example [1], as well as from the effects of gravitational lensing of background objects (see the 2004 observation of the Bullet Cluster by Chandra Xray observatory). Dark matter appears to have an important role in the formation of the structures and in the evolution of galaxies.

A brief thermal history

Table 1.2, figure 1.2 and the following description of the different epochs of the Universe's history will give the reader a useful overview of the chronology of events as well as the *energies*, *temparatures*, *times* and *redshifts* at play.

-Epoch-/Event	Time	Temp. (K)	Energy (eV)	Redshift
Hot Big Bang	-	-	-	-
Inflation	-	-	-	-
Reheating	-	0	-	$\sim 10^{28}$
-Radiation domination era-	**-**	**-**	**-**	**-**
Baryongenesis-Leptogenesis	10^{-4} s	$2 \cdot 10^{12}$	$2 \cdot 10^{8}$	10^{11}
Primordial Nucleosynthesis	100 s	10^{9}	10^{5}	10^{9}
-Matter domination era-	**100 kyrs**	**9000**	**0.81**	**3400**
Recombination	380 kyrs	3000	0.3	1100
Reionisation	320 Myrs	120	0.01	20
First galaxies formation	1.3 Gyrs	60	$5 \cdot 10^{-3}$	10
-Dark Energy domination era-	**9.4 Gyrs**	**4.8**	$\mathbf{4{\cdot}10^{-4}}$	**0.75**
Today	15 Gyrs	2.7	$2.35 \cdot 10^{-4}$	0

TABLE 1.2: Brief thermal history of the universe

Big Bang Point in history where the Universe can be verified to have entered a regime where the laws of physics as we understand them work.

Inflation Phase of the Universe's history consisting of an exponential expansion of space right after the Big Bang singularity. It is expected to have lasted about 10^{-32} seconds. This is where the primordial fluctuations in the metric responsible for the formation of structures (halos, galaxies, stars, etc.) originates.

Reheating Period during which all the fundamental particles known to the Standard Model described in section 1.1 are generated. It is assumed that inflation has left our Universe is hot dense state – a primordial soup of fundamental particles – where it could expand and cool down as a result of the expansion. From this point on, particles take turn *decoupling* from the Hubble flow (see section 2.1.2 – next chapter). In plain English: one after the other, particles stop following the expansion of the Universe and follow an evolution of their own. Figure 1.2 presents a timeline of the decouplings of the elementary particles.

Baryongenesis - Leptogenesis Creation of leptons, then baryons. The conditions for dark matter to be thermally produced are in place and it is the period at which weakly

interacting massive particles (WIMPS) – the most popular dark matter candidates – decouple from the plasma. Dark matter then start to collapse into halos.

Primordial Nucleosynthesis Neutrinos decouple from the primordial plasma, the nuclear fusion processes dominate and light nuclei (H, D, He, Li and Be) are formed. The relative abundances of these light elements is predictable and these predictions are compared to observations, see figure 1.3 for a simplified inventory.

Recombination Light nuclei and electrons form neutral atoms[1]. Though very rapid, the process is not instantaneous. The Universe becomes transparent to photons, *i.e.* photons can travel long distances without encountering an ionized structure that would absorb them. Photons decouple from the primordial plasma and are today known as the ***cosmic microwave background*** (CMB). This relic electromagnetic radiation is observed at present day to be $T = 2.725\,K$ or 0.235 meV.

Reionization It starts with the *dark ages*, a period where the Universe was transparent, totally neutral and where no large scale structures had formed yet. Then, baryonic matter collapses in dark matter halos, creating the first stars and the first galaxies, as well as enabling processes that result in the ionization of their environment. Eventually, the whole Universe is reionized. This is also at that point that the rest of elements of the Mendeleev table are formed by fusion processes in stars and supernovae explosions. This epoch is explained in more details in chapter 3, section 3.4.

Now We have recently (in terms of the lifetime of our Universe) entered an epoch where the expansion is dominated by the cosmological constant...

[1] *The Saha equation* describes this process if we consider Hydrogen alone

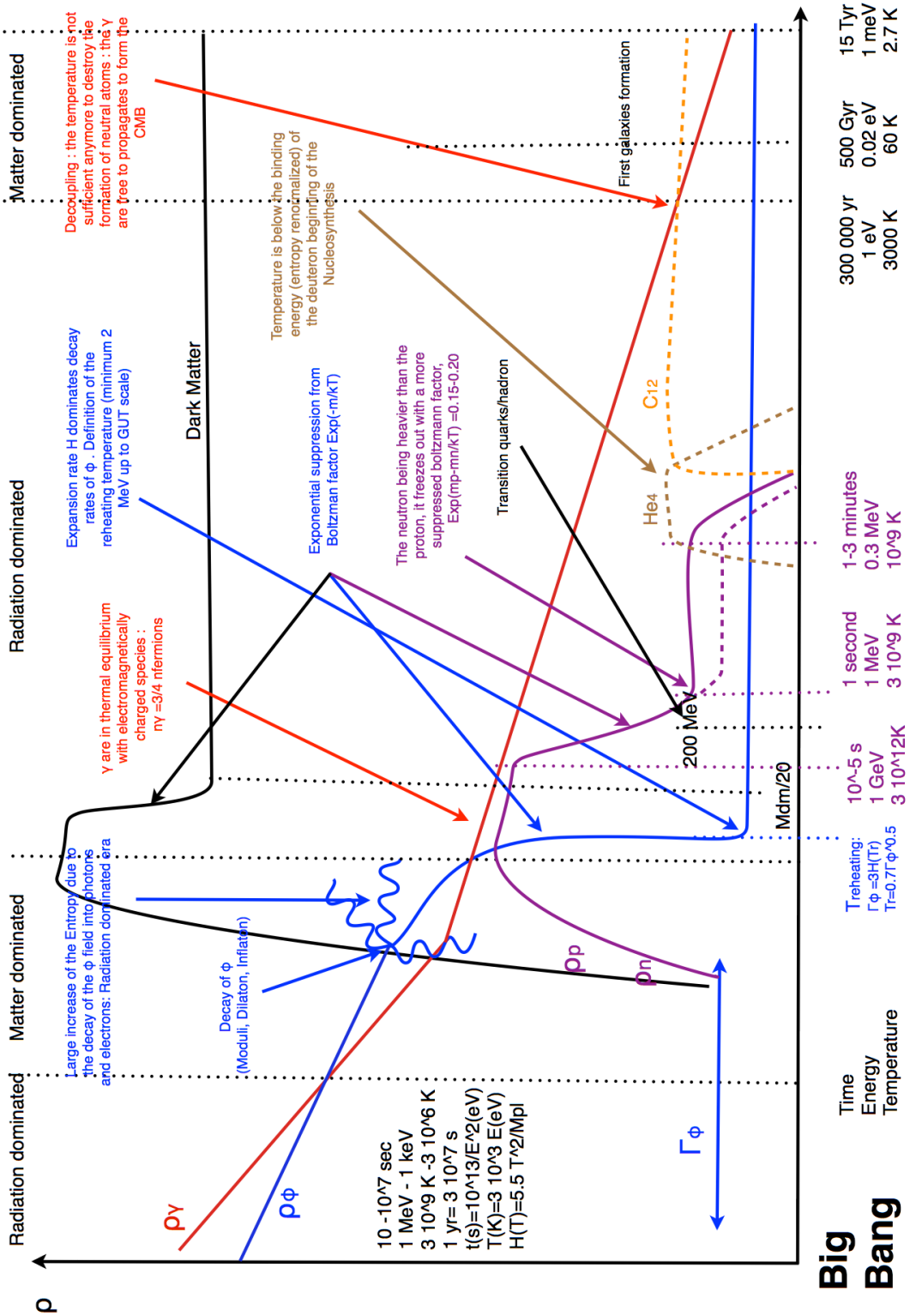

Source: *Dr. Yann Mambrini (LPT Orsay),* "Dark Matter and Physics Beyond Standard Model"

FIGURE 1.2: Timeline of the decouplings of fundamental particles from the primordial plasma.

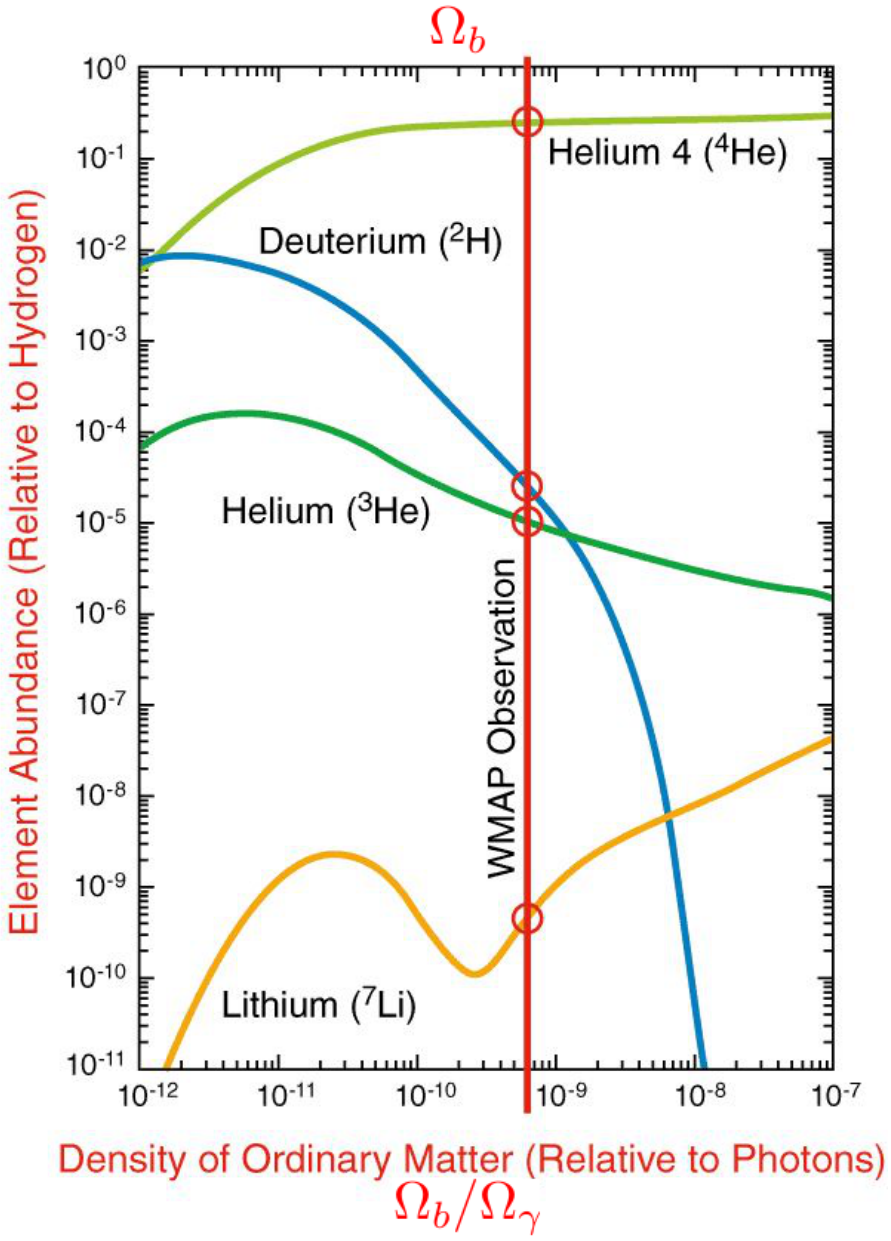

Source: *NASA/WMAP Science Team.* Steigman, Encyclopedia of Astronomy and Astrophysics.

FIGURE 1.3: Light elements abundances (relative to hydrogen) as a function of the baryon density. The WMAP satellite measured the baryon density indicated with the vertical red line [2], therefore giving a measure of the different abundances – highlighted by the red circles.

Chapter 2

Introduction to Cosmology

2.1 Construction of a general metric of the Universe

The ***cosmological principle*** is the fundamental hypothesis on which the construction of a general space-time metric of the Universe is based:

The Universe is homogeneous and isotropic on large scales ($\mathcal{O}(100)$ Mpc).

We start by building a 3D spatial metric plunged in a 4D space. Using cartesian coordinates (x, y, z, ω) to describe an event, but replacing (x, y, z) by spherical polar coordinates (ϱ, θ, ϕ), we have the infinite space interval dl

$$dl^2 = d\varrho^2 + \varrho^2 d\Omega^2 + d\omega^2, \tag{2.1}$$

where $d\Omega^2 = d\theta^2 + \sin^2(\theta) d\phi^2$. For a positive curvature one can also write

$$x^2 + y^2 + z^2 + \omega^2 = \varrho^2 + \omega^2 = R^2 \tag{2.2}$$

where R is the curvature radius, independent of the position (x, y, z) by the hypothesis of ***homogeneity***. Therefore, $\varrho d\varrho + \omega d\omega = 0$. It follows that

$$d\omega^2 = \frac{\varrho^2}{\omega^2} d\varrho^2 = \frac{\varrho^2}{R^2 - \varrho^2} d\varrho^2 \quad \Longrightarrow \quad dl^2 = d\varrho^2 + \frac{\varrho^2 d\varrho^2}{R^2 - \varrho^2} + \varrho^2 d\Omega^2 \tag{2.3}$$

This is a homogeneous, isotropic 3D space of positive curvature $1/R^2$. Setting $\varrho = Rr$, we get

$$dl^2 = R^2 \left(\frac{dr^2}{1 - r^2} + r^2 d\Omega^2 \right). \tag{2.4}$$

Negative and zero curvature are also possible. For the negative case, the radius condition should be written

$$dl^2 = d\varrho^2 + \varrho^2 d\Omega^2 - d\omega^2 \quad \text{and} \quad \varrho^2 - \omega^2 = -R^2 \tag{2.5}$$

This is the equivalent of the hyperboloid surfaces in 2D. It follows that

$$dl^2 = R^2 \left(\frac{dr^2}{1 + r^2} + r^2 d\Omega^2 \right). \tag{2.6}$$

We can combine all the possible curvature with the generic expression

$$dl^2 = R^2 \left(\frac{dr^2}{1 - \kappa r^2} + r^2 d\Omega^2 \right) \tag{2.7}$$

with $\kappa = +1$ for a positive curvature */closed Universe*, $\kappa = 0$ for no curvature */flat Universe*[1] and $\kappa = -1$ for a negative curvature / *open Universe*. In general, we must allow for R to be an arbitrary function of time $R(t)$ – not space since that would go against the ***homogeneity*** condition. The *space-time* interval between two events,

$$\boxed{ds^2 = c^2 dt^2 - R^2(t) \left(\frac{dr^2}{1 - \kappa r^2} + r^2 d\theta^2 + r^2 \sin^2(\theta) d\phi^2 \right)} \tag{FLRW}$$

is a *relativistic invariant* whose value does not depend upon the inertial frame of reference in which it is evaluated[2]. It is also known as the ***Friedmann-Lemaître-Robertson-Walker (FLRW) metric***. It was first derived by Alexander Friedmann in 1922, then independently again by Georges Lemaître in 1927, and finally more generally by Howard Robertson and Arthur Walker in 1935. It applies to any metric theory of gravity, not just general relativity. A useful alternative form of the FLRW metric is

$$ds^2 = c^2 dt^2 - R^2(t) \left(d\chi^2 + S_k^2(\chi) d\Omega^2 \right) \tag{2.8}$$

where

[1] It is important to note that "flat Universe" means flat in space, not flat in space-time.

[2] The notation ω was introduced to maintain an homogeneity of dimensions between coordinates of space and time : $d\omega^2 = c^2 dt^2$.

$$S_1(\chi) = \sin(\chi),\ S_0(\chi) = \chi,\ S_{-1}(\chi) = \sinh(\chi). \tag{2.9}$$

2.1.1 Redshift

Let us change our convention of variables to (t, χ, Ω). It is less obvious to understand the physics lying beyond the equation, but more practical to deal with formal calculations. This becomes clear when one needs to compute processes like the *redshift*. Indeed, as one of the most easily measured observable, the wavelength of light from astronomical sources is crucial to determine distances in the Universe. Let us consider two pulses of light emitted at times $t = t_e$ and $t = t_e + \delta t_e$ by an object at χ towards an observer at the origin who picks them up at $t = t_0$ and $t = t_0 + \delta t_0$. The light is emitted in a solid angle $d\Omega = 0$ and follows a geodesic[3]. Therefore, for photons traveling towards the origin $cdt = -R(t)d\chi$. Because χ represent a ***comoving coordinate*** (coordinate fixed and independent of time, see appendix A.1):

$$\chi = \int_{t_e}^{t_0} \frac{cdt}{R(t)} = \int_{t_e+\delta t_e}^{t_0+\delta t_0} \frac{cdt}{R(t)} \tag{2.10}$$

Subtracting the first integral from the second:

$$\int_{t_0}^{t_0+\delta t_0} \frac{cdt}{R(t)} - \int_{t_e}^{t_e+\delta t_e} \frac{cdt}{R(t)} = 0. \tag{2.11}$$

For small intervals $R(t)$ is almost constant, whereas t_e and t_0 are usually very spaced $(R(t_e) \neq R(t_0))$, so

$$\frac{\delta t_0}{R(t_0)} = \frac{\delta t_e}{R(t_e)}. \tag{2.12}$$

The ***redshift*** is defined as

$$\boxed{1 + z = \frac{\lambda_0}{\lambda_e} = \frac{\nu_e}{\nu_0} = \frac{\delta t_0}{\delta t_e} = \frac{R(t_0)}{R(t_e)}.} \tag{Redshift}$$

[3] A geodesic is the a generalization of the notion of a *straight line* to curved spaces. A particle whose trajectory respects $ds = 0$ follows a geodesic.

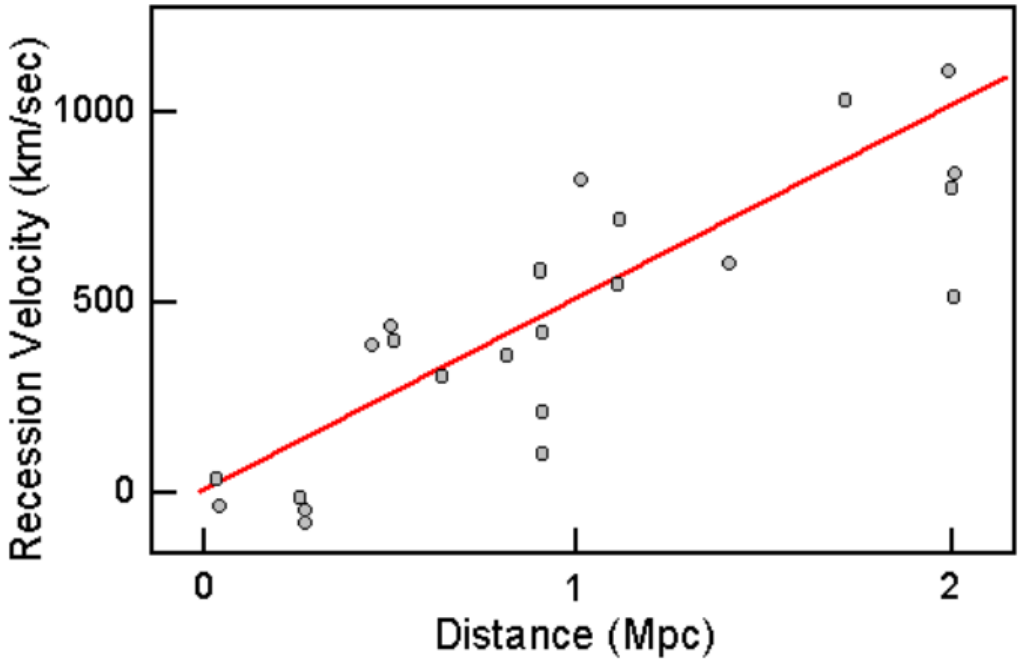

Source: *Prof. Richard Pogge (OSU),* Astronomy 162

FIGURE 2.1: Edwin Hubble's 1929 expansion data, see [3]. Let us acknowledge the fact that Hubble correctly intuited a linear law between the distance and the velocity of observed galaxies, and this, on a scale from 0 to 2 Mpc. Nowadays, this law has been verified up to distances of order of several Gpc.

2.1.2 Hubble Law

The set of galaxies in the Universe is at rest in ***comoving coordinates*** r or χ, θ, and ϕ. The expansion of the Universe is contained in the size factor $R(t)$. We refer the reader to section A.1 of appendix A for more details on the different notions of distances in the Universe. Let us consider the ***proper distance*** to a galaxy at radius χ

$$d_P = \int_0^\chi R(t) d\chi = R(t)\chi. \tag{2.13}$$

Since χ is fixed, the rate of recession of the galaxy is

$$v = \frac{d}{dt}(d_P) = \dot{R}_\chi = \frac{\dot{R}}{R} d_P. \tag{2.14}$$

where the *dot* notation indicates a time derivative.

From there we simultaneously define the ***expansion rate*** $H(t)$ and introduce the ***scale factor*** $a(t)$, as it is often referred to in the literature,

$$H(t) = \frac{\dot{R}}{R} = \frac{\dot{a}}{a}. \tag{2.15}$$

The ***Hubble's constant*** at current time t_0, i.e. today:

$$\boxed{H(t_0) = H_0.} \qquad \text{(Hubble's constant)}$$

We introduce that $H_0 = 100{\cdot}h$ km/s/Mpc $\equiv 2.13{\cdot}10^{-42}h$ GeV (see A.4 for the equivalence in matter dominated era). This corresponds to the recession speed of a galaxy at a distance of 1 Mpc, where h is a quantity that has been measured by different cosmological surveys. The latest measurement at this date comes from the PLANCK experiment (see [4], results of 2015), and is $h = 67.8 \pm 0.9$ km/s/Mpc.

Comes ***Hubble's law***, also illustrated on figure 2.1,

$$\boxed{v = H(t)d_p} \qquad \text{(Hubble's law)}$$

that can be interpreted as such: *for an observer on Earth, at any given point in time t, an astronomical object at rest is receding at speed $v(t)$*. Incidentally, the motion of astronomical objects due exclusively to this expansion is known as the ***Hubble flow***. It should be noted that Hubble's law is a direct consequence of the cosmological principle.

We also define the ***Hubble time***, $t_H = 1/H_0$, that is the inverse of the Hubble constant.

$$t_H \;=\; 4.55 \cdot 10^{17} \text{ s} \;=\; 14.4 \cdot 10^9 \text{ years}. \tag{2.16}$$

The Hubble time is the age that the Universe would be if its expansion was linear. We have seen in section 1.2 that the expansion of the Universe is not linear and that is why the measured value for the age of the Universe is

$$t_{BB} = 13.799 \pm 0.021 \text{ Gyr (current value from [4])}. \tag{2.17}$$

These two times are related by a dimensionless factor, called the ***scalar spectral index*** n_s, that depends on the mass-energy content of the Universe. The current value of this index is $n_s = 0.968 \pm 0.006$ (from [4]) and the relation $t_H = n_s \cdot t_{BB}$ is satisfied.

Finally, we define ***the Hubble radius*** *-or-* ***the Hubble horizon***

$$\boxed{r_H = \frac{c}{H(t)}} \qquad \text{(Hubble radius)}$$

as a conceptual horizon defining the boundary between particles that are moving slower and faster than the speed of light relative to an observer at a given time. If two particles are separated by a distance greater than the Hubble radius, their relation is *acausal*. In plain english, they cannot talk to each other as they are now, but they might have been able to do so in the past. However, if they are outside of each other's particle horizon[4], they could have never communicated. Depending on the form of expansion of the universe, they may be able to exchange information in the future. This horizon is not so much a physical distance as it is a useful length scale. Indeed, most physical distances in cosmology can be written in terms of the factors used to express the Hubble radius. One can also define the ***comoving Hubble horizon*** by dividing the Hubble radius by the scale factor: r_H/a.

2.2 Must know of the Hubble expansion

The Friedmann equations govern the expansion of space, under the assumptions of the cosmological principle and that the Universe is filled with various *perfect fluids* that make up the totality of its content. The different fluids are assumed to be of the following types: matter, radiation, curvature and cosmological constant. The total *energy density* and *pressure* are respectively the sum of the contribution of each of the affore mentioned fluids:

$$\rho(t) = \sum_i \rho_i(t) \tag{2.18}$$

$$P(t) = \sum_i P_i(t) \tag{2.19}$$

For more details on how to derive the Friedmann equations from the Einstein equations of General Relativity, see section A.3 of appendix A. The *first Friedmann* equation is

$$\boxed{H^2 = \left(\frac{\dot{a}}{a}\right)^2 = \frac{8\pi G}{3}\rho + \frac{\Lambda c^2}{3} - \frac{\kappa c^2}{a^2}} \qquad \text{(Expansion)}$$

[4]The comoving horizon is the maximum distance possibly covered by particles in the time-span of the life of the universe.

where $G = 1/M_P$ is the gravitational coupling[5] and Λ is the cosmological constant. The Expansion equation can also easily be derived from Newton's second law (see section A.2 of appendix A). The *second Friedmann* equation, if not directly obtained from the Einstein equations, can be derived by adding the time derivative of the expansion rate (see equation 2.15) to the Expansion equation

$$\boxed{\dot{H} + H^2 = \frac{\ddot{a}}{a} = -\frac{4\pi G}{3}\left(\rho + \frac{3P}{c^2}\right) + \frac{\Lambda c^2}{3}} \qquad \text{(Acceleration)}$$

The energy density of the content of the Universe respects the *first law of thermodynamics* with conservation of entropy, that can be written as

$$\boxed{\dot{\rho} + 3H\left(\rho + \frac{P}{c^2}\right) = 0.} \qquad \text{(Continuity)}$$

The Continuity equation can also be obtained by taking the derivative of the Expansion equation and using the Acceleration equation.

Since the content of the Universe is assumed to be a series of perfect fluid, each of their pressure is related to their energy density by a barotropic index w, assumed constant by the standard model of cosmology

$$\boxed{w_i = \frac{P_i}{\rho_i}.} \qquad \text{(Equation of state)}$$

where $w = 0$ for non-relativistic fluids and $w = 1/3$ for relativistic fluids.

The generalization of the Continuity equation is

$$\sum_i \left[\dot{\rho}_i + 3H\left(1 + \frac{w_i}{c^2}\right)\rho_i\right] = 0 \qquad (2.20)$$

The Expansion, the Acceleration, the Continuity equations and the Equation of state give a system of equations that allows to solve $a(t)$, $\rho(t)$ and $P(t)$.

By deriving the Expansion equation from Newton's second law, we become acquainted with a natural scale for matter density, called ***critical density***:

$$\rho_c = \frac{3H^2}{8\pi G} \qquad (2.21)$$

[5] M_P is the Planck mass $= 1.22 \cdot 10^{22}$ GeV.

that corresponds to the total energy density of the Universe expected at t, if the Universe is flat. In other words, if $\rho < \rho_c$ the expansion will never end (*loose system*), and if $\rho > \rho_c$ the expansion will eventually stop and the Universe will collapse onto itself (*bound system*). At present, the numerical value of the critical density is

$$\rho_c^0 = \frac{3H_0^2}{8\pi G} = 10^{-5} h^2 \text{GeV} \cdot \text{cm}^{-3} = 1.88\, h^2 \cdot 10^{-29}\, g\, \text{cm}^{-3} \tag{2.22}$$

We define the ***energy density fraction*** associated to each of the fluids making up the content of the Universe

$$\Omega_i = \frac{\rho_i}{\rho_c} \tag{2.23}$$

The Hubble expansion rate can be written as a function of these energy density fractions for today's values Ω_i^0

$$H(z) = H_0 \sqrt{\Omega_M^0 (1+z)^3 + \Omega_R^0 (1+z)^4 + \Omega_\kappa (1+z)^2 + \Omega_{DE}^0 f(z)} \tag{2.24}$$

where the current numerical values can be found in Table 2.1, the scale factor a has been replaced by its equivalent $a(t) = 1/(1+z)$ and $f(z)$ is a function that defines the evolution of the dark energy density. $f(z) = 1$ in the case of a cosmological constant.

It should be noted that all the results obtained in this section are valid regardless of the theory of gravity assumed, as long as it is a *metric* theory of gravity.

2.3 The content of our Universe

In Chapter 1, we have introduced all the fluids that make up the content of the Universe, as per Hypothesis 2. Here, we present additional information to help the reader understand the behavior of each fluid in the context of the Hubble expansion.

The behavior of the scale factor can be obtained by solving the Expansion equation for a single fluid. Similarly, for a single fluid, it is possible to solve the Continuity equation. Its solution is

$$\rho_i(t) = \rho_0 \left(\frac{a(t)}{a_0} \right)^{-3(1+w_i)} . \tag{2.25}$$

To the curvature term, we associate an energy density $\rho_\kappa(t) = \frac{-3\kappa}{8\pi G a^2(t)}$. Correspondingly, we associate $\rho_\Lambda = \frac{\Lambda}{8\pi G}$ with the dark energy – or cosmological constant – term.

Table 2.1 presents the evolution of the aforementioned quantities, as well as their current energy density fraction numerical values. These values can be used to integrate the Expansion equation and derive the age of the Universe.

Fluid	w_i	$\rho(a)$	$a(t)$	Ω_i	Numerical Value*
Baryonic Matter	0	$\propto a^{-3}$	$\propto t^{2/3}$	Ω_b	0.049 ± 0.005
Cold Dark Matter	0	$\propto a^{-3}$	$\propto t^{2/3}$	Ω_{CDM}	0.268 ± 0.013
Radiation	1/3	$\propto a^{-4}$	$\propto t^{1/2}$	Ω_R	$(9.16 \pm 0.24) \times 10^{-5}$
Curvature	-1/3	$\propto a^{-2}$	$\propto t$	Ω_κ	$-0.005^{+0.016}_{-0.017}$
Cosmological Constant	-1	$\propto a^0$	$\propto t^{exp(Ht)}$	Ω_{DE}	0.683 ± 0.013

TABLE 2.1: Useful values and notations associated with the behavior of the different cosmological fluids. The numerical values of the density fractions come from [4] and are the *today** values. Radiation = photons + neutrinos.

2.4 Structure formation

It is the accepted view at this time that the seeds for cosmological structures – namely energy density fluctuations – result from Gaussian quantum fluctuations of a single field ϕ that underwent an accelerated expansion during the inflation phase. Indeed at the beginning of inflation, quantum fluctuations are generated on sub-Hubble scales. Then, they are stretched out of the Hubble radius by an exponential expansion driven by a nearly flat potential (referred to as *slow-roll potential* in the literature). At the begining of the *reheating* period, the quantum fluctuations now found themselves to be classical (*macroscopic*), and to have been stretched out to a-causal distances. This results in the variances of the Fourier modes of energy density fluctuations being almost scale-invariant. From this point on, the energy density fluctuations progressively re-renter the Hubble radius in the subsequent non-accelerating evolution of the Universe and undergo gravitational collapse to form the large scale structures observed at this day.

In the following sub-sections, we will introduce two statistical descriptors of these fluctuations (also referred to as *perturbations*) that are the object of measurements from cosmological surveys: the power spectrum and the correlation function. *By comparing these measurements to predictions from existing cosmological models, one can constrain cosmological parameters.*

2.4.1 Primordial power spectrum

This is the only time in this chapter where we will "drop introduce" an equation / notion without a walk-through of the calculations and the mathematical framework used to obtain it. I refer a reader interested in the details to the lecture given by Hiranya Peiris at University College London "Cosmology Part II: The Perturbed Universe"[6], page 14 of her notes. An other interesting piece of literature on the topic are the TASI lectures on inflation by William Kinney [5].

We are interested in the *scalar* perturbations to the metric that couple to the energy density of matter and radiation. As is, they are ultimately responsible for most of the homogeneities and anisotropies in the Universe.

We introduce the notions of *dimensional* ***power spectrum*** $\mathcal{P}(k)$ and *dimensionless, scale-invariant* ***power spectrum*** Δ^2 as the variance per logarithmic interval of Fourier mode. Well after *recombination*, they relate to the contrast density of matter or radiation fluids, $\delta_\rho(x) = (\rho(x) - \rho_0)/\rho_0$, by

$$(\delta_\rho)^2 = \int \Delta^2 d\ln k = \int \frac{k^3 \mathcal{P}(k)}{2\pi^2} d\ln k \tag{2.26}$$

An other way to introduce it is to consider $d^3\mathscr{P}$, the power inside a Fourier space volume d^3k of the mass density fluctuations

$$d^3\mathscr{P} = \frac{d^3k}{(2\pi)^3}\mathcal{P}(k) \tag{2.27}$$

and integrate it over the solid angle

$$d\mathscr{P} = \frac{k^2 dk}{2\pi^2}\mathcal{P}(k) = \frac{k^3\mathcal{P}(k)}{2\pi^2} d\ln k \tag{2.28}$$

As previously mentioned, we assume a *slow-roll* inflation and it follows quasi-scale invariant curvature perturbations. We re-introduce the ***scalar spectral index*** n_s as a way to quantify small departure from scale-invariance

$$n_s - 1 \equiv \frac{d\ln(\mathcal{P}(k))}{d\ln k} \qquad \mathcal{P}(k) \propto k^{n_s - 1}. \tag{2.29}$$

It is to be noted that a scale invariant power spectrum (in the sense of constant amplitude) has $n_s = 1$ and current measurement indicate $n_s = 0.968 \pm 0.006$.

[6] http://zuserver2.star.ucl.ac.uk/ hiranya/PHASM336

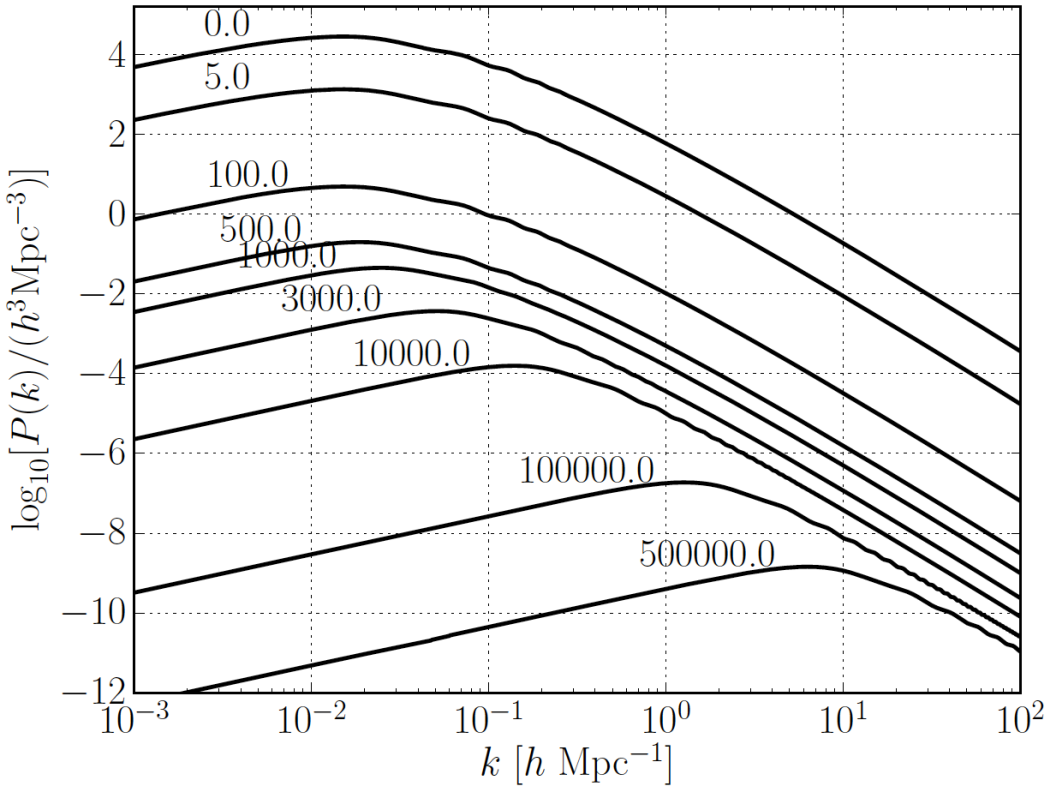

Source: *Dr. Julián Bautista (U of Utah)*

FIGURE 2.2: Evolution of the matter power spectrum $\mathcal{P}(k)$ from $z = 500000$ (lower line) to $z = 0$ (upper line). During the matter dominated era and the dark energy dominated era, Gravity makes matter density perturbations of all scales grow with time. However during the radiation dominated era, the rate of growth for matter density perturbations is null because the effects of thermal pressure counteract those of Gravity. Modes outside the Hubble horizon are not in causal contact and therefore are not submitted to gravitational collapse. As a result they keep growing until they re-enter the horizon, and it causes the break we observe in the power spectrum slope. This peak moves toward smaller k, i.e. larger scales, as the horizon keeps growing. As matter starts to dominate at $z \lesssim 2000$, perturbations inside and outside the horizon grow at same rate and the break in the power spectrum no longer shifts to small k.

On large scales, linear perturbation theory predicts that $\mathcal{P}$ grows as k and that these modes conserve their Gaussianity until later times. At $k \sim 0.01$ Mpc^{-1} for $z \lesssim 2000$ – and higher k values for higher redshifts – the power spectrum turns over. This scale correspond to the transition between radiation dominated era and matter dominated era. Beyond the peak, the power falls as $k^{-3} \ln^2 (k/k_{eq})$ where k_{eq} is the wavenumber of a mode that enters the Hubble horizon at the radiation-matter transition. This behavior is illustrated in figure 2.2. Linear perturbation theory stops describing properly the behavior of fluctuations at scales inferior to 10 Mpc (at $z \equiv 0$).

In terms of observations, the power spectrum corresponds to the probability to have matter periodically distributed with a wavenumber $k = 1/\lambda$.

2.4.2 Correlation function

One way to define the two–point correlation function $\xi(r)$ is to introduce it as the inverse Fourier transform of the power spectrum

$$\xi(r) = \frac{1}{(2\pi)^3} \int \mathcal{P} e^{-i\vec{k}\cdot\vec{r}} d^3k \tag{2.30}$$

A more physical way to introduce the concept is to use the distribution of galaxies as an illustration. The two–points correlation function of galaxies is the simplest description of the galaxies distribution at large scale. It quantifies the excess of probability to find a *galaxy 2* at a distance r from a *galaxy 1* selected by chance, compared to a mean uniform distribution. For instance, if the galaxies are distributed in an aleatory manner following a Poisson distribution with a mean density ρ_0, the probability $dN(r)$ to find a galaxy in a volume dV_2 at a distance r from *galaxy 1* in the volume dV_1 is the fraction of galaxies in $dV_1 \times$ the fraction of galaxies in dV_2:

$$dN = \rho_0^2 dV_1 dV_2 \tag{2.31}$$

When we write the *Poissonian* distribution, we mean that the mean properties are identical, whatever the size or the place of the sample considered. In other words, galaxies are placed by chance and independently from each other, with a homogenous spatial probability. It follows that the spectrum of such a distribution is flat: this is the distribution of a ***white noise***, also referred to as ***shot noise***. If the distribution of the galaxies changes lightly for a Poissonian distribution, the probability will be

$$dN = \rho_0^2 (1 + \xi_{gal}(r)) dV_1 dV_2 \tag{2.32}$$

where $\xi(r)$ is the two–points correlation function of the galaxies. We used r instead of $\vec{r}$ with the hypothesis of the isotropy of the distribution. $\xi_{gal}(r) > 1$ indicates a sur-density, $\xi_{gal}(r) = 0$ indicates a galaxy density equal to the mean density and $\xi_{gal}(r) < 0$ indicates an under-density.

The probability of finding a galaxy at a distance r from an other one can therefore be written with equation 2.31

$$dN(x, r) = \rho_{gal}(x) dV_1 \rho(x + r) dV_2 \tag{2.33}$$

The contrast density for galaxies is

$$\delta_{gal}(x) = \frac{\rho_{gal}(x) - \rho_0}{\rho_0} \quad \Longrightarrow \quad \rho_{gal}(x) = \rho_0(1 + \delta_{gal}(x)) \tag{2.34}$$

and we use it to connect equation 2.31 with equation 2.32

$$\begin{aligned} dN(r) = \langle dN(x,r) \rangle &= \rho_0^2 \left(1 + \langle \delta_{gal}(x)\delta_{gal}(x+r) \rangle\right) dV_1 dV_2 \\ &= \rho_0^2 (1 + \xi_{gal}(r)) dV_1 dV_2 \end{aligned}$$

It follows that

$$\boxed{\xi_{gal}(r) = \langle \delta_{\rho_{gal}}(x)\delta_{\rho_{gal}}(x+r) \rangle} \qquad \text{(Autocorrelation)}$$

The Autocorrelation equation is the quantity measured by galaxy surveys.

It has been shown that the distribution of baryonic matter traces that of dark matter. This is expressed by relating the contrast density of dark matter δ_{CDM} to that of a tracer (galaxy, quasar, ionized gas...) through a ***bias factor*** b_t

$$\boxed{\delta_t = b_t \cdot \delta_{CDM}} \qquad \text{(Bias factor)}$$

It should be noted that the bias factor is an indicator of the clustering strength of a given tracer. The higher the bias, the stronger the clustering. $b_t = 1$ corresponds to a tracer that follows exactly the clustering of dark matter. In our example with galaxy distribution, we measure the function of **autocorrelation of the dark matter distribution** $\xi_{gal}(r) = b_{gal}^2 \langle \delta_{\rho_{CDM}}(x)\delta_{\rho_{CDM}}(x+r) \rangle$.

Chapter 3

Quasars and their Absorption Spectra

The goal of this chapter is to introduce quasars and the intergalactic medium, the astrophysical objects of interest in this manuscript, as well as give an overview of the important notions that connect intergalactic medium and quasar absorption spectra. These notions will be useful for chapter 5. Finally, we will present aspects of the epoch of reionization that will be useful for chapter 4.

3.1 Quasars

The term ***quasar*** was introduced as a contraction of *quasi-stellar radio source*, because quasars were first identified as sources of radio-wave emission in the 1950's, and in photographic images at visible wavelengths, they resembled point-like stars. Quasars originate from matter falling into a super massive black hole (SMBH) at the center of a galaxy. The falling gas forms an accretion disk. Processes inside the accretion disk causes it to loose angular momentum and as a consequence brings it closer to the event horizon of the black hole. While this happens, the accretion disk heats up and starts emitting in ultraviolet (UV, ~ 100 – 4000 Å) and soft X-rays (~ 20 – 100 Å). Hard X-rays (below 20 Å) are produced closer to the event horizon of black hole. Rapidly moving gas clouds in the potential of the SMBH produce strong emission lines in the optical (~ 4000 – 7000 Å) and ultraviolet. Over all, quasars have their maximum intensity emission at 1216 Å , the wavelength corresponding to the energy required to transition the electron of ionized hydrogen (HI) from $n = 2$ to the ground state. The super massive black hole also forms jets of energetic particles that are ejected in the direction of the poles. This is illustrated in figure 3.1.

Source: *NASA/ESA/STScI*

FIGURE 3.1: Illustration of a quasar.

3.2 Intergalactic Medium

The ***intergalactic medium***, or IGM, is *everything* that is between galaxies. This includes:

- intergalactic gas, i.e. atoms, molecules, ions whose velocity distribution closely follow that of the Maxwell–Boltzmann distribution
- intergalactic dust, i.e. small solid particles with a maximum size of a few μm
- cosmic rays, i.e. charged particles and ions with velocities much superior to that of the intergalactic gas
- magnetic field – guiding cosmic rays – and gravitational field – potentially leading to self-gravitating cloud
- electromagnetic radiation, i.e. all the light resulting from various astrophysical processes (starlight, synchrotron radiation,...) or epoch transition (CMB)

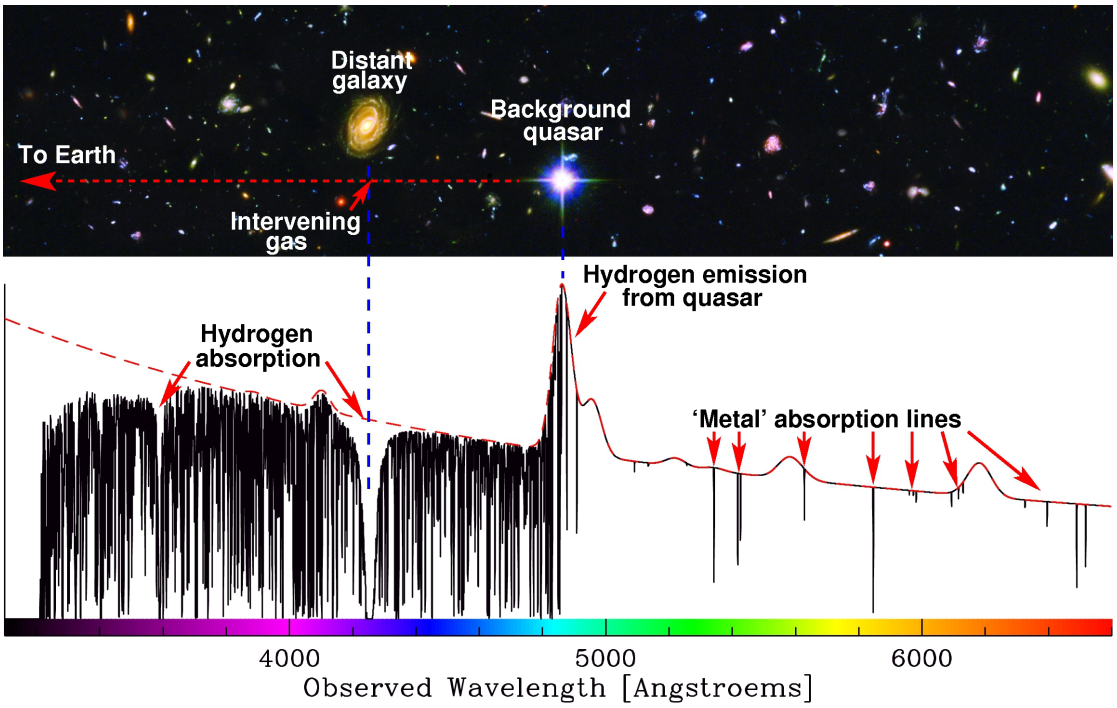

Source: *Prof. Joe Liske (University of Hamburg)*

FIGURE 3.2: Illustration of a quasar absorption spectrum and how its features highlight the medium between the quasar and the observer. Quasars act as backlight that *illuminate* the intergalactic medium.

3.3 Quasar Absorption Spectra features

A ***spectrum*** -or- electromagnetic spectrum is a measure of intensity of radiation (a) emitted by a given object, (b) absorbed by the medium between the observer and the object, per intervals of frequency. This concept is illustrated on figure 3.2, with a quasar being the object emitting the light and the IGM being the medium between the observer and the quasar. As a result, a fraction of the light emitted by a quasar is absorbed at a given wavelength in the frame of the absorber. We have seen that quasars are brighter around the wavelength associated to HI transition. With the intergalactic medium being composed at more than 70% of hydrogen, quasars being the most luminous objects in the Universe and given that the furthest observable quasars are at redshift $z \sim 6$, there is enough intensity of radiation emitted to allow an observer the opportunity to distinguish different absorption features, see figure 3.2.

In order to exploit information from observed spectra, we use the ***transmitted flux fraction***. As illustrated in figure 3.3,

$$\textit{transmitted flux fraction} = \textit{transmitted flux} \div \textit{intrinsic spectrum} \tag{3.1}$$

where the ***intrinsic spectrum***, also referred to as ***continuum***, is what we expect the observed spectrum to be if the IGM was completely transparent.

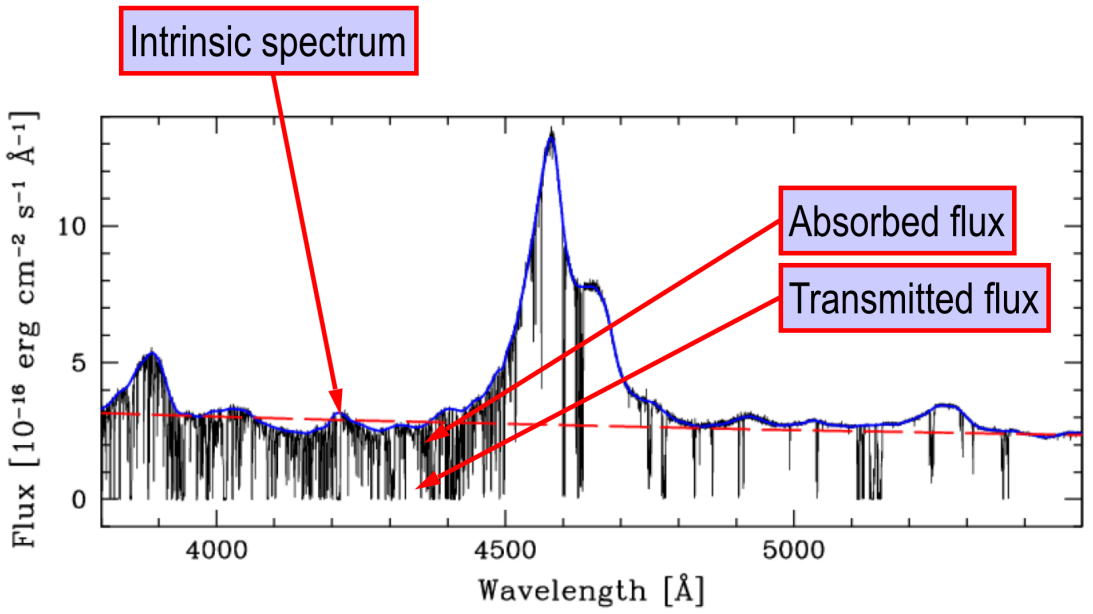

Source: *Prof. Nick Gndin (UChicago)*

FIGURE 3.3: Quasar spectrum in observed rest frame. The peak at 4600 Å is the Lyα emission peak. The zone at its left, on the *red-end* of the spectrum, is referred to as the ***Lyα forest***. The lines on the right side of the peak, on the *blue-end* of the spectrum, are metal lines – and depending on quality and redshift of the spectra, *skylines* (atmospheric absorption lines).

If we zoom in on one of the absorption feature (i.e. an absorption *line* in figures 3.2 and 3.3 spectra) we can identify different profiles. These profiles vary with the intrinsic properties of the intergalactic medium it goes through. Figure 3.4 illustrates 3 different profiles often encountered. They are characterized by their ***equivalent width*** W_λ.

$$W_\lambda = \int d\lambda \left(1 - e^{-\tau_\nu}\right) \tag{3.2}$$

where the ***optical depth*** τ_ν characterizes the absorptivity of the environment (i.e. how transparent it is for photons of a certain energy/frequency)

$$\tau_\nu = \tau_0 e^{-\left(\frac{u}{\sqrt{2}\sigma_V}\right)^2} \tag{3.3}$$

with the frequency shift from the line-center expressed as a velocity, in $km{\cdot}s^{-1}$, $u = c\frac{\nu_0 - \nu}{\nu_0}$ and σ_V the velocity dispersion. We consider that the velocity dispersion is mainly due to *local* reasons [6]

- natural broadening : the Heisenberg uncertainty principle relates the lifetime of an excited state with the uncertainty of its energy. A shorter lifetime will have a larger energy uncertainty and a broader emission. This broadening effect results in an unshifted Lorentzian profile.
- thermal Doppler broadening i.e., the distribution of velocities of the gas absorbing the radiation. The higher the temperature of the gas, the wider the distribution of velocities in this gas. This broadening effect is described by a Gaussian profile and there is no associated shift.

A ***column density*** is the number of units of matter observed along a line of sight that has an area of observation. It is the notion used to characterize the IGM gases that are responsible for the different features we observe in the quasar absorption spectra.

$$\tau_\nu = N_\lambda \frac{1}{\sqrt{2\pi}\sigma_V} \int \sigma_{cross} e^{\left(\frac{v-v_0}{\sqrt{2}\sigma_V}\right)^2} dv \tag{3.4}$$

We distinguish different categories of absorbers (profiles illustrated for HI gas with figure 3.4) :

- Lyα forest systems : ionized hydrogen gas with a column density $N_{HI} \sim 10^{13} - -10^{17}$ atoms per square centimeters.
- Lyman Limit Systems : column density a thousand times greater than Lyα forest systems i.e. $N_{HI} \sim 10^{17}$ atoms per square centimeters or higher.
- Damped Lyα Systems : self-shielding gas with a column density $N_{HI} \geq 2 \cdot 10^{20}$ atoms per square centimeters.

We have just illustrated how the absorption features we observe in quasar spectra, characterized by W_λ, relate to properties of the intervening gas $N_\lambda\,, \tau_\nu$.

3.4 A word on reionization

As seen in chapter 1, photons have continued cooling with the expansion of the Universe until recombination. Their decoupling can be observed today as the Cosmic Microwave Background (CMB) at a temperature around 2.7K. The period following the recombination is called *dark ages* and at that point the Universe is completely neutral. Fluctuations that were on the quantum level before inflation are now macroscopic and

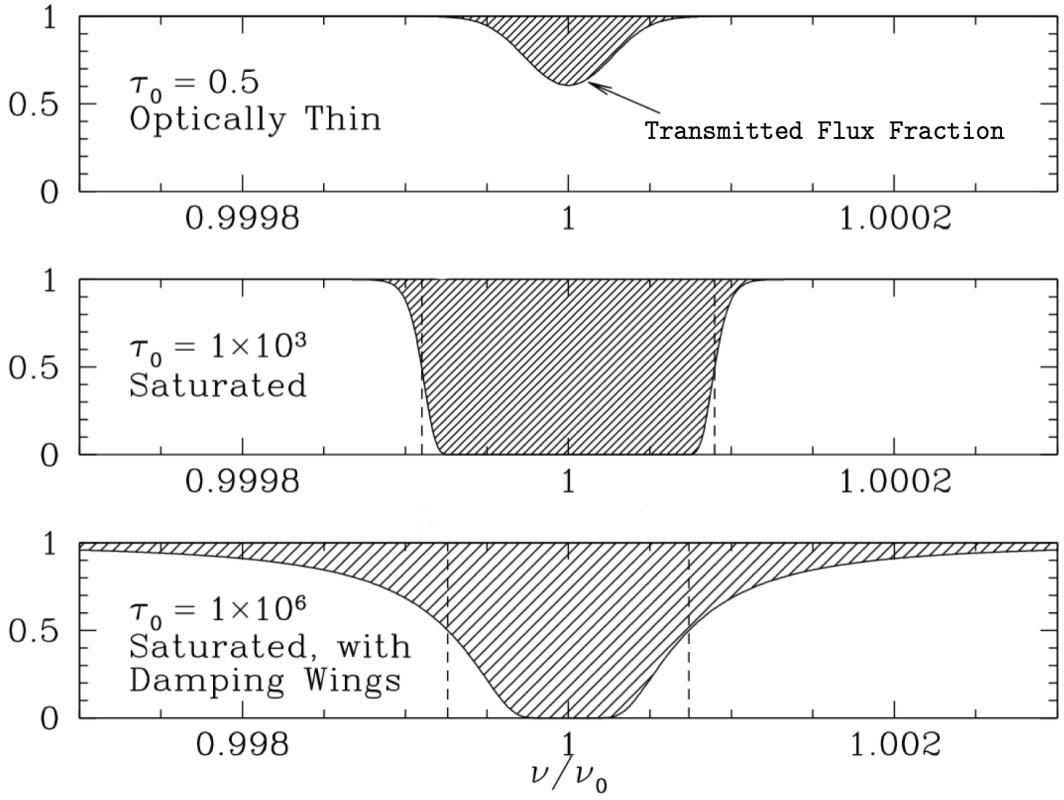

Source: *Prof. Brice T. Draine (Princeton)*

FIGURE 3.4: Absorption line profiles in three regimes, using as an example HI gas, with $b = 10\,km \cdot s^{-1}$. The upper panel has a column density $N_{HI} = 6.6 \cdot 10^{12}\,cm^{-2}$, the middle panel has $N_{HI} = 1.3 \cdot 10^{16}\,cm^{-2}$, and the lower panel has $N_{HI} = 1.3 \cdot 10^{19}\,cm^{-2}$. On the vertical axis, transmitted flux ratio = 1, corresponds to flux density from the source in the absence of absorption. Transmitted flux ratio = 0, means there was no flux to transmit by the time the observer is reached. Horizontal axis, $\nu/\nu_0 = 1$ denotes the center value of the absorption line for a given atom/molecule. The dashed zone is the absorption *line* and its width is in fact the ***equivalent width*** W_λ.

perturbations in the matter distribution grow linearly at first and, as the density peaks become non-linear, they collapse and form virialized objects (see chapter 2). When the first stars (named population III stars) and the first galaxies were formed from the baryonic matter in these virialized objects, they were metal free – almost only made of hydrogen. These stars were very massive and emitted huge amounts of UV radiation which started to re-ionize the Universe [7]. This UV radiation is also referred to as ***UV background*** or ***ionizing background***. Due to their large mass, population III stars became black holes at the end of their lives, which in turn gave rise to the first quasars. Re-ionizing radiation was increased by the apparition of these last objects. Figure 3.5 illustrates how the UV background progressively re-ionized the Universe and transitioned it out of the dark ages. This epoch is a very active field of research since it is unclear what the relative contribution of galaxies and quasars to the reionization are, how they

performed this contribution and how long the whole process took. In the following section, we will give an overview of the current state of knowledge on the contributions of galaxies and quasars to reionization.

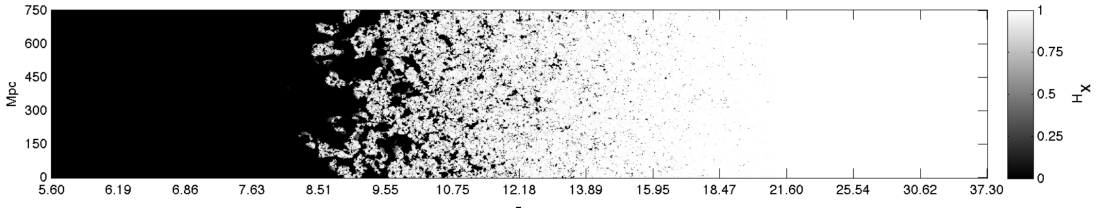

Source: *Prof. Andrei Mesinger (SNS Pisa)*

FIGURE 3.5: The predicted redshift evolution of the ionization state of the IGM in a realistic reionization model . The white/black represents fully neutral/ionized intergalactic gas. This figure demonstrates the inhomogeneous nature of the reionization process which took places over an extended range of redshifts: at $z > 16$ the first ionized regions formed around the most massive galaxies in the Universe (at that time). During the final stages of reionization - here at $z \sim 9$ the IGM contains ionized bubbles several tens of Mpc across.

3.4.1 Contribution of first galaxies to reionization

For the study on the contribution of the first galaxies to the reionization, some estimations have to be taken into account. This can provide a large uncertainty in the calculations and nowadays we only have a general idea of what happened. This being said, galaxies are believed to dominate the reionization process.

Verifying that star-forming galaxies were responsible for cosmic reionization requires under- standing how many energetic ultraviolet photons were produced by young stars at early times. In order to make this estimation, one needs to measure the luminosity function of star-forming galaxies [8]. In this case, the luminosity function is the number of star-forming galaxies per luminosity interval at a given redshift. This luminosity function has to be computed through a conversion factor, also estimated, which could be affected by several uncertainties [9]. Additional source of uncertainties when it comes to understanding this luminosity function is that it is strongly affected by dust attenuation and depends on the initial mass function – all of which are not highly constrained. Finally, there is a dependence on the escape fraction. This quantity represent the fraction of ionizing photons produced by stars that escape their host galaxies and can then ionize hydrogen in the surrounding intergalactic medium. From [9] and references therein, we see that if star-forming galaxies are the sole responsible for reionization, the escape fraction should be $\sim 20\%$ at redshift 7. However, current estimation show an escape fraction of $\sim 5\%$ as an upper limit [10]. It follows that galaxies are not the only source to contribute to the ionizing background.

3.4.2 Contribution of quasars to reionization

Unlike for star-forming galaxies, all the radiation emitted by quasars (and AGNs) is assumed to be available to reionize the intergalactic medium and not to be trapped in the quasar surroundings. Therefore we assume the escape fraction in this case to be ~ 1. Uncertainty arises because, for one, we have very little understanding of how quasars evolve with time. And also, the shape of the faint end of the luminosity function of quasars is not measured accurately. Additionally, it is unclear what the fraction of population III stars give rise to a black hole is, and how many cloud-collapse black holes can be created in the early stages of the reionization period. Current studies look at the ionizing photon rate per unit comoving volume (see [11]). Using this formalism and considering an estimation for the faint end of the luminosity function of quasars, it can be seen in [9] that the contribution of quasars is significant at redshift $z \sim 6$ but insufficient to provide an ionizing photon rate to make them the sole contributor to reionization. At higher redshift the contribution is even smaller and in order to be significant, a steeper faint-end of the luminosity function is required.

Final word

As we have seen, it is difficult to make a clear statement on the sources of reionization, their contributions, and the evolution of these contributions through time. It seems that at redshift $z \sim 6$, quasars could contribute what is missing from star-forming galaxies. However at higher redshifts, that is not the case. Recent studies suggest that there could be an evolution of the escape fraction – it would increase with redshift. Other explanations propose that dwarf galaxies and individual stars contributions might be underestimated... The study of the epoch of reionization and its processes is a very active field of research.

Part II.

Exploring the Universe with Quasar Absorption Spectra

Chapter 4

On the effect of the ionizing background on the Lyα forest autocorrelation function

An analytical framework is presented to understand the effects of a fluctuating intensity of the cosmic ionising background on the correlations of the Lyα forest transmission fraction measured in quasar spectra. In the absence of intensity fluctuations, the Lyα power spectrum should have the expected cold dark matter power spectrum with redshift distortions in the linear regime, with a bias factor b_δ and a redshift distortion parameter β that depend on redshift but are independent of scale. The intensity fluctuations introduce a scale dependence in both b_δ and β, but keeping their product $b_\delta\beta$ fixed. Observations of the Lyα correlations and cross-correlations with radiation sources like those being done at present in the BOSS survey of SDSS-III [12–14] have the potential to measure this scale dependence, which reflects the biasing properties of the sources and absorbers of the ionising background. We also compute a second term affecting the Lyα spectrum, due to shot noise in the sources of radiation. This term is very large if luminous quasars are assumed to produce the ionising background and to emit isotropically with a constant luminosity, but should be reduced by a contribution from galaxies, and by the finite lifetime and anisotropic emission of quasars.

This chapter is a reproduction of my work published in MNRAS [15].

4.1 Introduction

The Lyα forest absorption measured in spectra of high-redshift quasars has now been established as a powerful tracer of large-scale structure. Assuming that the intrinsic continuum spectrum of the observed quasar can be accurately modelled, then the observed flux divided by the fitted continuum yields the transmitted fraction, $F = e^{-\tau}$ (where τ is the optical depth), at every wavelength pixel. This one-dimensional map that is obtained from the spectrum of every observed source is related (neglecting the contamination by metal lines) to the gas density, temperature and peculiar velocity of the hydrogen gas in the intergalactic medium that is intercepted by the line of sight.

After the initial measurements of the Lyα power spectrum along the line of sight from individual spectra [16–20], the first determination of the power spectrum of the Lyα forest in three-dimensional redshift space came with the BOSS survey of SDSS-III [21, 22]. Analysis of the first 14000 quasars led to the detection of redshift space distortions [23], as expected in a simple biased linear theory where the Lyα power spectrum follows that of the dark matter with two bias parameters, reflecting the large-scale variation of the mean Lyα transmission with the fluctuation in the mean mass density and peculiar velocity gradient.

However, large-scale fluctuations in the Lyα forest can also be affected by variations in the intensity of the ionising background radiation, as well as the imprint that reionisation may have left on the gas temperature distribution as a function of gas density. These effects have been studied and discussed by several authors in the past. Analytic models of randomly distributed sources were considered by [24], and numerical realizations of random sources to compute the fluctuation properties of the ionising background were used in several subsequent papers [17, 25–29]. The impact of these ionising background fluctuations on the Lyα forest were found to be generally small compared to the intrinsic Lyα forest fluctuations due to the large-scale structure of the mass distribution. However, as pointed out in the early work of [17], the long mean free path of ionising radiation in the intergalactic medium at $z \sim 3$ implies that the fluctuations induced by the ionising background can become relatively more important in the limit of very large scales. These large scales are now becoming highly relevant with the recent detections of the BAO peak in the Lyα forest [12–14, 30].

In this paper we reanalyse with an analytic method the impact of large-scale fluctuations in the ionising radiation intensity and the gas temperature-density relation on the observable redshift space Lyα power spectrum. There are two independent effects on the power spectrum. The first arises from the clustering of sources and absorbers of radiation, which are assumed to trace the large-scale mass density fluctuations, each with

their own bias factor. This clustering term is independent of the luminosity function, variability and anisotropic emission of the sources, as well as the size or other geometric properties of the absorbers: it depends only on how the density of sources and absorbers follow the underlying large-scale structure. The second effect is due to the fluctuations in the radiation intensity that arises from shot noise in the number of sources. This second term is independent of the source clustering, but depends on other source characteristics like the luminosity function. An analytical framework to treat these contributions to the Lyα power spectrum is described in section 2, and results for simple illustrating models are presented in section 3, with a discussion and conclusions in section 4. We use a Cold Dark matter cosmological model with parameter values that are consistent with the [31]: $H_0 = 67.3\ \mathrm{km\,s^{-1}\,Mpc^{-1}}$, baryon density $\Omega_b h^2 = 0.02205$, $\Omega_m = 0.315$, $n_s = 0.96$ and $\sigma_8 = 0.856$.

As this paper was being finalized, we became aware of the work by [32], presenting very similar ideas as here. We mention in section 4 the similarities and differences between the two papers.

4.2 Analytic Formalism

The use of the Lyα forest as a tracer of large-scale structure lies on the principle that, when averaged over a large scale, the mean value of the transmission fluctuation through the Lyα forest, $\delta_\alpha = F/\bar{F}(z) - 1$ (where F is equal to the observed flux divided by a model quasar continuum, and $\bar{F}$ is the mean value of F over all the universe at redshift z), has a linear relation to the local deformation tensor of large-scale structure when smoothed in the same way over a large scale. On small scales, the distribution of δ_α and its correlations have a complex dependence on the physics of non-linear collapse of the intergalactic gas into filaments and halos, and the shock-heating, ionisation and cooling of the gas. However, on large scales all these effects are absorbed into a first order dependence of δ_α on the local deformation tensor in the linear regime [e.g., 33],

$$\frac{1}{H(z)}\frac{\partial v_i}{\partial x_j}\ , \tag{4.1}$$

where $\mathbf{v}$ is the peculiar velocity smoothed over a large scale in the same way as F, x is the comoving coordinate, and $H(z)$ is the Hubble constant at redshift z. For an observer measuring F along a direction specified by a unit vector $\mathbf{n}$, there are two first-order scalars that can be obtained from the deformation tensor: its trace, $H^{-1}\partial v_i/\partial x_i = f(\Omega_m)\delta$, where $f(\Omega_m) = d\log D(a)/d\log a$ is the logarithmic derivative of the growth factor $D(a)$, and the peculiar velocity gradient along the line of sight, $\eta = n_i n_j(\partial v_i/\partial x_j)/H$. Therefore, the fluctuation in the Lyα transmission must be given to first order by a linear

combination of δ and η, with two bias factors, $b_\delta = \partial\delta_\alpha/\partial\delta$ and $b_\eta = \partial\delta_\alpha/\partial\eta$, with numerical values that depend on redshift and on the small-scale physics of the intergalactic gas (McDonald et al. 18, McDonald 34, Slosar et al. 28, Slosar et al. 23). Whereas galaxy surveys require only one bias factor to relate galaxy density to mass density fluctuations, the Lyα forest requires two of them because of the non-linear transformation from the Lyα optical depth to the observed transmission fraction, which alters the dependence on the direction vector of the observation $\mathbf{n}$.

This dependence on δ and η is only valid, however, if one assumes that no other independent physical quantities that are correlated on large scales can affect the value of δ_α; in particular, a homogeneous ionising background intensity is assumed. The quantity that matters for determining the Lyα transmission is the photoionisation rate, $\Gamma(\mathbf{x})$, obtained from the integration over frequency of the background intensity times the cross section. Its fluctuation is $\delta_\Gamma(\mathbf{x}) = \Gamma(\mathbf{x})/\bar{\Gamma} - 1$. Including these large-scale variations of the photoionisation rate, the total Lyα transmission fluctuation smoothed over a large scale is

$$\delta_\alpha(\mathbf{x}) = b_\delta\delta(\mathbf{x}) + b_\eta\eta(\mathbf{x}) + b_\Gamma\delta_\Gamma(\mathbf{x}) \ . \tag{4.2}$$

where b_Γ is now a third bias factor for the photoionisation rate. Therefore, the total Lyα correlation depends now not only on the correlations of δ and η (which are related to the primordial linear power spectrum with redshift distortions), but also on the correlation of δ_Γ with itself, δ and η. We now compute these correlations, and we will do this taking into account two different effects: the fact that sources are clustered and trace the mass fluctuations, and the shot noise due to the random distribution of discrete sources.

4.2.1 Source Clustering

We assume that the sources of the ionising background have a spatial distribution tracing the mass density field, with a bias factor b_s, so the mean large-scale overdensity of sources is $\delta_s = b_s\delta$. In addition, the ionising radiation is being absorbed by a population of absorbers, which are Lyman limit systems as well as absorption systems with Lyman continuum optical depths below unity that have a comparable contribution to the overall absorption. This population of absorbers has a large-scale distribution that is affected by both the underlying mass density fluctuations and the radiation intensity fluctuations. So, the absorber density fluctuation can be written as $\delta_a = b_a\delta + b'_a\delta_\Gamma$. We expect these absorbers to increase in high density regions and decrease in response to an increased ionising intensity, so b_a should be positive and b'_a should be negative.

Even though the opacity to ionising photons depends on frequency, and a detailed treatment has to include the intensity spectrum and the combined effect of absorption and

redshift modifying the background spectrum compared to that emitted by the sources, here we shall treat the opacity as a single quantity, neglecting the effect of redshift. The opacity due to absorbers with density fluctuation δ_a is $\kappa(\mathbf{x}) = \kappa_0[1 + \delta_a(\mathbf{x})]$, where the average mean free path for an ionising photon is $\lambda_0 = \kappa_0^{-1}$. The radiation intensity fluctuation at a point $\mathbf{x}$ due to the combination of all sources at any position $\mathbf{x}$+$\mathbf{r}$ is

$$\delta_\Gamma(\mathbf{x}) = \int d^3r\, \kappa_0 \frac{[1 + \delta_s(\mathbf{x} + \mathbf{r})]e^{-\tau(\mathbf{x},\mathbf{r})} - e^{-\kappa_0 r}}{4\pi r^2} \tag{4.3}$$

where r is the modulus of the vector $\mathbf{r}$. Defining also $\mathbf{u}_r$ to be the unit vector in the direction $\mathbf{r}$, the optical depth from $\mathbf{x}$ to $\mathbf{x}$+$\mathbf{r}$ is:

$$\tau(\mathbf{x}, \mathbf{r}) = \int_0^r dy\, \kappa_0[1 + \delta_a(\mathbf{x} + y\mathbf{u}_r)] = \kappa_0 r \left[1 + \int_0^r \frac{dy}{r}\delta_a(\mathbf{x} + y\mathbf{u}_r)\right] . \tag{4.4}$$

Neglecting second order terms in δ_s and δ_a, equation (4.3) is simplified to

$$\delta_\Gamma(\mathbf{x}) = \int \frac{d\mathbf{u}_r}{4\pi} \int_0^\infty dr\kappa_0\, e^{-\kappa_0 r} \cdot \left[\delta_s(\mathbf{x} + r\mathbf{u}_r) - \kappa_0 \int_0^r dy\, \delta_a(\mathbf{x} + y\mathbf{u}_r)\right] . \tag{4.5}$$

For the second term involving the absorbers, the order of the integrals over r and y can be inverted, and we find:

$$\begin{aligned} \int_0^\infty dr\kappa_0^2 e^{-\kappa_0 r} \int_0^r dy \delta_a(\mathbf{x} + y\mathbf{u}_r) &= \int_0^\infty dy\, \kappa_0^2 \delta_a(\mathbf{x} + y\mathbf{u}_r) \int_y^\infty dr e^{-\kappa_0 r} \\ &= \int_0^\infty dy\, \kappa_0 e^{-\kappa_0 y} \delta_a(\mathbf{x} + y\mathbf{u}_r) , \end{aligned} \tag{4.6}$$

and so finally, changing the name of the dummy variable y back to r, and reexpressing the integral in terms of the variable $\mathbf{x}$'=$\mathbf{x}$+$\mathbf{r}$,

$$\delta_\Gamma(\mathbf{x}) = \int \frac{d\mathbf{x}'}{4\pi r^2}[\delta_s(\mathbf{x}') - \delta_a((\mathbf{x}')]\kappa_0 e^{-\kappa_0 r} . \tag{4.7}$$

This result is easy to understand, because an absorber actually acts in the same way as a negative source in this linear regime.

We now replace $\delta_\Gamma(\mathbf{x})$ and $\delta_s(\mathbf{x}')$, $\delta_a(\mathbf{x}')$ in equation (4.7) by their Fourier transforms, invert the order of the integrals over $\mathbf{k}$ and $\mathbf{x}'$, and do the integral over $\mathbf{x}'$, to find that the Fourier transforms are related by

$$\begin{aligned} \delta_\Gamma(\mathbf{k}) &= [\delta_s(\mathbf{k}) - \delta_a(\mathbf{k})]\, W\left(\frac{k}{\kappa_0}\right) \\ &= [(b_s - b_a)\delta(\mathbf{k}) - b_a'\delta_\Gamma(\mathbf{k})]\, W\left(\frac{k}{\kappa_0}\right) , \end{aligned} \tag{4.8}$$

where

$$W(s) = \int_0^\infty dx \, \frac{e^{-x} \sin(sx)}{sx} = \frac{\arctan(s)}{s} \ . \tag{4.9}$$

Writing now equation (4.2) in Fourier space, and suppressing dependences on k for brevity, the correlation of the Fourier modes of the Lyα transmission fluctuation is

$$\langle \delta_\alpha \delta_\alpha \rangle = b_\delta^2 \langle \delta\delta \rangle + b_\eta^2 \langle \eta\eta \rangle + b_\Gamma^2 \langle \delta_\Gamma \delta_\Gamma \rangle + 2b_\delta b_\eta \langle \delta\eta \rangle + 2b_\delta b_\Gamma \langle \delta\delta_\Gamma \rangle + 2b_\eta b_\Gamma \langle \eta\delta_\Gamma \rangle \ . \tag{4.10}$$

Using the linear redshift distortion theory of [33], the Fourier modes of δ and η are related by $\eta = f(\Omega_m)\mu_k^2\delta$, where $\mu_k \equiv \mathbf{n}\cdot\mathbf{k}/k$, and the power spectrum without including the radiation term δ_Γ can be written as usual in the form $b_\delta^2(1+\beta\mu_k^2)^2$, where the redshift distortion parameter is $\beta = f(\Omega_m)b_\eta/b_\delta$. When the radiation term is included and expressed as a function of δ using equation (4.8), we find that the total Lyα power spectrum is given by

$$P_\alpha(k,\mu_k) = P_L(k)\, b_\delta'^2(k) \left[1 + \beta'(k)\mu_k^2\right]^2 \ , \tag{4.11}$$

where

$$b_\delta'(k) = b_\delta + b_\Gamma \frac{(b_s - b_a)W(k/\kappa_0)}{1 + b_a' W(k/\kappa_0)} \ , \quad \text{and} \quad \beta'(k) = b_\delta\beta/b_\delta'(k) = b_\eta f(\Omega_m)/b_\delta'(k) \ . \tag{4.12}$$

Therefore, the effect of the photoionisation rate fluctuations that is induced by the clustering of sources and absorbers is to modify the bias factor and redshift distortion parameter in the power spectrum, replacing them with the effective values b_δ' and β' that are scale dependent, while their product $b_\delta'\beta' = b_\delta\beta$ remains fixed. At small scales, W is very small and the bias factor has its usual value $b_\delta' = b_\delta$. But in the limit of large scales, W approaches unity and b_δ' reaches the asymptotic value of $b_\delta + b_\Gamma(b_s - b_a)/(1 + b_a')$.

We now interpret physically the variation of the effective bias b_δ' with the Fourier scale k. We mention first that any realistic model for the absorbers needs to have $0 > b_a' > -1$: the density of absorbers (which we identify with the observed population of Lyman limit systems, as well as lower column density systems that also contribute to the global absorption of ionising photons) needs to decrease with δ_Γ as the increased photoionisation reduces the size of the absorbing regions, but the relative fluctuation in absorbers cannot be reduced faster than that in the ionising intensity because this would imply a runaway unstable process where any slight increase in emission leads to an arbitrarily large increase in the mean free path and the ionising intensity as the absorbers are completely ionised. Moreover, the sign of b_δ is negative while that of b_Γ is positive, so if $b_s > b_a$, the effective bias factor b_δ' decreases in absolute value with scale. The simple interpretation is that on scales large compared to the mean free

path of ionising photons, denser regions also have a greater ionising intensity, and so the corresponding increase of Lyα absorption that is caused by the higher density is reduced. If $b_\Gamma(b_s - b_a)/(1 + b'_a)$ is larger than $-b_\delta$, then the value of b'_δ is actually positive in the limit of large scales. Ignoring for now the effect of the peculiar velocity gradient (we return to this in section 3), this means that the effect of the higher ionising intensity overwhelms that of the higher mass density, causing denser regions to have an increased Lyα transmission (or reduced absorption), opposite to the behavior on small scales. In this case, there needs to be a critical scale k_r where b'_δ has a root, and the only surviving term for the power spectrum in equation (4.11) is $P_\alpha(k_r) = P_L(k_r)(b_\delta \beta \mu_k^2)^2$. In practice, the power spectrum near $\mu_k = 0$ can never quite go down to zero owing to the shot noise from individual sources of radiation, as discussed below, as well as non-linear effects from small scales which we are not including here, but a change of sign of b'_δ as a function of scale still implies the presence of a dip in the power spectrum at small μ_k which should be measurable in the observations.

4.2.2 Shot noise from individual sources

Our treatment so far includes only the correlation of sources and absorbers with the matter density fluctuations. Next, we consider the term that is added to the correlation function because of the shot noise from individual sources. We assume that all the ionising sources emit their radiation isotropically at a constant luminosity. As we shall discuss below, this assumption is crucial for our computation of the shot noise term, even though it does not affect the source clustering term calculated above. We start defining the source luminosity function, per unit of volume, as $\Phi(L)$. The mean emissivity of the ionising sources is

$$\epsilon_q = \int_0^\infty dL \Phi(L) L \ . \tag{4.13}$$

If all the sources have the same luminosity, the power spectrum of the relative emissivity fluctuations is simply equal to the inverse of the source density, $1/n_s = L/\epsilon_q$. With a distribution of luminosities, the fraction of the emissivity provided by sources of luminosity L is $L\Phi(L)\, dL/\epsilon_q$, and therefore the overall power spectrum is equal to the constant

$$4\pi C = \int_0^\infty dL \, \frac{\Phi(L) L^2}{\epsilon_q^2} \ , \tag{4.14}$$

where we have introduced the factor 4π in the definition of C for later convenience. The intensity correlation can now be obtained by multiplying by the kernel in equation (4.9), and applying the Fourier transform. It is also instructive, however, to directly compute the correlation function by considering the correlated intensity at two spatial positions

separated by a distance x caused by the flux that arrives at the two points from the same individual sources.

We choose one of the two spatial positions to be at the origin of coordinates, $\mathbf{r} = 0$, and the other one to lie on the x-axis at a distance x. The ionising intensity fluctuation at the origin is

$$\delta_\Gamma(\mathbf{r}=0) = \sum_i \frac{L_i}{4\pi r_i^2} \frac{\kappa_0 e^{-\kappa_0 r_i}}{\epsilon_q} - 1 \ , \tag{4.15}$$

where the sum is over each source i located at a distance r_i from the origin. The intensity fluctuation at $\mathbf{x}$ is similarly expressed, replacing r_i by $|\mathbf{r}_i - \mathbf{x}|$. Using the fact that the probability per unit of volume to find a source of luminosity L within dL at any point $\mathbf{r}_i$ is $\Phi(L)\, dL$, the correlation function of δ_Γ is then obtained as

$$\xi_\Gamma(x) = \langle \delta_\Gamma(\mathbf{r}=0)\delta_\Gamma(\mathbf{x})\rangle = \frac{C}{4\pi} \int d^3r \frac{\kappa_0^2 e^{-\kappa_0(r+|\mathbf{r}-\mathbf{x}|)}}{r^2|\mathbf{r}-\mathbf{x}|^2} \ .$$

We compute this integral by transforming $\mathbf{r}$ to spherical coordinates. Defining $\mu = \mathbf{r}\cdot\mathbf{u}_x/r$, where $\mathbf{u}_x$ is the unit vector along the x-axis, and changing r to the variable $s = r/x$, the result is

$$\xi_\Gamma(x) = C\kappa_0^2 \int_0^\infty \frac{ds}{x} \cdot \int_{-1}^1 d\mu \, \frac{\exp\left[-\kappa_0 x \left(s + \sqrt{1+s^2-2s\mu}\right)\right]}{1+s^2-2s\mu} \ . \tag{4.16}$$

This can be further reexpressed in terms of the exponential integral function, $E_i(x) = -\int_{-x}^\infty dt\, e^{-t}/t$. The final expression for the intensity correlation function is

$$\xi_\Gamma(x) = \frac{C\kappa_0^2}{x} A(\kappa_0 x) \ , \tag{4.17}$$

where the dimensionless function A is (replacing $\kappa_0 x = \tau$ and $\kappa_0 r = \rho$)

$$A(\tau) = \int_0^\infty d\rho \, \frac{e^{-\rho}}{\rho} \cdot \left[E_i\left(-\rho\sqrt{1+\frac{\tau^2}{\rho^2}}\right) - E_i\left(-\rho\left|1-\frac{\tau}{\rho}\right|\right)\right] \ . \tag{4.18}$$

The function A is plotted in Figure 4.1.

The sources that dominate the fluctuations in the ionising radiation intensity are the most luminous ones, which are well known from observations of the quasar luminosity function. We now estimate the constant C from recent measurements of the quasar luminosity function by [35], who used the BOSS survey of the SDSS-III Data Release 9 [see 21, 22, 36]. The quasar luminosity function was fitted to a double power-law of the form,

$$\Phi_q(L)dL = \frac{\Phi_*/L_*}{(L/L_*)^{-\alpha} + (L/L_*)^{-\gamma}} \, dL \ . \tag{4.19}$$

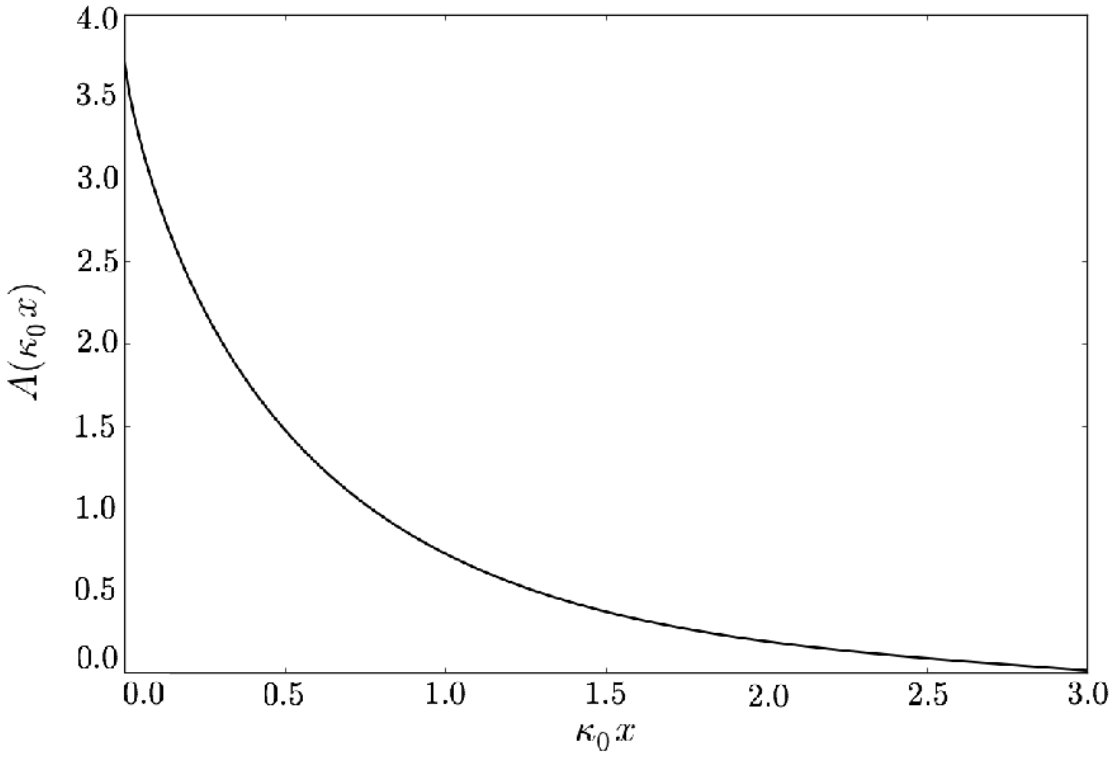

FIGURE 4.1: The dimensionless function A defined in equation (4.18), giving the shape of the intensity correlation function due to a set of randomly distributed, isotropic and constant sources of radiation.

The values of the fitted parameters obtained by Ross et al. [35] are $\alpha = 1.52$, $\gamma = 3.10$, and $\Phi_*^{(R)} = 10^{-6.37}\,\mathrm{Mpc}^{-3}\mathrm{mag}^{-1}$, where they defined $\Phi_*^{(R)}$ to be a number density of quasars per unit of absolute magnitude. We convert their value $\Phi_*^{(R)}$ to our cosmological model, at $z = 2.25$ (the model used by Ross et al. [35] had $\Omega_m = 0.30$ and $H_0 = 70\,\mathrm{km\,s^{-1}\,Mpc^{-1}}$) and to our units, finding $\Phi_* = 1.42 \times 10^{-6}(\,h^{-1}\,\mathrm{Mpc})^{-3}$. With these numbers, we compute the quantity C_q for quasars using equation (4.14), and we find $C_q = 9.5 \times 10^4(\,h^{-1}\,\mathrm{Mpc})^3$. Note that the value of C_q is independent of L_*, and depends only on Φ_* and the shape of the luminosity function. The value of C_q diverges as γ approaches 3, so the fitted value of $\gamma = 3.1$ from [35] implies a large uncertainty of C_q depending on the exact shape of the luminosity function at the high luminosity end.

The intensity of the ionising background is likely to have a contribution from galaxies, in addition to quasars. Assuming that all galaxies are much less luminous than the quasars that contribute appreciably to the constant C_q, then the faint galactic sources can increase the mean intensity, but can be neglected for the fluctuations, i.e., their contribution to the integral $\int dL\,\Phi(L)L^2$ is negligible. In that case, equation (4.14) implies that the emissivity power spectrum amplitude is determined by the constant

$$C = \frac{\epsilon_q^2 C_q}{(\epsilon_g + \epsilon_q)^2}\ , \tag{4.20}$$

where ϵ_g and ϵ_q are the emissivities of galaxies and quasars. The correlation due to shot noise is therefore reduced as the contribution from galaxies to the ionising intensity is increased.

Apart from the effect of galaxies, the amplitude of the intensity correlation function contributed by shot noise from the observed quasars that is obtained from equation (4.17) ought to be considered as an upper limit only. The reason is that real quasars are likely to emit anisotropically and to be highly variable in their luminosity on the light-crossing time of the cosmological scales at which the correlations are being measured. The effects of the variability and anisotropy of the emission from individual quasars can be highly complex and difficult to model, but an order-of-magnitude estimate can be made by assuming the opposite limit in which quasars emit in very narrow cones and short bursts. If f_Ω is the fraction of the solid angle over which the light of a quasar is emitted, and f_t is the fraction of time during which a quasar is shining, and we assume that the quasar luminosity is zero outside of this fraction of solid angle and time, then the correlation function ξ_Γ in equation (4.17) is reduced by a factor $f_\Omega f_t$, because assuming that a source is being observed at a point $\mathbf{r} = 0$, the probability that it is also observed at a point $\mathbf{x}$ with the same luminosity is only $f_\Omega f_t$.

The total correlation function of the Lyα transmission is equal to the sum of the term due to source clustering, from equation (4.11), and the shot noise term in equation (4.17) multiplied by b_Γ^2.

4.2.3 Values of the bias parameters

We now discuss how the values of the various bias parameters that have appeared in our derivation of the radiation effects in the Lyα correlation function can be estimated. All the bias factors should generally depend on redshift, and our discussion here will be focused at $z = 2.25$, the redshift near which the observations of Lyα correlations have so far been done with the BOSS survey.

We start with the bias factor that relates the ionising intensity fluctuations to the Lyα transmission fluctuations. As described in [37] (see their equation 5.4), this bias factor can easily be calculated from its definition as $b_\Gamma = \partial\delta_\alpha/\partial\delta\Gamma$, where the values δ_α and δ_Γ are smoothed over sufficiently large, linear scales, if the true, unsmoothed distribution of the Lyα transmission is known, and under two additional assumptions: photoionisation equilibrium in a highly ionized medium (neglecting any contribution from collisional ionisation), and that any changes of temperature and hydrodynamic evolution of the intergalactic gas with the ionising background intensity can be neglected (in a more detailed treatment, small temperature variations would likely be induced by changes in

the spectral shape of the ionising background rather than its intensity). In this case, the effect of the ionising intensity fluctuations is simply to divide the Lyα optical depth by a factor $1 + \delta_\Gamma$ at every pixel in the spectrum. If $P(F)$ is the unsmoothed probability distribution of F, one obtains

$$b_\Gamma = -\frac{1}{\bar{F}} \int_0^1 dF\, P(F)\, F\, \log(F)\ . \tag{4.21}$$

At $z = 2.25$, the distribution of the Lyα optical depth, $\tau = -\log F$, can be approximated as a log-normal function, constrained to produce a mean transmission $\bar{F} = 0.8$ and a dispersion in the transmission $\sigma_F = 0.124$. This distribution yields a value $b_\Gamma \simeq 0.13$.

The values of b_δ and b_η have to be measured observationally. They are related to the redshift distortion parameter by $\beta = f(\Omega_m) b_\eta / b_\delta$ [33]. Measurements from the Lyα forest correlation in the scale range $10 - 60\, h^{-1}$ Mpc in [23] resulted in a good measurement of $b_\delta(1 + \beta) = -0.336 \pm 0.012$ at $z = 2.25$, with a more poorly constrained $\beta \sim 1$. We shall assume $\beta = 1$, which is also favored by the measurement of cross-correlations (see Font-Ribera et al. 38, 2013), and $b_\delta = -0.17$ (so $b_\eta = \beta b_\delta / f(\Omega_m) \simeq -0.17$; note that the negative sign of b_δ and b_η results from the convention that δ_α is a transmission fluctuation, which is therefore negative when the mass density perturbation is positive). These observational results may change in the future since they were obtained by neglecting the radiation effects that are examined here, and they are subject to other possible systematic errors [e.g., 39].

For the bias of the sources, quasars have had their bias factor measured from their auto-correlation [40, and references therein] and cross-correlation with the Lyα forest [37], resulting in values in the range 3.5 to 4. The actual bias of the sources, however, depends also on the contribution that galaxies make to the ionising background intensity and on the bias factor of these galaxies. If the bias factors of quasars and galaxies are b_q and b_g, then $b_s = (\epsilon_q b_q + \epsilon_g b_g)/(\epsilon_q + \epsilon_g)$. Galaxies are on average associated with lower-mass halos than quasars, so their bias factor should be smaller and therefore b_s should be lower than b_q.

The population of absorbers determining the mean free path of the ionising radiation is dominated by systems that have an optical depth of order unity at the Lyman limit, with column densities $\sim 1.6 \cdot 10^{17} \mathrm{cm}^{-2}$. Note that only systems with column densities above this value are usually referred to as Lyman limit systems, but absorbers of lower column density are about equally important [e.g., 41, 42]. The bias factor has only been measured for systems of higher column densities, the damped Lyα systems [38], and a value $b_a \simeq 2$ was obtained. Lyman limit systems are of lower column density than the damped systems but they should have a similar bias factor if halos of all

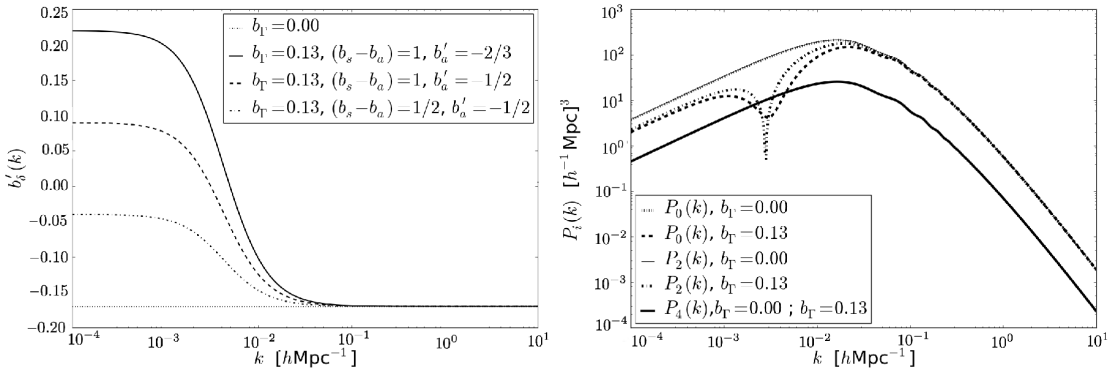

FIGURE 4.2: Effective bias (left) and power spectrum (right) of the Lyα forest, for several values of the bias parameters regulating the clustering strength of sources minus absorbers ($b_s - b_a$) and the response of the absorbers to the ionising intensity (b'_a). The dotted line is for no radiation effects, and the solid line in the left panel is for our fiducial radiation model. The mean free path is fixed to $\lambda_0 = 300\,h^{-1}$ Mpc. The right panel shows the monopole, quadrupole and hexadecapole of the power spectrum, for the cases of no radiation fluctuations and for our fiducial radiation model.

masses give rise to the same distribution of hydrogen column densities, depending on the impact parameter. However, a population of low-mass halos might exist in which the self-shielded gas does not reach as high column densities as in high-mass halos, which would then reduce the mean bias factor of the Lyman limit systems. Both b_s and b_a are therefore rather uncertain. The effective Lyα forest bias depends only on the difference $b_s - b_a$ (see equation 4.12), for which we shall assume a fiducial value $b_s - b_a = 1$.

Finally, the bias factor controlling the response of the absorbers to changes in the ionising intensity can be related to the column density distribution of Lyman limit systems, which we model as a power-law, $f(N_{HI})\,dN_{HI} \propto N_{HI}^{-a}\,dN_{HI}$. This implies a radial profile of the column density in spherical halos $N_{HI} \propto r^{2/(1-a)}$. In photoionisation equilibrium, the column density at a fixed radius r outside the region where the gas starts to self-shield will vary in proportion to the inverse of the photoionisation rate. The self-shielding radius r_s occurs at a fixed column density, and will therefore change as $r_s \propto \Gamma^{(1-a)/2}$ in response to a change of the external ionising intensity. The cross section to produce a Lyman limit system scales as r_s^2, so the number of absorbers that are intercepted per unit length should scale as Γ^{1-a}. For small changes in Γ this implies a bias factor $b'_a = 1 - a$. We shall use here $a = 5/3$ (the value corresponding to a gas density profile $\rho_g \propto r^{-2}$, and $N_{HI} \propto r^{-3}$), and therefore $b'_a = -2/3$.

With the values we adopt here for the fiducial model, the value of $b'_\delta(k)$ in equation (4.12) is plotted in the left panel of Figure 4.2, as the solid line. Here and in the rest of the paper, we use a mean free path $\lambda_0 = 300\,h^{-1}$ Mpc as our fiducial value. Observational estimates of the mean free path of an ionising photon for being absorbed by hydrogen in the intergalactic medium or Lyman limit systems give a value $\lambda_0 \simeq 350\,h^{-1}$ Mpc [43].

Our approximate treatment in section 2.2 neglects the redshift of the photons, which effectively acts in the same way as an additional source of opacity with a comoving mean free path of the order of the horizon, $c(1+z)/H(z) \simeq 3000\,h^{-1}$ Mpc. The effective overall mean free path is therefore close to our fiducial value of $300\,h^{-1}$ Mpc.

The two other curves in Figure 4.2 are for variations of the bias values that will be used in section 3. For our fiducial model, $b'_\delta(k)$ is positive in the limit of large scales and negative at small scales, and therefore changes sign at a critical scale k_r. Depending on the uncertain values of all the bias factors we have discussed, this critical scale can have very different values, and is likely to vary substantially with redshift.

4.2.4 Fluctuations due to helium reionisation

In addition to the intensity of the ionising background, the intergalactic medium may be affected by other physical elements that are correlated over large scales. Here we consider as another possibility the imprint that may have been left by helium reionisation in the temperature of the intergalactic gas. At the mean baryonic density of the universe, the recombination time at $z = 2.25$ is much longer than the age of the universe, and so is therefore the cooling time of photoionised gas. As helium is doubly ionised for the first time, probably by luminous quasars at $z \simeq 3$ [44, and references therein], the gas is heated to a spatially variable temperature depending on the spectrum and luminosity of the sources producing the ionisation fronts that eventually overlap when reionisation ends [e.g., 45, 46]. The long cooling time then implies that the gas temperature at every spatial location may keep a memory of the time at which helium reionisation occurred, or the spectral shape of the sources, or other characteristics that were imprinted at the reionisation time. If the temperature fluctuates according to $\delta_T = b_T \delta_{\Gamma e}$, where $\delta_{\Gamma e}$ is an intensity fluctuation of the HeII-ionising radiation that was present at the reionisation time arising from sources that may long have been dead, then the observed Lyα transmission in hydrogen would vary as $\delta_\alpha = b_e \delta_{\Gamma e}$ owing to the dependence of the recombination coefficient on temperature, which follows the approximate relation $\alpha_{rec}(T) \propto T^{-0.7}$. Using similar arguments as in section 2.3 for deriving b_Γ, we can infer that $b_e = 0.7 b_\Gamma b_T$.

If the helium-ionising radiation intensity follows the same behavior as the radiation that ionised hydrogen, with a different mean opacity κ_{0e}, a similar derivation as in section 2.1 shows that the total power spectrum that includes also the clustering term for the sources inducing the helium-reionisation perturbations is the same as in equation (4.11),

with the new bias factor

$$b'_\delta(k) = b_\delta + b_\Gamma \frac{(b_s - b_a)W(k/\kappa_0)}{1 + b'_a W(k/\kappa_0)} + b_e \frac{(b_{se} - b_{ae})W(k/\kappa_{0e})}{1 + b'_{ae} W(k/\kappa_{0e})} \ , \tag{4.22}$$

where the bias factors with the additional subscript e are the analogous ones for helium to those that were described for hydrogen in section 2.1.

4.3 Results

The correlation function of δ_α is obtained from the Fourier transform of the power spectrum in equation (4.11), which includes the source clustering term. To include the shot noise term, the correlation ξ_Γ from equation (4.17) multiplied by b_Γ^2 must be added. Following the formalism and notation of Dawson et al. [47] (see their section 2.2), the multipole terms of the power spectrum of equation (4.11) have their usual form with the new scale-dependent bias factor $b'_\delta(k)$ and redshift distortion parameter $\beta'(k)$ [33, 48]:

$$P_{\ell,\alpha}(k) = P_L(k)\, b'^{,2}_\delta(k)\, C_\ell[\beta'(k)] \ , \tag{4.23}$$

where

$$\begin{aligned} C_0 =& 1 + \frac{2}{3}\beta'(k) + \frac{1}{5}\beta'^2(k) \ , \\ C_2 =& \frac{4}{3}\beta'(k) + \frac{4}{7}\beta'^2(k) \ , \\ C_4 =& \frac{8}{35}\beta'^2(k) \ . \end{aligned} \tag{4.24}$$

(4.25)

The multipoles of the real space Lyα correlation function are

$$\xi_\ell = \frac{i^\ell}{2\pi^2} \int_0^\infty dk\, k^2 j_\ell(kr)\, P_{\ell,\alpha}(k) \ , \tag{4.26}$$

where j_ℓ are the spherical Bessel functions. Note that these correlation multipoles are no longer given by the equations in Hamilton [48] because of the scale dependence of b'_δ and β', except for the hexadecapole which does not change because $b'_\delta\beta' = b_\delta\beta$. We have used a Fast Fourier Transform method to calculate these multipoles numerically.

As shown in the left panel of Figure 4.2, the bias factor $b'_\delta(k)$ in our fiducial radiation model changes sign at a critical scale $k_r \simeq 0.005\, h/\mathrm{Mpc}$. The monopole, quadrupole and hexadecapole of the power spectrum are well defined and non-zero at $k = k_r$ because $b'_\delta\beta'$ is constant. At $k < k_r$, the redshift distortion parameter $\beta'(k)$ is negative. While the

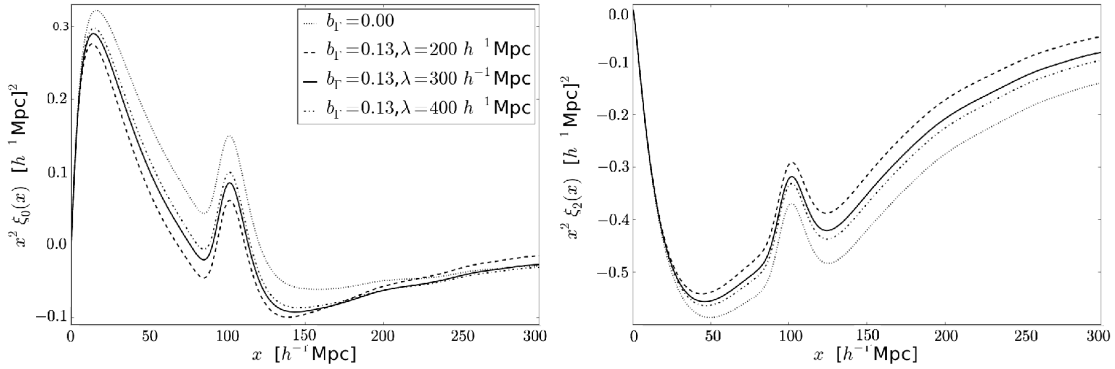

FIGURE 4.3: Monopole ($\ell = 0$, left) and quadrupole ($\ell = 2$, right) of the Lyα auto-correlation function. The dotted line is with no radiation effects, and the other three lines include them with our fiducial value of the bias factors in section 2.3 and three different values of the mean free path.

monopole is always positive for any value of β', the quadrupole is zero when $\beta'(k) = -7/3$, and becomes negative at small k, when $-7/3 < \beta' < 0$. This is seen in the right panel of Figure 4.2, where the monopole, quadrupole and hexadecapole of the power spectrum are shown for the no radiation case, and the case that includes the source clustering effect for our fiducial values of the radiation bias parameters (the power spectrum is computed for the Cold Dark Matter model with the parameters mentioned in the introduction; all results for power spectra and correlation functions in this paper are shown at $z = 2.25$). The monopole has a dip near $k = k_r$, and the quadrupole has a root at the slightly smaller value of k where $\beta' = -7/3$. The reason for this behaviour is that when b'_δ is negative on large scales, high-density regions produce reduced absorption owing to the larger ionising intensity that overwhelms the gas density effect, but the gradient of peculiar velocity counteracts that, resulting in a negative quadrupole for the power spectrum.

The monopole and quadrupole terms in the Lyα correlation for our fiducial case of the values of the bias parameters discussed in section 2.3 are shown in the two panels of Figure 4.3, multiplied for convenience by x^2. The dotted line is for a uniform ionising background. The well known Baryon Acoustic Oscillation peak appears at its characteristic scale of $\sim 100\,h^{-1}$ Mpc. The dashed, solid and dash-dot lines include the source clustering effect, with no shot noise, for three different values of the comoving mean free path: 200, 300 and $400\,h^{-1}$ Mpc (our fiducial value used in all other figures is $\lambda_0 = 300\,h^{-1}$ Mpc). This mean free path decreases rapidly with redshift, which should change the way that intensity fluctuations modify the correlation function as the redshift increases.

The radiation from clustered sources adds a broadband term that is negative in the monopole and positive in the quadrupole. This is because the absolute value of the bias

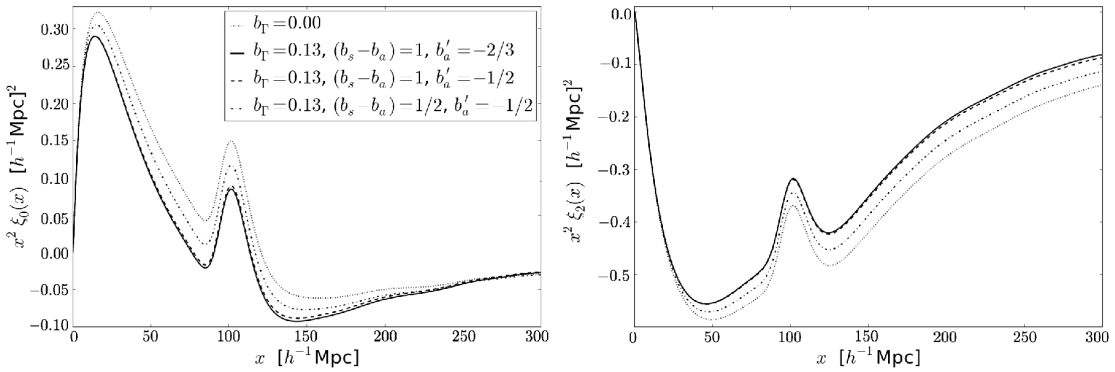

FIGURE 4.4: Monopole (left) and quadrupole (right) of the Lyα autocorrelation function, for different values of the bias parameters regulating the clustering strength of sources minus absorbers ($b_s - b_a$) and the response of the absorbers to the ionising intensity (b'_a). The dotted line is with no radiation effects. The mean free is fixed to $\lambda_0 = 300\,h^{-1}\,\mathrm{Mpc}$.

b'_δ in equation (4.12) is reduced at scales small compared to λ_0, as long as $b_s > b_a$. The shorter the mean free path, the larger the radiation effects. On scales larger than the mean free path, the impact of the radiation on the monopole becomes positive. The effects are predicted to be relatively large, and they should be measurable as long as the broadband shape can be retrieved from the data without substantial systematic errors caused by the quasar continuum fitting operation. In the observations reported so far, broadband terms were marginalised over [12–14] and therefore the effect of the ionising intensity fluctuations would not have been detected. Note that the position of the BAO peak is practically not affected; even if the peak shifts by a small amount owing to the addition of the radiation effects, any such shift should be further reduced when fitting with a parameterised broadband term.

Figure 4.4 shows how the radiation effects vary with some of the bias parameters (again, with the monopole on the left panel and the quadrupole on the right panel). The dotted line (no radiation effects) and the solid line (for the fiducial values of the bias parameters in section 2.3) are the same as in Figure 4.3. The dashed line shows that the radiation effect is very insensitive to b'_a on scales small compared to λ_0. The dash-dot line has a reduced value of $b_s - b_a$, and shows that the radiation effect is basically proportional to this bias difference between sources and absorbers.

Observations of the correlation function (or one-dimensional power spectrum) can also be done exclusively on the line of sight [20, 49]. The correlation function along the line of sight is equal to the sum of all the multipoles. The result is shown in Figure 4.5 for some of the same models shown in Figures 4.3 and 4.4. This figure shows that the correlation along the line of sight on scales small compared to the mean free path is much less affected by the radiation fluctuations than the three-dimensional correlation.

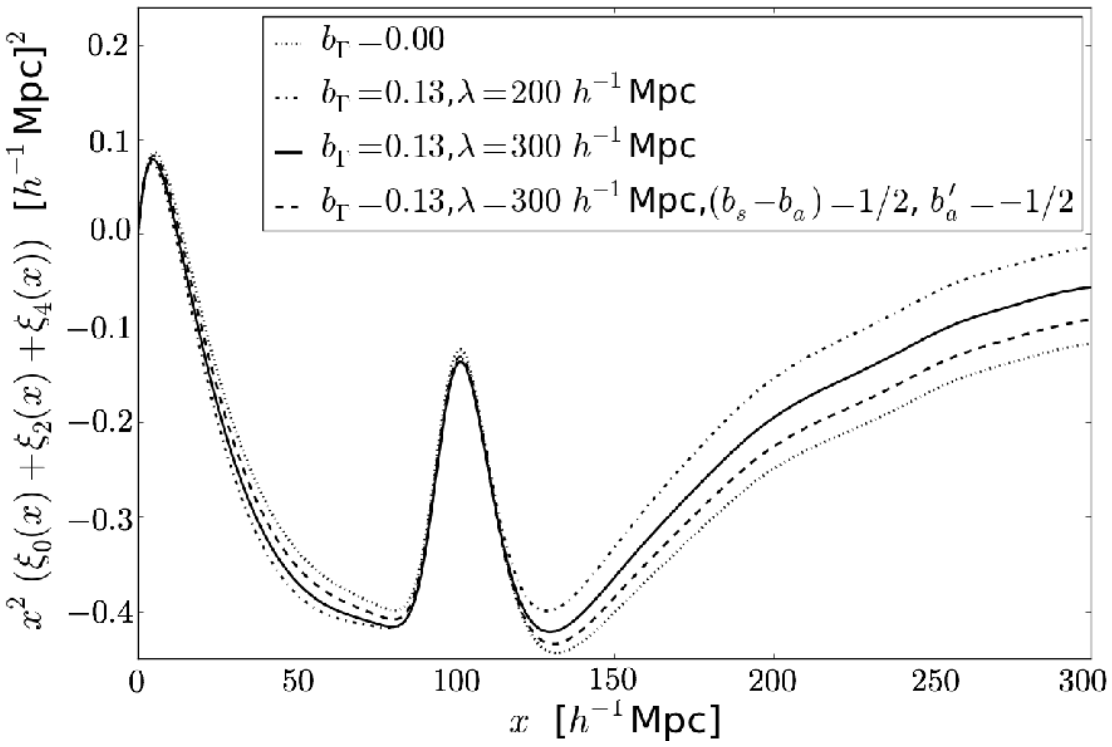

FIGURE 4.5: The sum of the monopole, quadrupole and hexadecapole of the Lyα autocorrelation function. The dotted and solid lines are as in Figures 2 and 3. The dash-dot line changes the mean free path to $200\,h^{-1}$ Mpc, and the dashed line shows the effect of changing the bias parameters from our fiducial model to the values indicated in the legend.

A simple model for the possible helium effect on the monopole of the correlation function, computed as explained in section 2.4, has been included in the dashed line in Figure 4.6. We have assumed a mean free path for the helium reionisation influence on the gas temperature of $\lambda_{0e} = \kappa_{0e}^{-1} = 30\,h^{-1}$ Mpc, and a relation between the gas temperature fluctuation and helium-ionising intensity fluctuation of $b_T = 0.1$, implying $b_e = 0.0084$ (see section 2.4). The small value that we estimate for this bias factor means that the effect from the imprint on the gas temperature that may be left from double helium reionisation is very small, even with a much smaller mean free path than for the case of hydrogen. However, the effects might be more substantial if different spectra of the ionising sources in regions of different density gave rise to a larger variation of gas temperature than our assumed value $b_T = 0.1$.

The effect of shot noise is also analysed in Figure 4.6. The dotted and solid lines are again like in Figures 4.3 and 4.4 (only the monopole is shown here), and the dashed line adds to the solid one the shot noise term from equation (4.17), multiplied by b_Γ^2, and multiplied also by a reduction factor that we now describe. If quasars are the sources of the ionising background with the luminosity function used in section 2.2, and they are isotropic and constant, the shot noise is an extremely large effect which

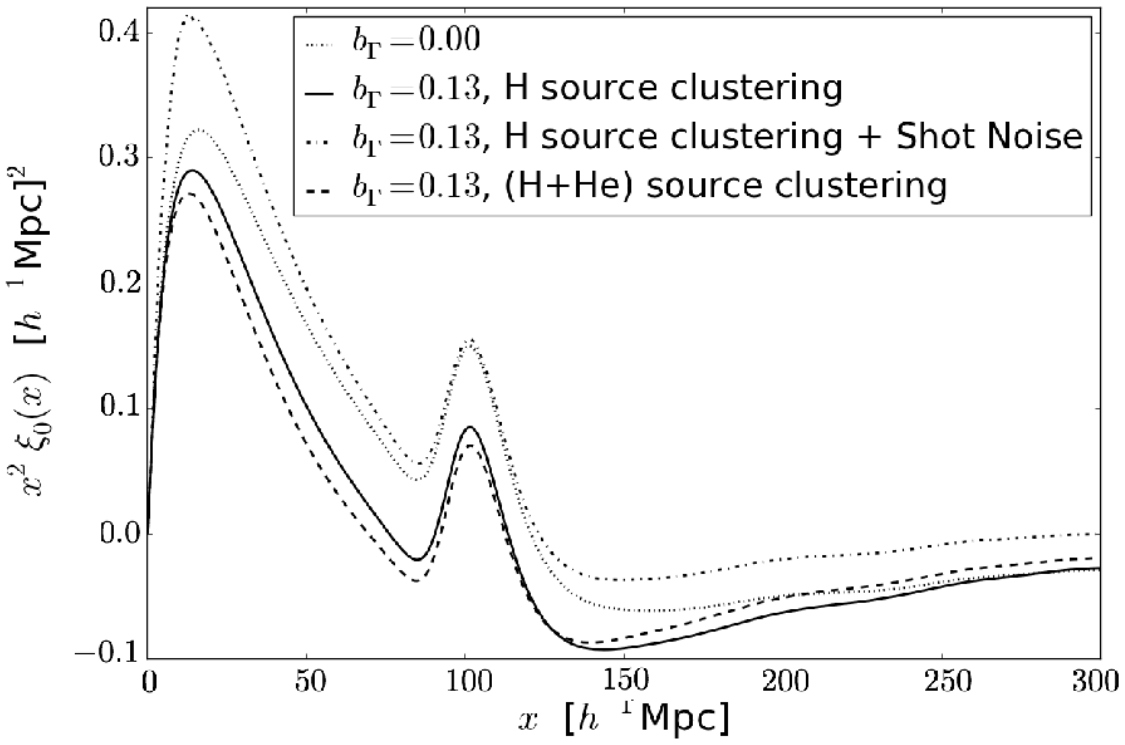

FIGURE 4.6: Monopole of the Lyα autocorrelation function. The dotted and solid lines are the same as in Figures 2 and 3. The dashed line includes the effect of helium reionisation, assuming an influence on the gas temperature with an effective mean free path $\lambda_{0e} = 30\,h^{-1}\,\mathrm{Mpc}$. The dash-dot line shows the effect of adding the shot noise from individual sources, multiplied by a reduction factor as explained in the text.

brings the value of the correlation function near the BAO peak, at $x \simeq 100\,h^{-1}\,\mathrm{Mpc}$, to $x^2\xi_0(x) \simeq 2(\,h^{-1}\,\mathrm{Mpc})^2$, well above the upper bound of the axis in Figure 4.6. However, as discussed at the end of section 2.2, the shot noise term is likely to be reduced by the contribution from galaxies to the ionising background (by the factor C/C_q in equation 4.20), the fraction of solid angle over which quasars emit their radiation, and the fraction of the time over which an individual quasar is emitting. For the purpose of visualisation, we multiply the shot noise by the overall factor

$$\frac{C}{C_q} f_\Omega f_t = \frac{1}{4} \frac{10\,h^{-1}\,\mathrm{Mpc}}{\max(x, 10\,h^{-1}\,\mathrm{Mpc})} \ . \tag{4.27}$$

The effect of variability in reducing the shot noise may reasonably be expected to scale as x^{-1}, because two points in the Lyα forest are affected by the same luminosity of a certain quasar only if they are both within the paraboloid of constant retarded time for the light emitted by the quasar that ionises the gas producing the observed Lyα absorption, and this paraboloid has a fixed width determined by the duration of the quasar luminous phase. We stress, however, that the effects of anisotropy and variability are complicated and that here we multiply the shot noise by this simple reduction factor

for display purposes.

The result in Figure 4.6 shows that the shot noise can be a large and highly significant effect. Clearly, the case of constant and isotropic quasars was already ruled out by the observations of [23], which showed that the correlation function was well fitted by the linear approximation that generalises the redshift distortion effects [33] to the Lyα forest. Even with a large reduction of the shot noise term, the effects are likely to be comparable to the source and absorber clustering term, and this will make the interpretation of any observed differences from linear theory to be complicated. One can hope, nevertheless, that by combining a detailed observation of the monopole and quadrupole terms, and using joint constraints from cross-correlations of the Lyα forest with quasars and other objects in addition to the Lyα autocorrelation, the impact of the biasing of sources and absorbers and the shot noise from a complex population of ionising sources can be disentangled in the future.

4.4 Discussion and Conclusions

The first observational determination of the large-scale Lyα power spectrum in redshift space by [23] showed a remarkably good agreement with the simple linear theory of redshift space distortions with the Cold Dark Matter power spectrum. The same conclusion was reached from measurements of the cross-correlations with damped Lyα systems and quasars [37, 38]. However, the ionising intensity fluctuations should have an impact on these correlations. We have presented an analytical framework in this paper to model these effects in the Lyα autocorrelation, which can also be easily generalised to the cross-correlation with quasars or other objects, assuming they contribute as sources of the ionising background. Our conclusion from the results obtained in a few illustrating cases is that both the clustering term that measures how sources and absorbers of the ionising background trace the mass density fluctuations, and the shot noise term that depends on the luminosity function and other properties of the sources, have an important and measurable effect on the monopole and quadrupole of the Lyα autocorrelation. A substantial broadband term is added as a contamination to this autocorrelation, which is being marginalised over in present studies that are focused on inferring the scale of the Baryon Acoustic Oscillation peak [12, 13]. As the modeling of the spectral calibration and quasar continua and the accuracy of the Lyα correlation measurements in BOSS and upcoming surveys improve in the future, we can look forward to a detection of the broadband terms induced by radiation fluctuations discussed in this paper.

There are several parameters that are important in determining how the Lyα correlation is modified by intensity fluctuations. These are the quantities appearing in equation

(4.12) for the effective Lyα bias factor, and the mean free path of ionising photons. The additional shot noise term is also dependent on many characteristics of the sources: the luminosity function, luminosity history and emission anisotropy. Disentangling all these effects from a detailed measurement and model fit to the redshift-space autocorrelations and cross-correlations will probably be a difficult challenge. However, if the emission properties and typical luminosity histories of quasars can be well understood from an accurate determination of the quasar-Lyα cross-correlation, it should be possible to model the shot-noise contribution to the autocorrelation and to infer from the observations some constraints on the biasing terms that affect the source clustering term. It is also worth noting that in the Lyα power spectrum, the term proportional to μ_k^4 is affected by neither the source clustering nor shot noise effects, and the other two terms proportional to μ_k^2 and independent of μ_k can in principle be used to separate the influence of the source clustering and shot noise effects (the term proportional to μ_k^2 is not affected by shot noise for constant and isotropic sources, but would acquire a contribution for anisotropic and variable sources). The three-dimensional Lyα power spectrum therefore provides a way of separating the radiation influences by separating the multipole terms, which are predicted to have the specific features near the scale of the mean free path shown in Figure 4.2 can then be compared to constraints obtained from cross-correlations.

The conclusions of our work are in agreement with those of [32], who has presented very similar ideas with a somewhat different mathematical treatment. There are a few differences in the way that absorbers are treated, and our incorporation of the redshift distortion effects allows us to predict the different behavior of the monopole and quadrupole terms in the Lyα power spectrum, but the basic conclusions of the two papers are similar.

While the radiation intensity fluctuations make the large-scale Lyα forest correlations substantially more difficult to interpret as a tracer of the primordial fluctuations in the universe, these complications practically do not affect the measurement of the Baryon Acoustic Oscillation scale, and they should constitute a new motivation for studying the evolution of the source and absorber population of the ionising background.

Acknowledgments

SGG thanks the APC, especially the "Cosmology & Gravitation" group, for their hospitality during part of the time when this work was being carried out. We also thank David Kirkby, Pat McDonald and Andrew Pontzen for stimulating discussions and for sharing their work on this subject. This work is supported in part by Spanish grant AYA-2012-33938.

Chapter 5

Quasar – CIV forest cross-correlation with BOSS DR12

We have made the first detection using the continuum transmission approach of a signal from the Quasar - triply ionized Carbon (CIV) forest cross-correlation. This study uses 140,813 CIV forests and 231,312 quasars from the Sloan Digital Sky Survey (SDSS) Data Release 12 (DR12). We find that the physical bias of CIV absorption systems, at redshift $z = 2.3$, is $b_{\tau c} = 2.3 \pm 0.2$, for $\beta_{Fc} = 0.52$..

5.1 Introduction

Studies of metal-absorption systems and their large-scale distribution as probed by absorption spectra can contribute to our understanding of galaxy formation and evolution. The overall star formation rate in galaxies peaked at a redshift ~ 2 to 3, and has then decreased by an order of magnitude by the present day [e.g., 50–52]. Heavy elements are produced by stars in galaxies and are subsequently expelled to the intergalactic medium (IGM) by galaxy winds. One of the most common and easily detectable lines in metal absorption systems is the triply ionized carbon (CIV) and its doublet line at 1548.204 Åand 1550.781 Å. Measuring the large-scale clustering strength of CIV systems, for example by measuring their cross-correlation with the Lyα forest or with quasars themselves, brings us closer to a full picture of the origin of these systems by informing us on the characteristic masses of the halos they reside in, because the large-scale bias factor of any population of objects in the Universe increases with the mass of their host halos (e.g., Cole & Kaiser 1989). Depending on the model assumed for the metal enrichment process, we expect different values for the clustering strength: if most CIV systems originated from stars that formed in very low-mass halos, we would expect to have a low bias factor or, in other words, to be more homogeneously distributed than dark matter; whereas if the CIV gas was expelled to the IGM in winds from massive star-forming galaxies, then the bias factor would be high, reflecting the highly biased host halos of these massive galaxies. Detailed hydrodynamic simulations of galaxy formation and the absorption line systems that are produced during the process of accretion of gas into galaxies and ejection by winds can make predictions of the properties of the absorption systems (see, e.g., Bird et al. 2016 for a recent study) that provide fundamental tests, which are as useful for improving our models of galaxy formation as the observations of galaxies themselves.

Previous studies have estimated the clustering strength of individual CIV absorbers between redshift 1.5 and 4.5 (e.g, [53], [54]). In this paper, instead of using individual CIV absorber systems, we use the observed spectrum blueward of the quasar CIV emission line as a continuous absorption field that generally probes carbon enriched gas in the Universe, similarly to the Lyα forest for atomic hydrogen, and we use this to the CIV clustering strength. Using the continuous absorption field offers the significant advantage of including all the absorption systems, whether or not they are individually detected. These type of studies have been done so far only with the Lyα forest, for which there was also a long debate about the nature of the absorption line systems and their relation to gravitationally collapsed halos on which galaxies may form (e.g., [55–58]). The approach of measuring the Lyα forest clustering in terms of the power spectrum of the continuous absorption field, starting with [16–20] has generally been very successful. In the linear

regime, the over-density of the tracer δ_t in real space relates to the over-density in mass δ through the bias factor b as $\delta_t = b \cdot \delta$; it follows that the observed Lyα forest correlation function should be equal to the mass autocorrelation times the square of the mean bias factor of the Lyα transmission fluctuation, with the appropriate modifications of the well known redshift distortions [33]. Measurements of this Lyα autocorrelation have allowed to infer the value of the Lyα bias and redshift space distortion parameters ([23], [13], [12], [59], [60], [61]). In addition to these measurements, the quasar bias and redshift space distortion parameters have been measured through the quasar-Lyα Forest cross-correlation [14, 37, 62], using the fact that the cross-correlation between two different probes is proportional to the product of the two probes bias factors. Similarly, here we measure the cross-correlation between quasars and the CIV forest at redshift 2.3 using the final data release of the Baryon Oscillation Spectroscopic Survey (BOSS) from the Sloan Digital Sky Survey IIIrd edition (SDSS-III), and measure the CIV absorption fluctuation bias at the above mentioned characteristic redshift.

We start by introducing the data samples that are used for this study in section 5.2. In section 5.3, we go in details over the procedure followed to obtain the flux variation in the CIV forest. In section 5.4 we summarize our analysis method. In section 5.5, we present our measurement of the Quasar-CIV forest cross-correlation and the inferred CIV bias factor. Finally, we discuss our results in section 5.6.

5.2 Data sets

In this paper, we are using the public twelfth Data Release (DR12, [63]) of the SDSS-III Collaboration ([21], [64], [65], [66], [67] and [68]). DR12 encompasses the entirety of the nearly 5 years of observations of the Baryon Oscillation Spectroscopic Survey (BOSS, [22]).

5.2.1 Quasar catalog

The DR12 quasar catalog[1], described in [69], contains 297,301 quasars. which were targeted for spectroscopy using the target selection procedure presented in [70], that makes use of a number of algorithms to identify candidates such as the ones described in [71], [72], [73] and [74]. We impose a redshift cut such that $z_q \in [1.4, 4.2]$ which reduces the catalog to 231,312 quasars. We use the quasar redshifts obtained with the Principal Component Analysis method, as described in [75], [76] and [69]. The redshift distribution of the quasar catalog is illustrated on Figure 5.1.

[1] http://data.sdss3.org/dr12/.../boss-dr12-quasar-catalog/

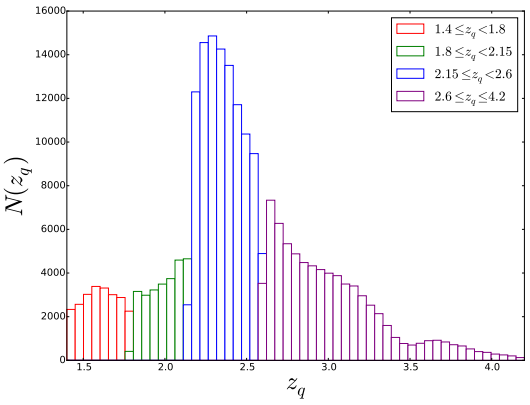

FIGURE 5.1: Distribution of the redshift of the quasars with $z_q \in [1.4, 4.2]$.

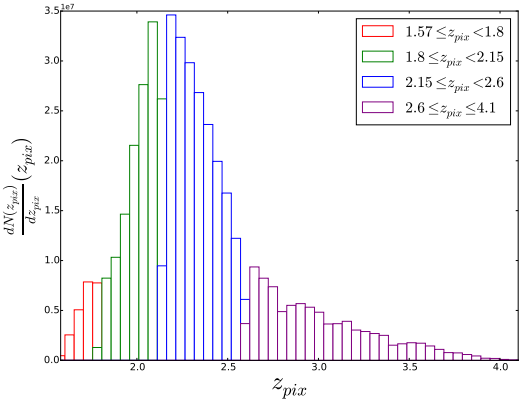

FIGURE 5.2: Weighted distribution of the redshift of the CIV forest pixels with $z_{pix} \in [1.57, 4.10]$.

5.2.2 CIV sightline sample

The first cut we apply on the final BOSS data release is with regards to broad absorption lines (BALs). When significant amounts of matter are expelled along quasar jets pointing to our direction at velocities of many thousands of km·s^{-1}, BALs are produced in its spectrum at wavelengths blueward of the Lyα and other emission lines. The broadness of these lines, caused by the large velocity dispersion of the outflowing gas, is used to identify them and classify the quasars according to the balnicity index (BI), introduced in [77]. The visual inspection of DR12 confirmed 297,301 quasars, of which 267,721 were visually flagged for BAL. We also exclude any quasars with a BI greater than zero. That leaves us with 266,456 quasars.

We then set a quasar redshift cut such that $z_q \in [1.8; 4.2]$, leaving 182,566 quasars. The lower limit is set by the requirement that the observed wavelength be greater than 3600 Å, the minimum observable wavelength for the BOSS spectrograph. The upper limit is set by the maximum quasar redshift of 4.2, beyond which the BOSS surface density of quasars is not sufficient to be useful for this study. We define the CIV forest to be between 1420 Å and 1520 Å in the quasar rest-frame. The quasar redshift cut we have applied only leaves spectra with a fully observed CIV forest and spectral pixels in the CIV forest with redshift $z_{pix} \in [1.57, 4.10]$.

We remove the pixels where the variance of the co-added sky-subtracted sky fibers is significantly higher than from the surrounding sky continuum. The DR12 sky mask provides a list of such observed-frame wavelengths (contact Michael Blomqvist for the full file). To apply the mask, we remove any pixels whose observed wavelength satisfies

$$abs(10^4 \cdot \log_{10}(\lambda/\lambda_{mask})) <= m \tag{5.1}$$

for some λ_{mask} in the list, where m is the margin. We use a margin of 1.5 that suitable for both co-added and individual exposures. Note that pixels in the BOSS co-added spectra have wavelength width $\Delta \log_{10} \lambda = 10^{-4}$.

The spectrum in the CIV forest region needs to be appropriately normalized by defining a quasar continuum. We define for this purpose two zones surrounding the CIV forest that avoid the SiIII, SiIV and CIII emission lines : zone_1 = [1280 Å ; 1380 Å] and zone_2 = [1575 Å ; 1860 Å]. A spectrum is retained to contribute in our sample if the following condition for the signal-over-noise is satisfied:

$\sum_{\lambda_{RF}} \left(f(\lambda_{RF}) / \sqrt{\text{var}(\lambda_{RF})} \right) \geq 2$ where f is the observed flux and $\lambda_{RF} \in \text{zone}_1$ – *AND* – zone_2. As a result, the sample we analyze contains a total of 140,813 line of sights, and a redshift distribution of the pixels such as described in Figure 5.2.

5.2.3 Sub-samples

For economy of computing time, we divide the CIV sightline sample described in 5.2.2 into 2,370 sub-samples, corresponding to the 2,370 observational plates that make the final data release of SDSS- III BOSS, see Figure 5.3 and combine their measurements.These are the same sub-samples $\mathcal{P}$ that will be used to estimate the covariance matrix associated to the quasar - CIV forest measurement described in section 5.4.1.

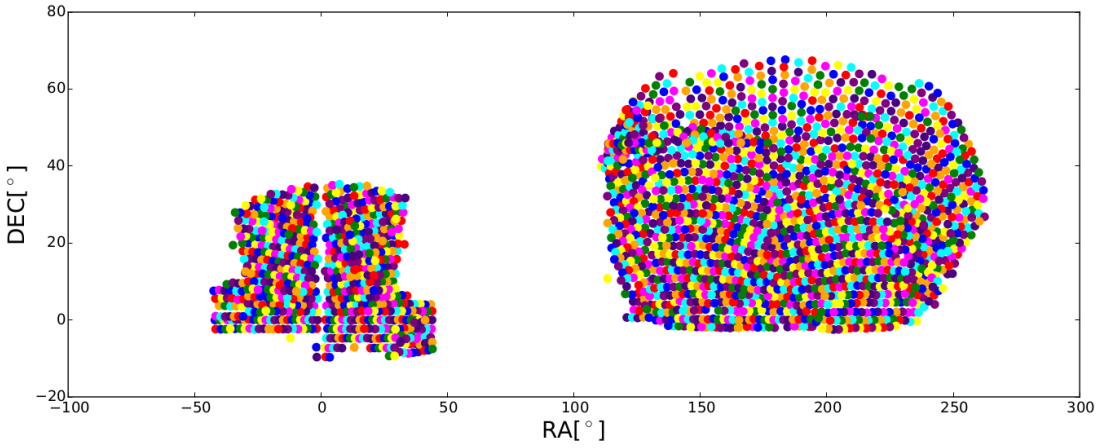

FIGURE 5.3: DR12 footprint in J2000 equatorial coordinates with the 2,370 sub-samples indicated in different colors – left area is the South Galactic Cap and right area is the North Galactic Cap. The size of dot-like representation is arbitrary and simply indicates the center of the plate, not its actual size.

In section 5.5, we will partition the work sample we defined in 5.2.2 into 4 according to the redshift range of the observed quasars. Table 5.1 presents the redshift intervals used to define the partitions.

	$z-$range	$\langle z \rangle$	
$\mathbb{F}$	1.4 - 4.2	2.2981	100 %
v$\mathbb{L}$	1.4 - 1.8	1.7225	4 %
$\mathbb{L}$	1.8 - 2.15	2.0325	20 %
$\mathbb{M}$	2.15 - 2.6	2.327	63%
$\mathbb{H}$	2.6 - 4.2	2.8519	13%

TABLE 5.1: Redshift intervals used in this analysis, their corresponding mean redshift and proportion of the work sample defined in 5.2.2.

5.3 From BOSS DR12 spectra to δ_{CIV}

In order to extract the flux variation in the CIV forest, δ_{CIV}, one needs to divide the observed flux by an estimation of the intrinsic quasar continuum in that region. This is done by co-adding the normalized spectra of our work-sample. We start by describing the renormalization steps, then we present the continuum estimate resulting from the stacking. Finally, we define the flux variation in the CIV forest.

5.3.1 Continuum fitting

For a given forest $\mathcal{F}$ in our work-sample, we start by normalizing by a coefficient $c_{\mathcal{F}}$ such that:

$$c_{\mathcal{F}} = \sum_{\mathcal{F},i} w_{\mathcal{F},i} f_{\mathcal{F},i} / \sum_{i} w_{\mathcal{F},i} \tag{5.2}$$

where a pixel i of the forest $\mathcal{F}$ belongs either to zone$_1$ or to zone$_2$ and where $f_{\mathcal{F},i}$ and $w_{\mathcal{F},i}$ are the flux and weight for said pixel i. Here, $w_{\mathcal{F},i}$ is the pipeline estimate of the inverse noise variance available in the BOSS SPEC files. Then, we correct for the tilt, the difference of intensity between the red-end and the blue-end of the quasar through the coefficients $A_{\mathcal{F}}$ and $B_{\mathcal{F}}$. These parameters being respectively the offset and the slope calculated from zone$_1$ and zone$_2$. The normalized flux $\hat{f}_{\mathcal{F}}$ and its associated weight $W^{cont}_{\mathcal{F},i}$ are as follow:

$$\hat{f}_{\mathcal{F},i} = \frac{f_{\mathcal{F},i}}{c_{\mathcal{F}}(A_{\mathcal{F}} + B_{\mathcal{F}}\lambda_i)} \tag{5.3}$$

$$W^{cont}_{\mathcal{F},i} = (c_{\mathcal{F}}(A_{\mathcal{F}} + B_{\mathcal{F}}\lambda_i))^2 \cdot w_{\mathcal{F},i} \tag{5.4}$$

Finally, renormalized spectra from the sample described in 5.2.2 (i.e. $R[f_{\mathcal{F},i}]$) are stacked in the quasar rest-frame using the weights $W^{cont}_{\mathcal{F},i}$ presented in equation 5.4 to produce the mean quasar continuum, see equation 5.5.

$$C(\lambda_{RF}) = \sum_{\mathcal{F}} \left(W^{cont}_{\mathcal{F}}(\lambda_i) \cdot \hat{f}_{\mathcal{F}}(\lambda_i) \right) / \sum_{\mathcal{F}} W^{cont}_{\mathcal{F}}(\lambda_i) \tag{5.5}$$

It is interesting for the reader to take note that as a result of equation 5.5 our work-sample has the following property in the restframe: $\left\langle \hat{f}_{\mathcal{F},i}/C(\lambda_i) \right\rangle = \vec{1}$.

Figure 5.4 illustrates for one arbitrary spectrum the normalizing steps previously described, as well as illustrates the resulting continuum estimate for our work-sample.

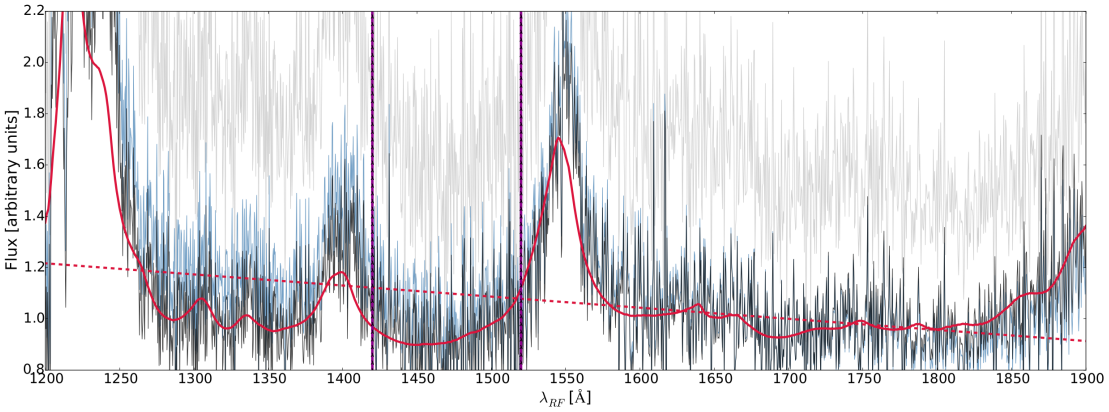

FIGURE 5.4: Illustration of some of the steps used to estimate the mean quasar continuum, and incidentally the flux variation in the CIV forest for BOSS spectrum at $z = 2.896$, $RA = 1.490°$, $DEC = 13.582°$, reference PLATE = 6177, MJD = 56268, FIBER = 55 and THINGID=232251732. The gray spectrum is the observed spectrum $f_{\mathcal{F}}$. The blue spectrum, is the gray spectrum renormalized by the coefficient introduced in equation 5.2: $f_{\mathcal{F}}/c_{\mathcal{F}}$. The red dashed line illustrates the tilt $A_{\mathcal{F}} + B_{\mathcal{F}}\lambda_i$. The black spectrum $\hat{f}_{\mathcal{F},i}$ is the renormalized spectrum corrected for the difference of intensity between the red-end and the blue-end of the quasar, as described in equation 5.3. The red solid line is the mean quasar continuum introduced in equation 5.5. Finally, the purple vertical lines delimit the CIV forest,

5.3.2 Determination of the flux variation in the CIV Forest

In order to create the flux variation in the CIV forest, we use the sightline sample defined in 5.2.2. The definitions given in equation 5.3 and in equation 5.4 are still valid. The flux variation in the CIV region is therefore:

$$\delta_{\mathcal{F},i}^{CIV} = \frac{\hat{f}_{\mathcal{F},i}}{C(\lambda_{RF})s(\lambda_{obs})} - 1 \tag{5.6}$$

where $s(\lambda_{obs})$ corrects for systematic errors in the calibration vectors in the spectra, (refer to similar correction in [61]) . It is obtained by co-adding all of the flux variation elements of our work sample in the observed frame and it ensures that $\langle \delta^{CIV} \rangle = 0$ at each wavelength:

$$s(\lambda_{obs}) = \sum_{\mathcal{F}} \left(W_{\mathcal{F},i}^{CIV} \frac{\hat{f}_{\mathcal{F},i}}{C(\lambda_{RF})} \right) / \sum_{\mathcal{F}} W_{\mathcal{F},i}^{CIV}. \tag{5.7}$$

where

$$W_{\mathcal{F},i}^{CIV} = \left[\left(C^2(\lambda_i) \cdot W_{\mathcal{F},i}^{cont} \right)^{-1} + \sigma_{int}^2 \right]^{-1}. \tag{5.8}$$

Then we renormalize said elements by the total sum so that in observed frame :

$$\sum_{\mathcal{F}} W_{\mathcal{F},i}^{CIV} \delta_{\mathcal{F},i}^{CIV} = \vec{0}. \tag{5.9}$$

In order to account properly for the contribution of strong absorbers relatively to all absorbers, we introduce the notion of intrinsic deviation, noted σ_{int}. From [78], we assume $1 - \bar{F}_{CIV} = 0.006$, we expect the intrinsic deviation to be $\sigma_{int} = \sqrt{0.006} = 0.08$.

5.4 Quasars-CIV Forest cross-correlation

Let $\xi_{\mathcal{P}}$ be the measured cross-correlation between quasars and CIV forests in a given plate. The pairs quasar-pixel that contribute to a $\xi_{\mathcal{P},A}$ element satisfy (a) the pixel i belongs to a forest $\mathcal{F}$ located in plate $\mathcal{P}$ see(5.2.3) and (b) the distance between said pixel i and the quasar from the DR12Q quasar catalog (see 5.2.1) falls in a bin A. Note that we measure the cross-correlation up to scales of 64 h^{-1} Mpc, and the size of a bin is 4 h^{-1} Mpc along the line of sight and 4 h^{-1} Mpc across the line of sight. Let $W_{\mathcal{P},A}$

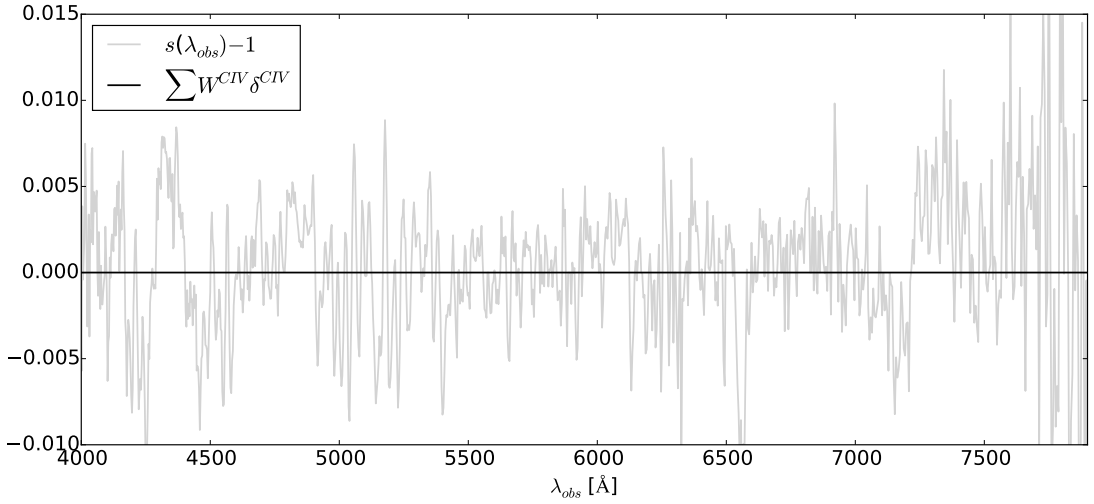

FIGURE 5.5: Illustration of the co-addition of all the forests in our work sample before and after correcting for systematic errors in the calibration vectors in the spectra. The black line corresponds to equation 5.9 and the gray line to equation 5.7.

be the sum of the weights associated to a bin A. These quantities are expressed in the following manner:

$$\xi_{\mathcal{P},A} = \left(\sum_{\mathcal{F}\in\mathcal{P}, i\in A} W^{CIV}_{\mathcal{F},i}\, \delta^{CIV}_{\mathcal{F},i} \right) / W_{\mathcal{P},A} \qquad \text{where} \qquad W_{\mathcal{P},A} = \sum_{\mathcal{F}\in\mathcal{P}, i\in A} W^{CIV}_{\mathcal{F},i} \tag{5.10}$$

The cross-correlation between the full DR12 δ_{CIV} sample described in 5.3.2 and the quasar sample described in 5.2.1 is

$$\xi_A = \sum_{\mathcal{P}} W_{\mathcal{P},A}\xi_{\mathcal{P},A}/W_A \qquad \text{and} \qquad W_A = \sum_{\mathcal{P}} W_{\mathcal{P},A} \tag{5.11}$$

5.4.1 The covariance matrix under revision!

For bins A and B, any element of the covariance matrix C, for the cross-correlation ξ, can be expressed as follow:

$$C_{AB} = \langle \xi_A \xi_B \rangle - \langle \xi_A \rangle \langle \xi_B \rangle \tag{5.12}$$

Using the sub-samples described in 5.2.3 and neglecting the small correlations between sub-samples, the covariance can be expressed as:

$$C_{AB} = \frac{1}{W_A W_B} \sum_{\mathcal{P}} W_{\mathcal{P},A} W_{\mathcal{P},B} \left[\xi_{\mathcal{P},A}\xi_{\mathcal{P},B} - \xi_A \xi_B\right] \tag{5.13}$$

For the covariance matrix to be reliable, there is need for its number of elements $\mathcal{N}(C_{AB})$ to be considerably smaller than the number of sub-samples $N_p = 2370$. As stated previously, in this analysis we measure the cross-correlation in bins of 4 $h^{-1}\,\mathrm{Mpc}$, with $r_\parallel \in [-64, 64]$ $h^{-1}\,\mathrm{Mpc}$ and $r_\perp \in [0, 64]$ $h^{-1}\,\mathrm{Mpc}$. The covariance matrix has $\mathcal{N}(C_{AB})(16 \times 32)^2$ elements, and the condition $N_p \gg \mathcal{N}(C_{AB})$ is not respected. To correct for this, we apply a method that allows to reduce the effective number of $\mathcal{N}(C_{AB})$ elements by averaging over elements of the correlation matrix. The correlation matrix associated to a given covariance matrix is defined as:

$$\varrho_{AB} = \frac{C_{AB}}{\sqrt{C_{AA}C_{BB}}} \tag{5.14}$$

We consider that bins A and B will be correlated only if they have the same transverse separation $r_{\perp,A} = r_{\perp,B}$, see [12]. For a given transverse separation, exception made for very small $r_\perp$, the cross-correlation coefficients between bins A and B are almost independent of their line of sight separation. The cross-correlation coefficients between bins A and B depend on their transverse separation. These two statements are illustrated on figure 5.6.

We define ρ the *smoothed* correlation matrix associated to ϱ. At a given transverse separation $\bar{r}_\perp$, $\rho(\Delta r_\parallel\,;\,\bar{r}_\perp) = \langle\varrho(\Delta r_\parallel\,;\,\bar{r}_\perp)\rangle$. On figure 5.6, the correspondence to this function of $\Delta r_\parallel$ at a fixed $\bar{r}_\perp$ is a set of same-color dots. For example, *set 0* corresponds to the function $\rho(\Delta r_\parallel\,;\,\bar{r}_\perp)$ where $\bar{r}_\perp = 2$ because $0 \leq r_\perp < 4$. For all the sets, and their corresponding $\bar{r}_\perp$, the first dot on the left side is $\rho(r_\parallel\,;\,\bar{r}_\perp) = \langle\varrho_{AB}(\Delta r_\parallel\,;\,\bar{r}_\perp)\rangle$ where $\Delta r_\parallel = 4$.

The rest of the analysis uses the *smoothed* covariance matrix $\tilde{C}_{AB} = \rho_{AB} \cdot \sqrt{C_{AA}}\sqrt{C_{BB}}$ that results from applying this method.

5.4.2 Fitting the CIV bias

The CIV forest probes material at low density and high redshift, which is affected by non-linear evolution and random peculiar velocities in such faint ways that we remain, in the limit of large scales, within linear theory. Linear theory predicts the form of the

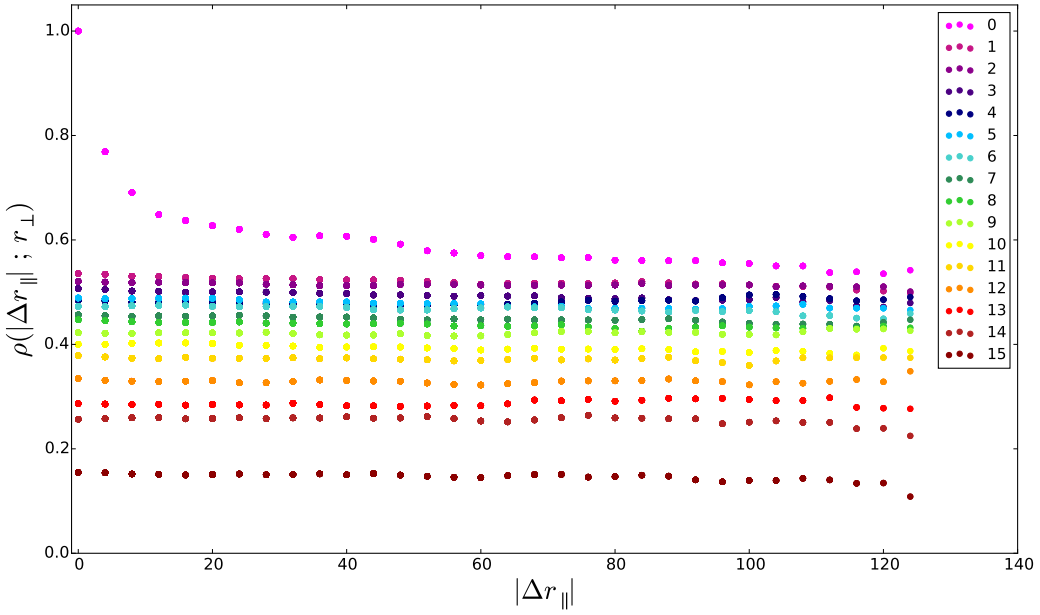

FIGURE 5.6: *Smoothed* correlation matrix associated to ϱ as a function of line of sight separation at fixed transverse separation. The legend refers to the 16 bins in $r_\perp$, of width 4 h^{-1} Mpc, where *set 0* indicates $0 \leq r_\perp < 4$ and *set 15* indicates $60 \leq r_\perp < 64$. A set of same-color dots corresponds to $\rho(\Delta r_\parallel\ ;\ \bar{r}_\perp) = \langle \varrho(\Delta r_\parallel\ ;\ \bar{r}_\perp) \rangle$ at a given transverse separation.

correlations among any pair of tracers of the large scale structure in redshift space, see [33]. The linear Quasars-CIV cross-power spectrum, a.k.a the Fourier transform of the measured Quasars-CIV cross-correlation function, is expressed as follow:

$$P_{QCIV}(\mathbf{k}, z) = b_{Fc}(z)[1 + \beta_{Fc}(z)\mu_k^2] \cdot b_q(z)[1 + \beta_q(z)\mu_k^2]P_L(k, z) \tag{5.15}$$

where b_{Fc} and b_q are the CIV and quasars density bias factors respectively, β_{Fc} and β_q are their redshift space distortion parameters and $P_L(k, z)$ is the linear matter power spectrum. As expressed in equation (5.15), the amplitude of each Fourier mode in a biased tracer field is enhanced by the redshift distortions by the factor $b_{Fc}(z)[1 + \beta_{Fc}(z)\mu_k^2]$, where β is the redshift distortion parameter associated to CIV systems and μ_k the cosine of the angle between the Fourier mode and the line of sight.

We make use of the fitting tool BAOFIT[2] developed by the BOSS collaboration to constrain cosmological and astrophysical parameters from correlations between quasar-type tracers of the underlying mass density field. We work with the PLANCK 2015 cosmology [4]. We assume that there is no redshift evolution for the CIV bias and that the quasar bias follows the evolution described in [62]:

[2] http://darkmatter.ps.uci.edu/wiki/DeepZot/Baofit

$$b_q(z) = \frac{e_{q,1} + e_{QSO,2} \cdot (1+z)^2}{e_{q,1} + e_{q,2} \cdot (1+z_{ref})^2} \cdot b_q(z_{ref}) \tag{5.16}$$

where $e_{q,1} = 0.53$ and $e_{q,2} = 0.289$, and where a recent reference value can be borrowed from [79] such that $b_q(z_{ref}) = 3.91$ for $z_{ref} = 2.39$. For computational purposes, we use a power law with $\gamma_q = 1.7133$ that fits the redshift evolution described in equation 5.16. We fit from 5 h^{-1} Mpc up to scale 60 h^{-1} Mpc.

5.5 Results

In this section the results of the cross-correlation of quasars and the CIV absorption in redshift space are presented. After obtaining a series of fit around our fiducial model, we check the consistency of our results using the smoothed covariance matrix by comparing to estimations made using bootstrap errors.

5.5.1 CIV bias parameter

We make several measurements of the quasar CIV forest cross-correlation in different redshift intervals, defined in table 5.1. The parameters we are interested in measuring are the CIV bias b_{Fc}, the CIV redshift distortion parameter β_{Fc}, the velocity shift Δ_v and the dispersion in quasar redshift $z-$disp. We start by doing a 4-parameters fit for the full redshift interval $\mathbb{F}$, presented in the first line of table 5.2. Since β_{Fc} is barely constrained by such a fit, we add a gaussian prior that limits its variation in the interval [0.3,0.6], see second line of table 5.2. Then we fix β_{Fc}, Δ_v and $z-$disp to the values measured in the 1-parameter fits for the $\mathbb{F}$ sample and proceed to measure the CIV bias in the different redshift sub-samples. Those results are presented in the lower part of table 5.2.

	$(1+\beta_{Fc})b_{Fc}$	β_{Fc}	Δ_v $[km \cdot s^{-1}]$	$z-$disp [Mpc$\cdot h^{-1}$]	χ^2	dof
$\mathbb{F}$	-0.024 ± 0.003	1.09 ± 0.56	-128.1 ± 56.1	4.75 ± 0.83	351	$356-4$
$\mathbb{F}$	-0.021 ± 0.0018	0.52 ± 0.14	-127.0 ± 54.4	4.18 ± 0.73	352	$356-4$
v$\mathbb{L}$	-0.0211 ± 0.0057	0.52	-127.0	4.18	372	$356-1$
$\mathbb{L}$	-0.0193 ± 0.0034	0.52	-127.0	4.18	346	$356-1$
$\mathbb{M}$	-0.0205 ± 0.0018	0.52	-127.0	4.18	365	$356-1$
$\mathbb{H}$	-0.0208 ± 0.0048	0.52	-127.0	4.18	343	$356-1$

TABLE 5.2: Estimation of $(1+\beta_c)b_{Fc}$, β_c, $\Delta_v$and $z-$disp for different fitting configurations. We divided our full CIV sightlines sample $\mathbb{F}$ ($z \in [1.4, 4.2]$) into 4 subsamples by condition of redshift: v$\mathbb{L}$ corresponds to $z \in [1.4, 1.8]$, $\mathbb{L}$ to $z \in [1.8, 2.15]$, $\mathbb{M}$ to $z \in [2.15, 2.6]$ and $\mathbb{H}$ to $z \in [2.6, 4.2]$.

Redshift evolution of the CIV bias

When comparing our fitting results of our measurements of the CIV transmission bias at 4 different redshift intervals (vL,L,M,H), we see no significant sign of redshift evolution. We conclude that our measurement is consistent with CIV bias having no redshift evolution between redshifts 1.7 and 2.9..

5.5.2 Bootstrap evaluation of the error

In order to verify the robustness of the smoothing of the covariance matrix, we estimate the error on the fitted value of the CIV bias by bootstrap from the 2,370 plate measurements. We create a composite correlation ξ_{2370} from picking at random 2,370 $\xi_{\mathcal{P}}$ correlations and adding them accounting for their weights. Then the CIV bias is fitted for ξ_{2370} with the covariance matrix expressed in equation 5.12. We do this operation two hundred and fifty times and obtain a set of 250 $B = \{b_{Fc}\}$ values. The estimation of the CIV bias for a given redshift interval of the CIV sightline work sample is the mean value of B, with its associated error being the variance of the set of B values. The value of the CIV bias and its error estimated with the bootstrap method, matches the one obtained using only the smoothed covariance matrix. We are satisfied by the robustness of method we presented in 5.4.1 to "smooth" the covariance matrix.

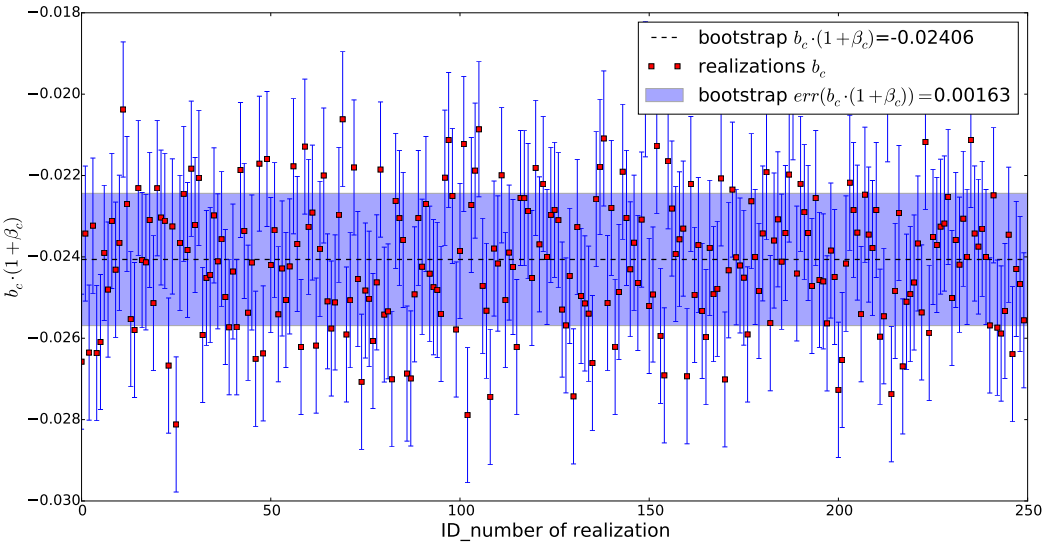

FIGURE 5.7: Set of 250 $B = \{b_{Fc}\}$ values obtained by bootstrap from the set of 2,370 $\xi_{\mathcal{P}}$ quasar CIV forest cross-correlations. This bootstrap measurement should be compared with the first line of table 5.2.

5.6 Discussion

This paper has focused on deriving the transmission bias factor of the CIV absorption from the measurement of the cross-correlation of this absorption with quasars. However, a theoretical interpretation of this measurement requires a relation between this transmission bias factor to the physical bias factor of CIV absorbers, which is related at the same time to the bias factor of their host halos.

We assume that this relation between transmission and physical bias factors is the general one derived in [39] for any class of absorption systems where the absorption profiles rarely overlap and the internal absorption profiles are not correlated with the large-scale structure (see their section 4.3). A simple way to understand the relation is to start with the definition of the transmission fluctuation of CIV absorbers δ_{Fc} (or δ^{CIV} in section 5.3), $F_c = \bar{F}_c(1+\delta_{Fc})$, where F_c is the flux transmission fraction due to CIV absorbers only, and $\bar{F}_c$ is its average value. Defining the effective optical depth as $F_c = e^{-\tau_c}$ when averaged over a large-scale region, our assumption is that the effective optical depth is the quantity that changes linearly with the density of absorbers in redshift space, and therefore the transmission fluctuation δ_{Fc} corresponds to an absorber density fluctuation $\delta_{\tau c}$ that is derived as:

$$\bar{F}_c(1+\delta_{Fc}) = e^{-\tau_c} = e^{-\bar{\tau}_c(1+\delta_{\tau c})} = \bar{F}_c(1-\bar{\tau}_c\delta_{\tau c}) \; ; \qquad \delta_{\tau c} = \frac{\delta_{\tau c}}{\log \bar{F}_c} \; . \tag{5.17}$$

The transmission and physical bias factors and redshift distortion factors are therefore related as

$$b_{\tau c} = -\frac{b_{Fc}}{\log \bar{F}_c} \; ; \qquad \beta_{\tau c} = \beta_{Fc} \; . \tag{5.18}$$

These physical bias factors should be equal to the bias factors of their host halos derived from any cosmological theory, and the physical redshift distortion factor should be given by the standard equation $\beta_{\tau c} = f(\Omega)/b_{\tau c}$, where $f(\Omega)$ is the logarithmic derivative of the growth factor.

Our measurement of β_{Fc} therefore is directly related to the physical bias factor of the absorbers, but its measurement error is very large. To obtain a more reliable estimate of the physical bias factor from our measurement of $b_{Fc}(1+\beta_{Fc})$, we need an estimate of $\bar{F}_c$.

5.6.1 The mean transmission of the CIV forest

For a population of uncorrelated absorbers, the mean transmission is related to the density of absorbers per unit redshift and equivalent width W_c, $\mathcal{N}(W_c, z)\, dW_c$. For the

CIV doublet, the standard convention used in the literature is that the equivalent width W_c is that of the strongest line at $\lambda = 1548.2$ Å. The mean effective optical depth due to the CIV forest is then

$$\bar{\tau}_c(z) = -\log(\bar{F}_c(z)) = \int_0^\infty dW_c \frac{\mathcal{N}(W_c, z)\, W_c(1+\bar{q}_c)(1+z)}{\lambda_c} \ , \tag{5.19}$$

where $\lambda_c = 1549.1$ Åis the mean rest-frame wavelength of the CIV doublet, and $\bar{q}_c$ is the average doublet equivalent width ratio of the absorbers (weighted by W_c).

To estimate $\bar{\tau}_c$, we use the observed equivalent width distributions obtained by [80] and [78]. The results of [78] are more reliable at high equivalent width because they are based on a very large sample of quasars (SDSS DR7), whereas [80] use a smaller sample of quasar spectra with high resolution and signal-to-noise, allowing them to measure the distribution of weak absorption systems. We use an exponential distribution, which fits well the observations of [78] :

$$\mathcal{N}(W_c, z) = k \exp(-W_c/W_*) \ . \tag{5.20}$$

We take the fitted values for k and W_* from Table 4 of [78], for their redshift range $2.24 < z < 2.51$, which best corresponds to our middle redshift range, $2.15 < z < 2.6$, which contains most of our absorption systems. The values are $W_* = 0.368$ Å, and $kW_* = 4.84$ (we have converted the value of k reported by [78] to a density of systems per unit redshift, which is the directly observed quantity, instead of density per unit X, where $dX = dz(1+z)^2 H_0/H(z)$, a quantity often used in studies of absorption systems). The distribution of CIV equivalent widths has been found to be weakly evolving over the redshift range covered by the SDSS data, so we ignore any possible effects of redshift evolution and we use our results for the full sample (see their Table 4).

Integrating equation (5.19) with the exponential form of the equivalent width distribution, we find

$$\bar{\tau}_c = \frac{(1+\bar{q})(1+z)kW_*^2}{\lambda_c} \ . \tag{5.21}$$

We use a mean doublet ratio $\bar{q} = 0.695 \pm 0.010$ from the mean value measured in [81] for CIV systems associated with DLAs, noting that the mean equivalent width of DLAs found in [81]l is $\bar{W}_c = 0.429$ Å, only slightly larger than W_*, implying a similar degree of line saturation and therefore of the value of $\bar{q}$. At a mean redshift $z = 2.37$, this yields a value $\bar{\tau}_c = 0.00657$.

We now correct this value for the fact that the true equivalent width distribution does not follow the exponential form at $W < 0.5$ Å, where the SDSS data used in

[78] starts being incomplete. [80] find that the CIV equivalent width distribution is correctly modeled by a power-law at low equivalent widths. We use their power-law model $\mathcal{N}(W_c, z) \propto W_c^{-\alpha}$, with $\alpha = 1.53$, which provides a good fit down the lowest equivalent widths at which they are complete (see their Figure 2). We assume we can treat the systems as optically thin for the low column densities at which we use their model, so that CIV column densities are proportional to equivalent widths. We match the power-law and equivalent width distributions at $W = 1.4W_* = 0.515$ Å, which is roughly where the results of [80] and [78] match (see Figure 10 in [78]), and also the equivalent width below which the data of [78] starts being incomplete. Assuming a fixed value $1 + \bar{q} = 1.695$, we replace the function $\mathcal{N}$ by

$$\mathcal{N}_{\rm corr} = k \, \exp(-W_c/W_*) \; , \qquad (W > 1.4W_*) \; ; \tag{5.22}$$

$$\mathcal{N}_{\rm corr} = k \, \exp(-1.4) \left(\frac{W_c}{1.4W_*} \right)^{-1.53} \; , \qquad (W < 1.4W_*) \; . \tag{5.23}$$

The corrected value with this distribution is found to be $\bar{\tau}_c = 0.0106$. Finally, we note that the correction to this effective optical depth arising from the difference between the exponential distribution and the power-law distribution at $W < 1.4W_*$, which is $\Delta\bar{\tau}_c = 0.0040$, probably has an average value of $1 + \bar{q}$ that is intermediate between the value $1 + \bar{q} = 1.695$ for DLAs found by [81] , and the limiting value for optically thin absorbers, $1 + \bar{q} = 1.5$. Adopting an intermediate value $1 + \bar{q} = 1.6$ for this correction to the W_c distribution, we reduce the correction to $\Delta\bar{\tau}_c = 0.0040 \cdot (1.6/1.695)$, and we obtain our final estimate $\bar{\tau}_c = 0.0103$.

The error on our estimate of $\bar{\tau}_c$ is dominated by the uncertainties in the W_c distribution and its redshift evolution, in particular by the slope of the power-law distribution and how far down it extends to low W_c. An error ± 0.1 to the power-law slope in α implies an error of $\sim 10\%$ in $\bar{\tau}_c$. We note also that the low-W_c absorbers tend to be clustered with the high W_c ones because they often result from de-blending of complex absorption profiles, which may have led us to an overestimate of $\bar{\tau}_c$, but this is difficult to estimate. We therefore urge the total absorption by all detected absorbers to be directly reported in future studies of weak metal-line systems.

5.6.2 The physical bias of the CIV absorption systems

Having estimated $\bar{\tau}_c$, we can now obtain our estimate for the average physical bias of the CIV absorbers. Using our estimate from section 5.1, we find the result:

$$b_{\tau c}(1 + \beta) = b_{Fc} \frac{(1 + \beta)}{\bar{\tau}_c} \simeq 2.3 \; . \tag{5.24}$$

Using also $\beta = f(\Omega)/b_{\tau c} \simeq 0.98/b_{\tau c}$ at our mean redshift $z = 2.37$, we find a consistent answer for $b_{\tau c} \simeq 1.2$, and $\beta \simeq 0.8$. Our result therefore yields a value for the physical bias factor of the CIV absorbers that is rather low, suggesting that CIV absorbers may occupy lower mass halos than DLAs, for which the physical bias is close to 2 (see [38]). However, the systematic error due to $\bar{\tau}_c$ is still substantial. For a reasonably lower value of $\bar{\tau}_c = 0.009$, and $b_{Fc}(1+\beta) = -0.027$, we would obtain $b_{\tau c} \simeq 2$. Our error on $b_{\tau c}$ is therefore large and of a systematic nature, arising from the uncertainty in determining $\bar{\tau}_c$, and more precise observations will be necessary to determine its value with greater confidence.

5.6.3 Relation to the host halo physical bias factor

The bias of metal lines can be modeled theoretically assuming that the gas causing metal absorption is associated with host halos with some mass distribution. This is probably a very good approximation because metals are rare outside halos (they can only move to the intergalactic medium due to strong winds) and because the metals are highly ionized in regions of very low density and they are unlikely to produce absorption systems that can contribute significantly to the mean absorption. Any large-scale structure model predicts a number density of halos $n(M)\,dM$ of mass M in a bin dM. If a line of sight intercepts this halo, a metal line can be observed with some equivalent width W_c. A useful concept to define is the *absorptionvolume* of the metal line produced by a halo, equal to

$$V_c(M) = \int d^2x \frac{W_c(1+\bar{q}_c)(1+z)}{\lambda_c} \frac{c}{H(z)} \ , \tag{5.25}$$

where the integral is done over the projected area of the halo seen from a specific line of sight, with comoving coordinates x in the perpendicular directions. The volume V_c is then obtained in comoving units, and is defined to be an average over all halos of mass M. The mean absorption of CIV systems is then given by

$$\bar{\tau}_c = \int dM\, n(M)\, V_c(M) \ . \tag{5.26}$$

The large-scale structure models predict the bias of halos of mass M, and the bias factors of CIV systems are related to this by

$$b_{Fc} = -\int dM n(M)\, b(M)\, V_c(M) \ ; \qquad b_{\tau c} = -\frac{b_{Fc}}{\bar{\tau}_c} = \frac{1}{\bar{\tau}_c} \int dM n(M)\, b(M)\, V_c(M) \ . \tag{5.27}$$

We note the distinction between the average bias factor of CIV absorbers, for which every absorber is weighted equally and the host halos are weighted by their mean cross section required to produce a certain type of absorbers, and the average bias factor of

the CIV transmission fluctuation, which is what we have measured here, which should be compared to the host halo bias weighted by the absorption volume we have defined here.

5.7 Conclusions

To conclude, we measure the transmission bias of the triply-ionized carbon to be $(1 + \beta_{Fc})b_{Fc} = -0.021 \pm 0.002$, for $\beta_{Fc} = 0.5$ at redshift $z = 2.3$. It corresponds to a physical bias of CIV absorption systems $b_{\tau c} = 2.3$. This is a clustering of the same order as that of Damped Lyα systems.

Acknowledgments

This work is supported in part by Spanish grant AYA-2012-33938. SGG thanks the Lawrence Berkeley Laboratory and the APC for their hospitality during part of the time when this work was being carried out. SGG also thanks Daniel Margala from UCI and NASA's Craig Gordon for the technical support they provided, as well as the BOSS Lyα working group for their comments and suggestions.

Funding for SDSS-III has been provided by the Alfred P. Sloan Foundation, the Participating Institutions, the National Science Foundation, and the U.S. Department of Energy Office of Science. The SDSS-III web site is http://www.sdss3.org/.

SDSS-III is managed by the Astrophysical Research Consortium for the Participating Institutions of the SDSS-III Collaboration including the University of Arizona, the Brazilian Participation Group, Brookhaven National Laboratory, University of Cambridge, Carnegie Mellon University, University of Florida, the French Participation Group, the German Participation Group, Harvard University, the Instituto de Astrofisica de Canarias, the Michigan State/Notre Dame/JINA Participation Group, Johns Hopkins University, Lawrence Berkeley National Laboratory, Max Planck Institute for Astrophysics, Max Planck Institute for Extraterrestrial Physics, New Mexico State University, New York University, Ohio State University, Pennsylvania State University, University of Portsmouth, Princeton University, the Spanish Participation Group, University of Tokyo, University of Utah, Vanderbilt University, University of Virginia, University of Washington, and Yale University.

5.8 Additional figures of the Quasar–CIV forest measurement

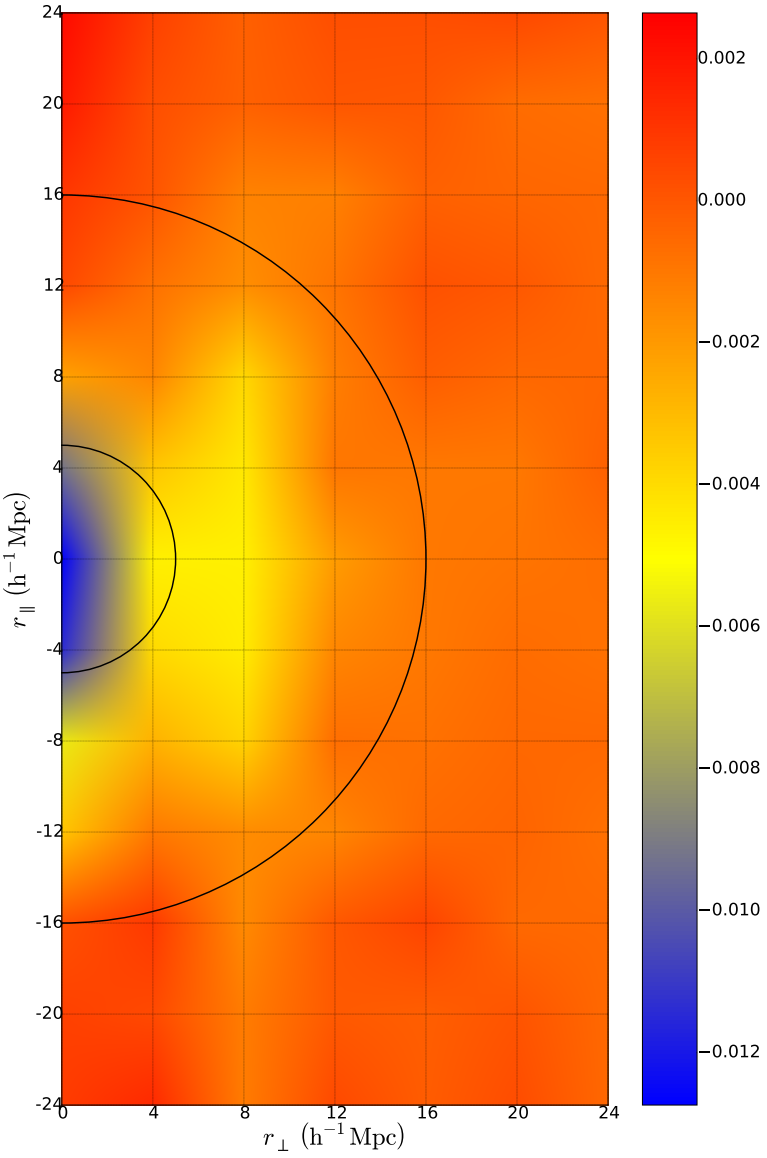

FIGURE 5.8: Contour plot of the Quasar CIV cross-correlation for the full redshift interval $\mathbb{F}$ sample.

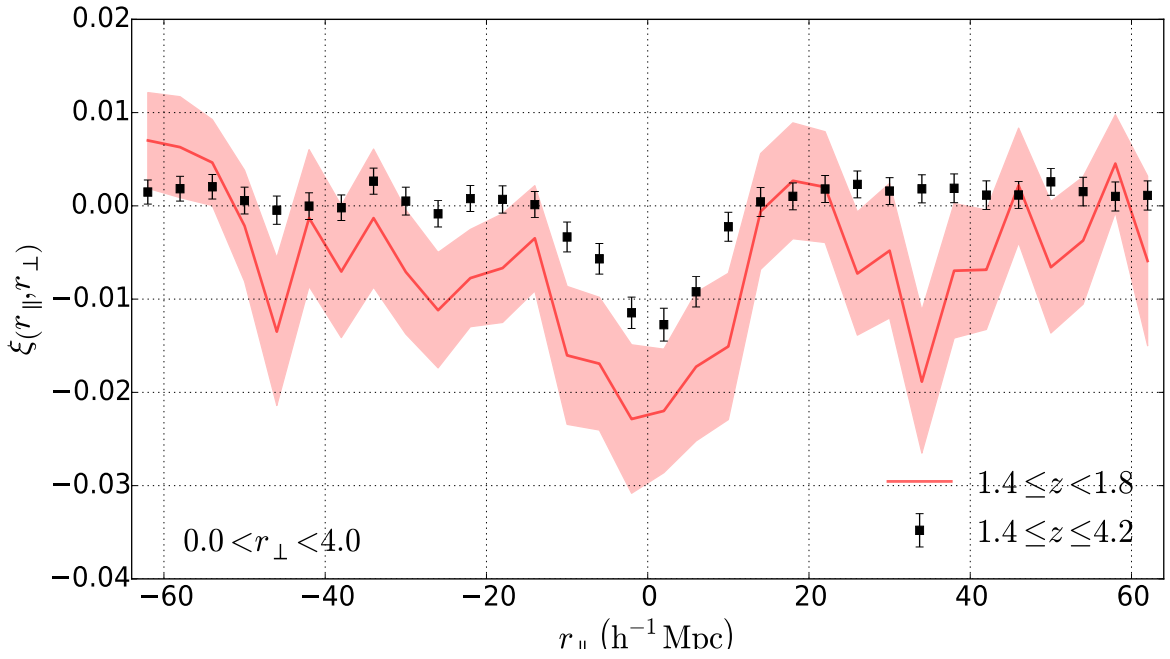

FIGURE 5.9: Comparison between the cross-correlation Quasar-CIV forest measured at vL sample vs. F sample for $0.0 < r_\perp < 4.0$.

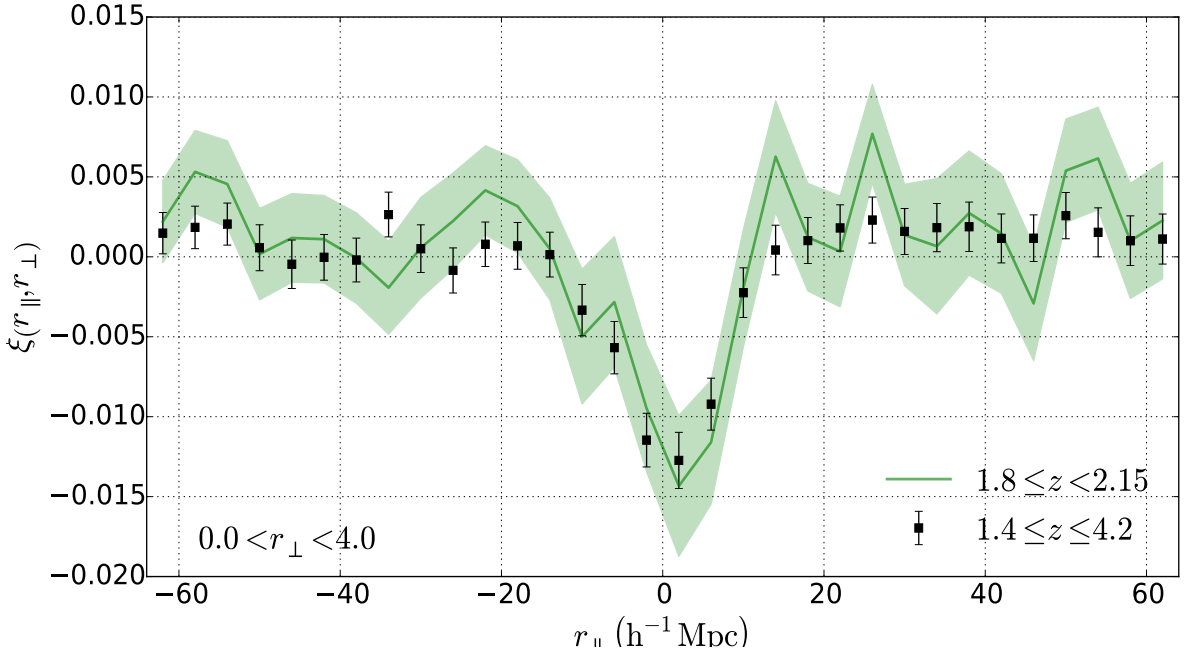

FIGURE 5.10: Comparison between the cross-correlation Quasar-CIV forest measured at L sample vs. F sample for $0.0 < r_\perp < 4.0$.

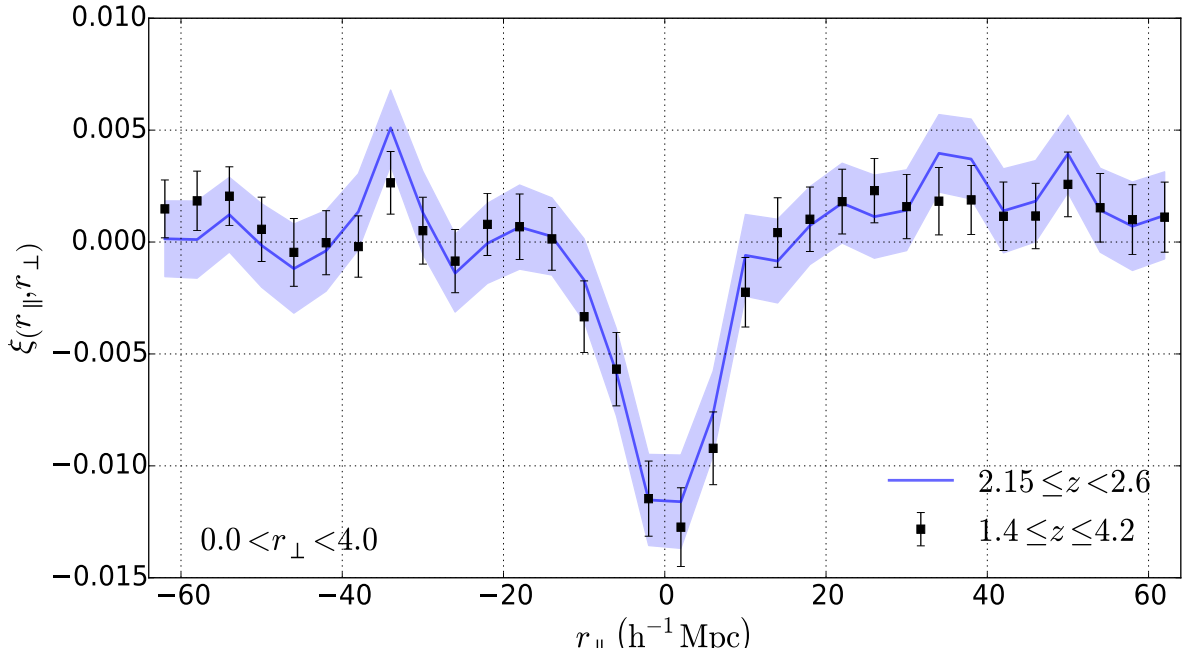

FIGURE 5.11: Comparison between the cross-correlation Quasar-CIV forest measured at $\mathbb{M}$ sample vs. $\mathbb{F}$ sample for $0.0 < r_\perp < 4.0$.

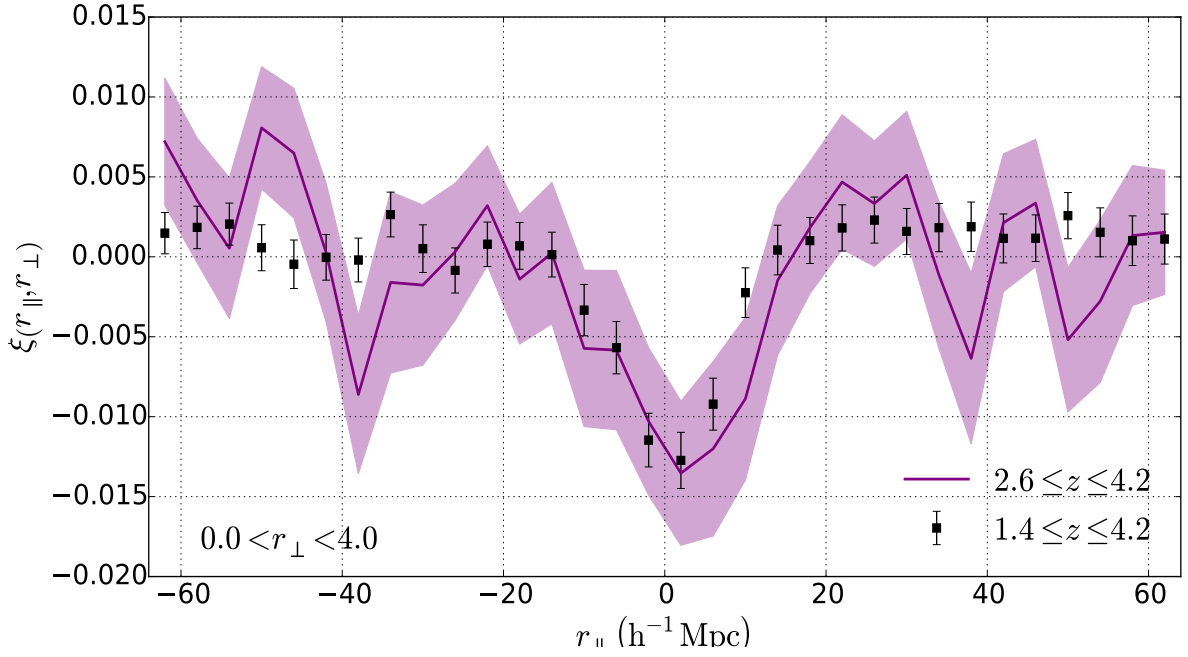

FIGURE 5.12: Comparison between the cross-correlation Quasar-CIV forest measured at $\mathbb{H}$ sample vs. $\mathbb{F}$ sample for $0.0 < r_\perp < 4.0$.

Appendix A

Useful Facts of Cosmology

A.1 On distances in the Universe

Comoving distance v. proper distance

It is the accepted definition that the ***comoving distance*** χ between comoving observers is the fixed unchanging quantity independent of time, while the dynamic, changing distance between them is referred to as the ***proper distance*** d_p. Therefore, comoving and proper distances are numerically equal at the current age of the universe, but will differ in the past and in the future. The proper distance to a galaxy relates to its comoving distance as such:

$$\boxed{d_p(t) = a(t)\chi.} \qquad \text{(proper distance)}$$

Cosmic expansion v. Doppler shift

The generalized ***Copernican principle*** says :

> There is no privileged point in space in the Universe.

This principle is the cornerstone of the difference between redshift due to cosmic expansion and Doppler shift of an object. In the first case, the Universe expands in the same way from any object, or in other words, there is no center for the expansion. In the latter, there is a privileged direction – think about the sound distortion heard when a loud vehicle speeds by you.

Spectroscopic redshift (used in BOSS)

This technique consists in studying the distribution of light of a given galaxy as a function of frequency or wavelength. It is called the ***spectrum*** of a galaxy, see figure A.1. As a reference, we use the measurements conducted on Earth that measured the emission and absorption lines wavelengths in the rest-frame. The challenge is to correctly identify to which atom or molecule do the redshifted lines observed in the spectrum correspond.

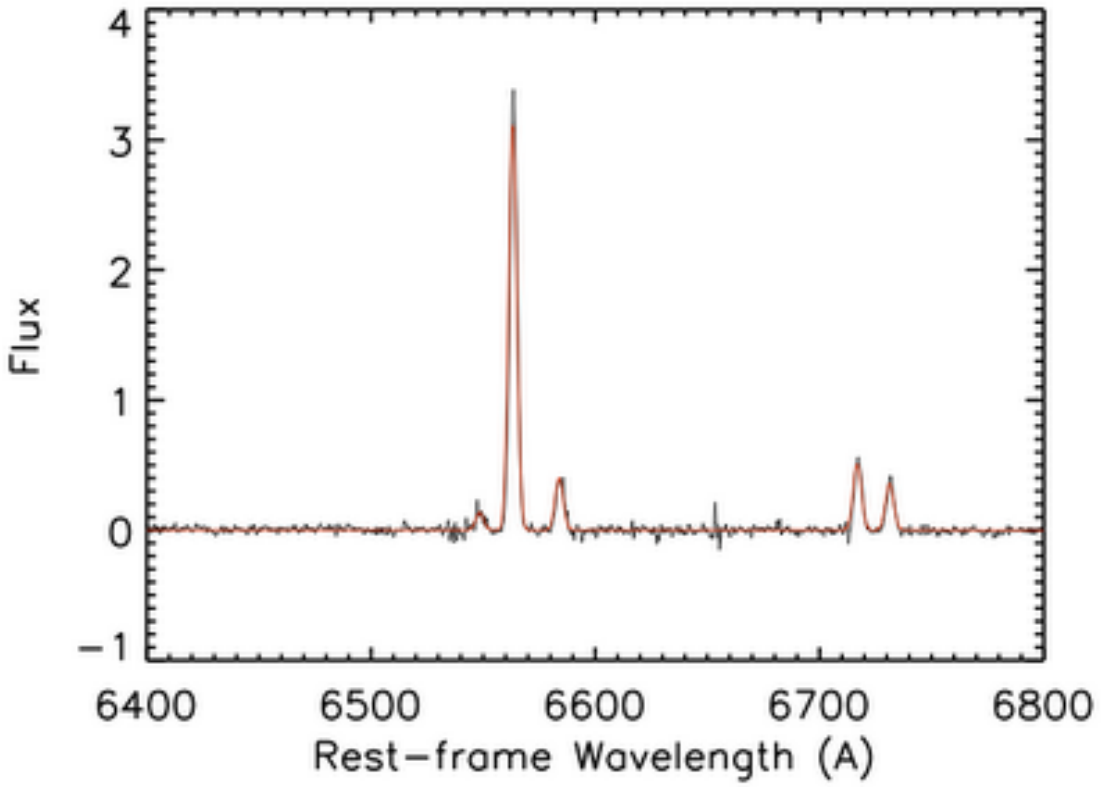

Source: *Dr Jeyhan Kartaltepe*

FIGURE A.1: An example of emission lines in a galaxy spectrum

A.2 Newton's second law to Friedmann's first equation

Let us consider a test particle of mass m on the surface of a sphere of radius R. Newton's second law is written as

$$\vec{F} = -\frac{mMG}{R^2(t)}\vec{u}_r \,. \tag{A.1}$$

Because of the spherical symmetry, and keeping in mind that the acceleration of the expansion of the sphere is expressed by $\ddot{R}$, we can rewrite it as:

$$\ddot{R} = -\frac{MG}{R^2} \quad \Rightarrow \quad \frac{\ddot{R}}{R} = \frac{\ddot{a}}{a} = -\frac{4\pi G}{3}\frac{M}{R^3} \,. \tag{A.2}$$

Multiplying both sides of the equation by $2\dot{R}$ and integrating leads to

$$\frac{\dot{R}^2}{2} - \frac{GM}{R} = \text{cst} \tag{A.3}$$

This equation is similar to a mechanical energy conservation: the first term is looking like a kinetic energy per unit mass and the second one like a potential energy per unit mass. If "cst" >0, the kinetic term dominates and the expansion never ends. If "cst" <0, the potential term dominates and the expansion will eventually stop and reverse. Using the definition of the Hubble constant, playing with the previous equations, and using the fact that "cst" is equal to its value today, we can rewrite equation A.3 as

$$R^2\left(\frac{H^2}{2} - \frac{4\pi G}{3}\rho\right) = R_0^2\left(\frac{H_0^2}{2} - \frac{4\pi G}{3}\rho_0\right) \,. \tag{A.4}$$

With $\rho_c - \rho$ =cst, we can see that a natural scale formatter density arise from our calculations :

$$\rho_c = \frac{3H^2}{8\pi G} \quad \text{or,} \quad \rho_c^0 = \frac{3H_0^2}{8\pi G} \,. \tag{A.5}$$

"cst" has the dimension: [cst]=$[R_0^2 H_0^2]$=[velocity]^2. By convention, and since the only fundamental constant with the same dimension is the speed of light, let us set :

$$kc^2 = R_0^2\left(\frac{4\pi G}{3}\rho_0 - \frac{H_0^2}{2} -\right) \tag{A.6}$$

where k is a dimensionless parameter. Equation A.3 becomes the first Friedmann equation:

$$H^2 = \frac{4\pi G}{3}\rho - \frac{kc^2}{R^2}\,. \tag{A.7}$$

A.3 From General Relativity to the Friedmann equations

This toolbox uses as a reference the course material from Renaud Parentani (LPT Orsay) and Jim Bartlett (APC). A reader interested in a formal introduction to general relativity should take a look at [82], [83] and [84].

A.3.1 GR toolbox

In this section, we will give some essential elements of general relativity. We will focus on the quantities which will help us to derive the covariant generalization of the Friedmann equations. Einstein realized that physics should not be frame dependent and so he introduced the notion of *tensor* to the physics community. Those objects are quantities from differential geometry that transform in a specific *covariant* way under coordinates or frame transformation. Einstein postulated that the equations governing gravity should be covariant and of second order. To that effect, he wrote a very general second order tensor to describe gravitational effects. To proceed further, one has to realize that the existence of a tensor is bound to the existence of *curved* space-times. In curved space-time, the derivative ∂_μ of a given quantity is, in most cases, not a tensor anymore. For a given vector v^μ, one has to define a new covariant derivative:

$$\nabla_\mu v^\nu \equiv \partial_\mu v^\nu + \Gamma^\nu_{\mu\alpha} v^\alpha\,. \tag{A.8}$$

The $\Gamma^\nu_{\mu\alpha}$ are called the ***Christoffel symbols*** and have been precisely introduced to account for the non-tensoricity of the first term. By considering a general coordinates transformation, it is possible to obtain an expression for $\Gamma^\nu_{\mu\alpha}$ in term of the metric tensor $g_{\mu\nu}$ and its derivatives:

$$\Gamma^\nu_{\mu\alpha} = \frac{1}{2} g^{\alpha\beta}\left(\partial_\nu g_{\mu\beta} + \partial_\mu g_{\nu\beta} - \partial_\beta g_{\mu\nu}\right)\,. \tag{A.9}$$

The metric tensor $g_{\mu\nu}$ can be written as a 4×4 matrix. In the case of equation FLRW, in chapter 2, it is

$$g_{\mu\nu} = \begin{pmatrix} 1 & 0 & 0 & 0 \\ 0 & -1 & 0 & 0 \\ 0 & 0 & -1 & 0 \\ 0 & 0 & 0 & -1 \end{pmatrix} . \tag{A.10}$$

By definition, the Christoffel symbols encode some curvature effect. They would vanish in a non-curved (i.e. flat) space-time. However they are not tensors. It is possible to construct a tensor that quantifies how curved a space-time is. It is called the Riemann tensor $R^{\mu}_{\delta\alpha\beta}$:

$$[\nabla_\alpha, \nabla_\beta]v^\mu \equiv R^{\mu}_{\delta\alpha\beta}v^\delta \, . \tag{A.11}$$

Using equations A.8 and A.9, we can make the calculation of equation A.11, that gives an expression for the Riemann tensor in term of the Christoffel symbols:

$$\boxed{R^{\delta}_{\alpha\beta\mu} = \partial_\beta\Gamma^{\delta}_{\alpha\mu} - \partial_\alpha\Gamma^{\delta}_{\beta\mu} + \Gamma^{\mu}_{\alpha\mu}\Gamma^{\delta}_{\beta\nu} + \Gamma^{\mu}_{\beta\mu}\Gamma^{\delta}_{\alpha\nu} \, .} \qquad \text{(Riemann tensor)}$$

The Riemann tensor verifies the following four properties. (a) It vanishes for a flat space because of the symmetry of second derivatives (Schwartz theorem, i.e. derivatives swap is allowed). (b) It is antisymmetric under the permutation of the last two indices. (c) It is symmetric under the permutation of the first two index with the last two. And finally, (d) it verifies the Bianchi identities.

We can define the Ricci tensor:

$$\boxed{R_{\alpha\beta} \equiv R^{\mu}_{\alpha\mu\beta}} \qquad \text{(Ricci tensor)}$$

which is symmetric by propagation of the properties of the Riemann tensor. We finally define the Ricci scalar:

$$\boxed{R \equiv R^{\mu}_{\mu} \, .} \qquad \text{(Ricci scalar)}$$

We can now write a general tensor that can describe gravitational phenomenon. It is the Einstein tensor:

$$G_{\mu\nu} \equiv R_{\mu\nu} - \frac{R}{2}g_{\mu\nu} \, . \tag{A.12}$$

From the Bianchi identities, $\nabla^\mu G_{\mu\nu} = 0$. If we replace the Ricci scalar R by $R - 2\Lambda$, the Bianchi identities would still be fulfilled. As a results, we can write the most general Einstein tensor:

$$\boxed{G_{\mu\nu} \equiv R_{\mu\nu} - \frac{R}{2} g_{\mu\nu} + \Lambda g_{\mu\nu}\,.} \qquad \text{(Einstein tensor)}$$

The Einstein equations are

$$\boxed{G_{\mu\nu} = 8\pi G T_{\mu\nu}} \qquad \text{(Einstein equations)}$$

where G is the gravitational constant and $T_{\mu\nu}$ is the *stress energy tensor*. In other words, the energy-momentum tensor describes the distribution of matter in the Universe. It is interesting to note the parallel with Maxwell's law of electromagnetism: $\partial_\nu F^{\mu\nu} = \frac{4\pi}{c} J^\nu$. In both cases, the right-end side represents the *charge acting as a source* for the *field* presented on the left-end side. Einstein equations governs how matter $T_{\mu\nu}$ evolves for a given geometry $G_{\mu\nu}$. Reversely, Einstein equations also show how the matter content of the Universe affects its geometry.

A.3.2 Friedmann equations

Using the FLRW metric, and the Einstein equations, the associated Christoffels symbols are :

$$\Gamma^0_{\mu\nu} = \begin{pmatrix} 0 & 0 & 0 & 0 \\ 0 & \frac{a\dot{a}}{1-\kappa r^2} & 0 & 0 \\ 0 & 0 & a\dot{a}r^2 & 0 \\ 0 & 0 & 0 & a\dot{a}r^2 \sin^2\theta \end{pmatrix},$$

$$\Gamma^1_{\mu\nu} = \begin{pmatrix} 0 & \frac{\dot{a}}{a} & 0 & 0 \\ \frac{\dot{a}}{a} & \frac{\kappa r}{1-\kappa r^2} & 0 & 0 \\ 0 & 0 & r(\kappa r^2 - 1) & 0 \\ 0 & 0 & 0 & (r\sin^2\theta)(\kappa r^2 - 1) \end{pmatrix},$$

$$\Gamma^2_{\mu\nu} = \begin{pmatrix} 0 & \frac{\dot{a}}{a} & 0 & 0 \\ \frac{\dot{a}}{a} & 0 & \frac{1}{r} & 0 \\ \frac{1}{r} & 0 & 0 & 0 \\ 0 & 0 & 0 & -\sin\theta\cos\theta \end{pmatrix},$$

$$\text{and} \quad \Gamma^3_{\mu\nu} = \begin{pmatrix} 0 & 0 & 0 & \frac{\dot{a}}{a} \\ 0 & 0 & 0 & \frac{1}{r} \\ 0 & 0 & 0 & \cot\theta \\ \frac{\dot{a}}{a} & \frac{1}{r} & \cot\theta & 0 \end{pmatrix}.$$

Using the Riemann tensor, we have derive the expression of the Ricci tensor. In this case, it is diagonal :

$$\begin{cases} R_{00} = 3\frac{\ddot{a}}{a} \\ R_{11} = \frac{a\ddot{a}+2\dot{a}^2+2\kappa}{\kappa r^2-1} \\ R_{22} = -r^2(a\ddot{a}+2\dot{a}^2+2\kappa) \\ R_{33} = R_{22}\sin^2\theta \end{cases} \tag{A.13}$$

The curvature scalar, or Ricci scalar is :

$$R = R_{00} - \frac{1-\kappa r^2}{a^2}R_{11} - \frac{1}{a^2r^2}R_{22} - \frac{1}{a^2r^2\sin^2\theta}R_{33} \tag{A.14}$$

which gives, when replacing with elements of A.13

$$R = 6\left(\frac{\ddot{a}}{a} + \left(\frac{\dot{a}}{a}\right)^2 + \frac{\kappa}{a^2}\right). \tag{A.15}$$

Finally, we can derive the left-end side of the Einstein equations:

$$\begin{cases} G_{00} = -3\left(\left(\frac{\dot{a}}{a}\right)^2 + \frac{\kappa}{a^2}\right) \\ G_{11} = \frac{a^2}{1-\kappa r^2}\left(\frac{\ddot{a}}{a} + \left(\frac{dota}{a}\right)^2 + \frac{\kappa}{a^2}\right) \\ G_{22} = a^2r^2\left(2\frac{\ddot{a}}{a} + \left(\frac{dota}{a}\right)^2 + \frac{\kappa}{a^2}\right) \\ G_{33} = G_{22}\sin^2\theta \end{cases} \tag{A.16}$$

where the non-diagonal terms are null. If we assume that the Universe is filled with perfect fluids, we can write the stress energy tensor as : $T_{\mu\nu} = (\rho + P)\delta^0_\mu\delta^0_\nu - Pg_{\mu\nu}$.

The ***Friedmann equations*** are obtained simply by establishing $G_{ii} = 8\pi G T_{ii}$.

A.4 Useful converter

♢ **Time-Temperature correspondance.**

In a thermal equilibrium regime where $T \ll m$ (see [85]):

$$t \sim \left(\frac{T}{MeV}\right)^{-n} \equiv \left(\frac{E}{MeV}\right)^{-n} \equiv \left(\frac{E_0(z+1)}{MeV}\right)^{-n} \tag{A.17}$$

where $n = 2$ in radiation dominated era and $n = \frac{3}{2}$ in matter dominated era.

Bibliography

[1] V. C. Rubin and W. K. Ford, Jr. Rotation of the Andromeda Nebula from a Spectroscopic Survey of Emission Regions. *ApJ*, 159:379, February 1970. doi: 10.1086/150317.

[2] G. Hinshaw, D. Larson, E. Komatsu, D. N. Spergel, C. L. Bennett, J. Dunkley, M. R. Nolta, M. Halpern, R. S. Hill, N. Odegard, L. Page, K. M. Smith, J. L. Weiland, B. Gold, N. Jarosik, A. Kogut, M. Limon, S. S. Meyer, G. S. Tucker, E. Wollack, and E. L. Wright. Nine-year Wilkinson Microwave Anisotropy Probe (WMAP) Observations: Cosmological Parameter Results. *ApJS*, 208:19, October 2013. doi: 10.1088/0067-0049/208/2/19.

[3] E. Hubble. A Relation between Distance and Radial Velocity among Extra-Galactic Nebulae. *Proceedings of the National Academy of Science*, 15:168–173, March 1929. doi: 10.1073/pnas.15.3.168.

[4] P. A. R. Ade et al. Planck 2015 results. XIII. Cosmological parameters. *Astron. Astrophys.*, 594:A13, 2016. doi: 10.1051/0004-6361/201525830.

[5] W. H. Kinney. TASI Lectures on Inflation. *ArXiv e-prints*, February 2009.

[6] P. Petitjean. QSO Absorption Line Systems. *ArXiv Astrophysics e-prints*, October 1998.

[7] B. E. Robertson, R. S. Ellis, J. S. Dunlop, R. J. McLure, and D. P. Stark. Early star-forming galaxies and the reionization of the Universe. *Nature*, 468:49–55, November 2010. doi: 10.1038/nature09527.

[8] R. J. Bouwens, G. D. Illingworth, P. A. Oesch, I. Labbé, M. Trenti, P. van Dokkum, M. Franx, M. Stiavelli, C. M. Carollo, D. Magee, and V. Gonzalez. Ultraviolet Luminosity Functions from 132 z ˜ 7 and z ˜ 8 Lyman-break Galaxies in the Ultra-deep HUDF09 and Wide-area Early Release Science WFC3/IR Observations. *ApJ*, 737:90, August 2011. doi: 10.1088/0004-637X/737/2/90.

[9] F. Fontanot, S. Cristiani, and E. Vanzella. On the relative contribution of high-redshift galaxies and active galactic nuclei to reionization. *MNRAS*, 425:1413–1420, September 2012. doi: 10.1111/j.1365-2966.2012.21594.x.

[10] J. S. B. Wyithe, A. M. Hopkins, M. D. Kistler, H. YÃijksel, and J. F. Beacom. Determining the escape fraction of ionizing photons during reionization with the grb-derived star formation rate. *Monthly Notices of the Royal Astronomical Society*, 401(4):2561–2571, 2010. ISSN 1365-2966. doi: 10.1111/j.1365-2966.2009.15834.x. URL http://dx.doi.org/10.1111/j.1365-2966.2009.15834.x.

[11] P. Madau, F. Haardt, and M. J. Rees. Radiative Transfer in a Clumpy Universe. III. The Nature of Cosmological Ionizing Sources. *ApJ*, 514:648–659, April 1999. doi: 10.1086/306975.

[12] N. G. Busca, T. Delubac, J. Rich, S. Bailey, A. Font-Ribera, D. Kirkby, J.-M. Le Goff, M. M. Pieri, A. Slosar, É. Aubourg, J. E. Bautista, D. Bizyaev, M. Blomqvist, A. S. Bolton, J. Bovy, H. Brewington, A. Borde, J. Brinkmann, B. Carithers, R. A. C. Croft, K. S. Dawson, G. Ebelke, D. J. Eisenstein, J.-C. Hamilton, S. Ho, D. W. Hogg, K. Honscheid, K.-G. Lee, B. Lundgren, E. Malanushenko, V. Malanushenko, D. Margala, C. Maraston, K. Mehta, J. Miralda-Escudé, A. D. Myers, R. C. Nichol, P. Noterdaeme, M. D. Olmstead, D. Oravetz, N. Palanque-Delabrouille, K. Pan, I. Pâris, W. J. Percival, P. Petitjean, N. A. Roe, E. Rollinde, N. P. Ross, G. Rossi, D. J. Schlegel, D. P. Schneider, A. Shelden, E. S. Sheldon, A. Simmons, S. Snedden, J. L. Tinker, M. Viel, B. A. Weaver, D. H. Weinberg, M. White, C. Yèche, and D. G. York. Baryon acoustic oscillations in the Lyα forest of BOSS quasars. *A&A*, 552:A96, April 2013. doi: 10.1051/0004-6361/201220724.

[13] A. Slosar, V. Iršič, D. Kirkby, S. Bailey, N. G. Busca, T. Delubac, J. Rich, É. Aubourg, J. E. Bautista, V. Bhardwaj, M. Blomqvist, A. S. Bolton, J. Bovy, J. Brownstein, B. Carithers, R. A. C. Croft, K. S. Dawson, A. Font-Ribera, J.-M. Le Goff, S. Ho, K. Honscheid, K.-G. Lee, D. Margala, P. McDonald, B. Medolin, J. Miralda-Escudé, A. D. Myers, R. C. Nichol, P. Noterdaeme, N. Palanque-Delabrouille, I. Pâris, P. Petitjean, M. M. Pieri, Y. Piškur, N. A. Roe, N. P. Ross, G. Rossi, D. J. Schlegel, D. P. Schneider, N. Suzuki, E. S. Sheldon, U. Seljak, M. Viel, D. H. Weinberg, and C. Yèche. Measurement of baryon acoustic oscillations in the Lyman-α forest fluctuations in BOSS data release 9. *J. Cosmology Astropart. Phys.*, 4:026, April 2013. doi: 10.1088/1475-7516/2013/04/026.

[14] A. Font-Ribera, D. Kirkby, N. Busca, J. Miralda-Escudé, N. P. Ross, A. Slosar, J. Rich, É. Aubourg, S. Bailey, V. Bhardwaj, J. Bautista, F. Beutler, D. Bizyaev, M. Blomqvist, H. Brewington, J. Brinkmann, J. R. Brownstein, B. Carithers, K. S.

Dawson, T. Delubac, G. Ebelke, D. J. Eisenstein, J. Ge, K. Kinemuchi, K.-G. Lee, V. Malanushenko, E. Malanushenko, M. Marchante, D. Margala, D. Muna, A. D. Myers, P. Noterdaeme, D. Oravetz, N. Palanque-Delabrouille, I. Pâris, P. Petitjean, M. M. Pieri, G. Rossi, D. P. Schneider, A. Simmons, M. Viel, C. Yeche, and D. G. York. Quasar-Lyman α forest cross-correlation from BOSS DR11: Baryon Acoustic Oscillations. *J. Cosmology Astropart. Phys.*, 5:027, May 2014. doi: 10.1088/1475-7516/2014/05/027.

[15] S. Gontcho A Gontcho, J. Miralda-Escudé, and N. G. Busca. On the effect of the ionizing background on the Lyα forest autocorrelation function. *MNRAS*, 442: 187–195, July 2014. doi: 10.1093/mnras/stu860.

[16] R. A. C. Croft, D. H. Weinberg, N. Katz, and L. Hernquist. Recovery of the Power Spectrum of Mass Fluctuations from Observations of the Lyα Forest. *ApJ*, 495: 44–62, March 1998. doi: 10.1086/305289.

[17] R. A. C. Croft, D. H. Weinberg, M. Pettini, L. Hernquist, and N. Katz. The Power Spectrum of Mass Fluctuations Measured from the Lyα Forest at Redshift z = 2.5. *ApJ*, 520:1–23, July 1999. doi: 10.1086/307438.

[18] P. McDonald, J. Miralda-Escudé, M. Rauch, W. L. W. Sargent, T. A. Barlow, R. Cen, and J. P. Ostriker. The Observed Probability Distribution Function, Power Spectrum, and Correlation Function of the Transmitted Flux in the Lyα Forest. *ApJ*, 543:1–23, November 2000. doi: 10.1086/317079.

[19] R. A. C. Croft, D. H. Weinberg, M. Bolte, S. Burles, L. Hernquist, N. Katz, D. Kirkman, and D. Tytler. Toward a Precise Measurement of Matter Clustering: Lyα Forest Data at Redshifts 2-4. *ApJ*, 581:20–52, December 2002. doi: 10.1086/344099.

[20] P. McDonald, U. Seljak, S. Burles, D. J. Schlegel, D. H. Weinberg, R. Cen, D. Shih, J. Schaye, D. P. Schneider, N. A. Bahcall, J. W. Briggs, J. Brinkmann, R. J. Brunner, M. Fukugita, J. E. Gunn, Ž. Ivezić, S. Kent, R. H. Lupton, and D. E. Vanden Berk. The Lyα Forest Power Spectrum from the Sloan Digital Sky Survey. *ApJS*, 163: 80–109, March 2006. doi: 10.1086/444361.

[21] D. J. Eisenstein, D. H. Weinberg, E. Agol, H. Aihara, C. Allende Prieto, S. F. Anderson, J. A. Arns, É. Aubourg, S. Bailey, E. Balbinot, and et al. SDSS-III: Massive Spectroscopic Surveys of the Distant Universe, the Milky Way, and Extra-Solar Planetary Systems. *AJ*, 142:72, September 2011. doi: 10.1088/0004-6256/142/3/72.

[22] K. S. Dawson, D. J. Schlegel, C. P. Ahn, S. F. Anderson, É. Aubourg, S. Bailey, R. H. Barkhouser, J. E. Bautista, A. Beifiori, A. A. Berlind, V. Bhardwaj, D. Bizyaev,

C. H. Blake, M. R. Blanton, M. Blomqvist, A. S. Bolton, A. Borde, J. Bovy, W. N. Brandt, H. Brewington, J. Brinkmann, P. J. Brown, J. R. Brownstein, K. Bundy, N. G. Busca, W. Carithers, A. R. Carnero, M. A. Carr, Y. Chen, J. Comparat, N. Connolly, F. Cope, R. A. C. Croft, A. J. Cuesta, L. N. da Costa, J. R. A. Davenport, T. Delubac, R. de Putter, S. Dhital, A. Ealet, G. L. Ebelke, D. J. Eisenstein, S. Escoffier, X. Fan, N. Filiz Ak, H. Finley, A. Font-Ribera, R. Génova-Santos, J. E. Gunn, H. Guo, D. Haggard, P. B. Hall, J.-C. Hamilton, B. Harris, D. W. Harris, S. Ho, D. W. Hogg, D. Holder, K. Honscheid, J. Huehnerhoff, B. Jordan, W. P. Jordan, G. Kauffmann, E. A. Kazin, D. Kirkby, M. A. Klaene, J.-P. Kneib, J.-M. Le Goff, K.-G. Lee, D. C. Long, C. P. Loomis, B. Lundgren, R. H. Lupton, M. A. G. Maia, M. Makler, E. Malanushenko, V. Malanushenko, R. Mandelbaum, M. Manera, C. Maraston, D. Margala, K. L. Masters, C. K. McBride, P. McDonald, I. D. McGreer, R. G. McMahon, O. Mena, J. Miralda-Escudé, A. D. Montero-Dorta, F. Montesano, D. Muna, A. D. Myers, T. Naugle, R. C. Nichol, P. Noterdaeme, S. E. Nuza, M. D. Olmstead, A. Oravetz, D. J. Oravetz, R. Owen, N. Padmanabhan, N. Palanque-Delabrouille, K. Pan, J. K. Parejko, I. Pâris, W. J. Percival, I. Pérez-Fournon, I. Pérez-Ràfols, P. Petitjean, R. Pfaffenberger, J. Pforr, M. M. Pieri, F. Prada, A. M. Price-Whelan, M. J. Raddick, R. Rebolo, J. Rich, G. T. Richards, C. M. Rockosi, N. A. Roe, A. J. Ross, N. P. Ross, G. Rossi, J. A. Rubiño-Martin, L. Samushia, A. G. Sánchez, C. Sayres, S. J. Schmidt, D. P. Schneider, C. G. Scóccola, H.-J. Seo, A. Shelden, E. Sheldon, Y. Shen, Y. Shu, A. Slosar, S. A. Smee, S. A. Snedden, F. Stauffer, O. Steele, M. A. Strauss, A. Streblyanska, N. Suzuki, M. E. C. Swanson, T. Tal, M. Tanaka, D. Thomas, J. L. Tinker, R. Tojeiro, C. A. Tremonti, M. Vargas Magaña, L. Verde, M. Viel, D. A. Wake, M. Watson, B. A. Weaver, D. H. Weinberg, B. J. Weiner, A. A. West, M. White, W. M. Wood-Vasey, C. Yeche, I. Zehavi, G.-B. Zhao, and Z. Zheng. The Baryon Oscillation Spectroscopic Survey of SDSS-III. *AJ*, 145:10, January 2013. doi: 10.1088/0004-6256/145/1/10.

[23] A. Slosar, A. Font-Ribera, M. M. Pieri, J. Rich, J.-M. Le Goff, É. Aubourg, J. Brinkmann, N. Busca, B. Carithers, R. Charlassier, M. Cortês, R. Croft, K. S. Dawson, D. Eisenstein, J.-C. Hamilton, S. Ho, K.-G. Lee, R. Lupton, P. McDonald, B. Medolin, D. Muna, J. Miralda-Escudé, A. D. Myers, R. C. Nichol, N. Palanque-Delabrouille, I. Pâris, P. Petitjean, Y. Piškur, E. Rollinde, N. P. Ross, D. J. Schlegel, D. P. Schneider, E. Sheldon, B. A. Weaver, D. H. Weinberg, C. Yeche, and D. G. York. The Lyman-α forest in three dimensions: measurements of large scale flux correlations from BOSS 1st-year data. *J. Cosmology Astropart. Phys.*, 9:001, September 2011. doi: 10.1088/1475-7516/2011/09/001.

[24] L. Zuo. Fluctuations in the ionizing background. *MNRAS*, 258:36–44, September 1992. doi: 10.1093/mnras/258.1.36.

[25] R. A. C. Croft. Ionizing Radiation Fluctuations and Large-Scale Structure in the Lyα Forest. *ApJ*, 610:642–662, August 2004. doi: 10.1086/421839.

[26] A. Meiksin and M. White. The effects of ultraviolet background correlations on Lyα forest flux statistics. *MNRAS*, 350:1107–1126, May 2004. doi: 10.1111/j.1365-2966.2004.07724.x.

[27] P. McDonald, U. Seljak, R. Cen, P. Bode, and J. P. Ostriker. Physical effects on the Lyα forest flux power spectrum: damping wings, ionizing radiation fluctuations and galactic winds. *MNRAS*, 360:1471–1482, July 2005. doi: 10.1111/j.1365-2966.2005.09141.x.

[28] A. Slosar, S. Ho, M. White, and T. Louis. The acoustic peak in the Lyman alpha forest. *J. Cosmology Astropart. Phys.*, 10:019, October 2009. doi: 10.1088/1475-7516/2009/10/019.

[29] M. White, A. Pope, J. Carlson, K. Heitmann, S. Habib, P. Fasel, D. Daniel, and Z. Lukic. Particle Mesh Simulations of the Lyα Forest and the Signature of Baryon Acoustic Oscillations in the Intergalactic Medium. *ApJ*, 713:383–393, April 2010. doi: 10.1088/0004-637X/713/1/383.

[30] T. Delubac, J. E. Bautista, N. G. Busca, J. Rich, D. Kirkby, S. Bailey, A. Font-Ribera, A. Slosar, K.-G. Lee, M. M. Pieri, J.-C. Hamilton, É. Aubourg, M. Blomqvist, J. Bovy, J. Brinkmann, W. Carithers, K. S. Dawson, D. J. Eisenstein, S. G. A. Gontcho, J.-P. Kneib, J.-M. Le Goff, D. Margala, J. Miralda-Escudé, A. D. Myers, R. C. Nichol, P. Noterdaeme, R. O'Connell, M. D. Olmstead, N. Palanque-Delabrouille, I. Pâris, P. Petitjean, N. P. Ross, G. Rossi, D. J. Schlegel, D. P. Schneider, D. H. Weinberg, C. Yèche, and D. G. York. Baryon acoustic oscillations in the Lyα forest of BOSS DR11 quasars. *A&A*, 574:A59, February 2015. doi: 10.1051/0004-6361/201423969.

[31] Planck Collaboration, P. A. R. Ade, N. Aghanim, C. Armitage-Caplan, M. Arnaud, M. Ashdown, F. Atrio-Barandela, J. Aumont, C. Baccigalupi, A. J. Banday, and et al. Planck 2013 results. XVI. Cosmological parameters. *A&A*, 571:A16, November 2014. doi: 10.1051/0004-6361/201321591.

[32] A. Pontzen. Scale-dependent bias in the baryonic-acoustic-oscillation-scale intergalactic neutral hydrogen. *Phys. Rev. D*, 89(8):083010, April 2014. doi: 10.1103/PhysRevD.89.083010.

[33] N. Kaiser. Clustering in real space and in redshift space. *MNRAS*, 227:1–21, July 1987. doi: 10.1093/mnras/227.1.1.

[34] P. McDonald. Toward a Measurement of the Cosmological Geometry at z ˜ 2: Predicting Lyα Forest Correlation in Three Dimensions and the Potential of Future Data Sets. *ApJ*, 585:34–51, March 2003. doi: 10.1086/345945.

[35] N. P. Ross, I. D. McGreer, M. White, G. T. Richards, A. D. Myers, N. Palanque-Delabrouille, M. A. Strauss, S. F. Anderson, Y. Shen, W. N. Brandt, C. Yèche, M. E. C. Swanson, É. Aubourg, S. Bailey, D. Bizyaev, J. Bovy, H. Brewington, J. Brinkmann, C. DeGraf, T. Di Matteo, G. Ebelke, X. Fan, J. Ge, E. Malanushenko, V. Malanushenko, R. Mandelbaum, C. Maraston, D. Muna, D. Oravetz, K. Pan, I. Pâris, P. Petitjean, K. Schawinski, D. J. Schlegel, D. P. Schneider, J. D. Silverman, A. Simmons, S. Snedden, A. Streblyanska, N. Suzuki, D. H. Weinberg, and D. York. The SDSS-III Baryon Oscillation Spectroscopic Survey: The Quasar Luminosity Function from Data Release Nine. *ApJ*, 773:14, August 2013. doi: 10.1088/0004-637X/773/1/14.

[36] C. P. Ahn, R. Alexandroff, C. Allende Prieto, S. F. Anderson, T. Anderton, B. H. Andrews, É. Aubourg, S. Bailey, E. Balbinot, R. Barnes, and et al. The Ninth Data Release of the Sloan Digital Sky Survey: First Spectroscopic Data from the SDSS-III Baryon Oscillation Spectroscopic Survey. *ApJS*, 203:21, December 2012. doi: 10.1088/0067-0049/203/2/21.

[37] A. Font-Ribera, E. Arnau, J. Miralda-Escudé, E. Rollinde, J. Brinkmann, J. R. Brownstein, K.-G. Lee, A. D. Myers, N. Palanque-Delabrouille, I. Pâris, P. Petitjean, J. Rich, N. P. Ross, D. P. Schneider, and M. White. The large-scale quasar-Lyman α forest cross-correlation from BOSS. *J. Cosmology Astropart. Phys.*, 5:018, May 2013. doi: 10.1088/1475-7516/2013/05/018.

[38] A. Font-Ribera, J. Miralda-Escudé, E. Arnau, B. Carithers, K.-G. Lee, P. Noterdaeme, I. Pâris, P. Petitjean, J. Rich, E. Rollinde, N. P. Ross, D. P. Schneider, M. White, and D. G. York. The large-scale cross-correlation of Damped Lyman alpha systems with the Lyman alpha forest: first measurements from BOSS. *J. Cosmology Astropart. Phys.*, 11:059, November 2012. doi: 10.1088/1475-7516/2012/11/059.

[39] A. Font-Ribera and J. Miralda-Escudé. The effect of high column density systems on the measurement of the Lyman-α forest correlation function. *J. Cosmology Astropart. Phys.*, 7:028, July 2012. doi: 10.1088/1475-7516/2012/07/028.

[40] M. White, A. D. Myers, N. P. Ross, D. J. Schlegel, J. F. Hennawi, Y. Shen, I. McGreer, M. A. Strauss, A. S. Bolton, J. Bovy, X. Fan, J. Miralda-Escude, N. Palanque-Delabrouille, I. Paris, P. Petitjean, D. P. Schneider, M. Viel, D. H. Weinberg, C. Yeche, I. Zehavi, K. Pan, S. Snedden, D. Bizyaev, H. Brewington, J. Brinkmann, V. Malanushenko, E. Malanushenko, D. Oravetz, A. Simmons, A. Sheldon, and

B. A. Weaver. The clustering of intermediate-redshift quasars as measured by the Baryon Oscillation Spectroscopic Survey. *MNRAS*, 424:933–950, August 2012. doi: 10.1111/j.1365-2966.2012.21251.x.

[41] J. Miralda and J. P. Ostriker. What is Producing the Ionizing Background at Large Redshift? In *Bulletin of the American Astronomical Society*, volume 20 of *BAAS*, page 1002, September 1988.

[42] F. Haardt and P. Madau. Radiative Transfer in a Clumpy Universe. II. The Ultraviolet Extragalactic Background. *ApJ*, 461:20, April 1996. doi: 10.1086/177035.

[43]

[44] G. Worseck, J. X. Prochaska, M. McQuinn, A. Dall'Aglio, C. Fechner, J. F. Hennawi, D. Reimers, P. Richter, and L. Wisotzki. The End of Helium Reionization at z ˜= 2.7 Inferred from Cosmic Variance in HST/COS He II Lyα Absorption Spectra. *ApJ*, 733:L24, June 2011. doi: 10.1088/2041-8205/733/2/L24.

[45] J. Miralda-Escudé and M. J. Rees. Reionization and thermal evolution of a photoionized intergalactic medium. *MNRAS*, 266:343–352, January 1994. doi: 10.1093/mnras/266.2.343.

[46] M. McQuinn, A. Lidz, M. Zaldarriaga, L. Hernquist, P. F. Hopkins, S. Dutta, and C.-A. Faucher-Giguère. He II Reionization and its Effect on the Intergalactic Medium. *ApJ*, 694:842–866, April 2009. doi: 10.1088/0004-637X/694/2/842.

[47] K. S. Dawson, D. J. Schlegel, C. P. Ahn, S. F. Anderson, É. Aubourg, S. Bailey, R. H. Barkhouser, J. E. Bautista, A. Beifiori, A. A. Berlind, V. Bhardwaj, D. Bizyaev, C. H. Blake, M. R. Blanton, M. Blomqvist, A. S. Bolton, A. Borde, J. Bovy, W. N. Brandt, H. Brewington, J. Brinkmann, P. J. Brown, J. R. Brownstein, K. Bundy, N. G. Busca, W. Carithers, A. R. Carnero, M. A. Carr, Y. Chen, J. Comparat, N. Connolly, F. Cope, R. A. C. Croft, A. J. Cuesta, L. N. da Costa, J. R. A. Davenport, T. Delubac, R. de Putter, S. Dhital, A. Ealet, G. L. Ebelke, D. J. Eisenstein, S. Escoffier, X. Fan, N. Filiz Ak, H. Finley, A. Font-Ribera, R. Génova-Santos, J. E. Gunn, H. Guo, D. Haggard, P. B. Hall, J.-C. Hamilton, B. Harris, D. W. Harris, S. Ho, D. W. Hogg, D. Holder, K. Honscheid, J. Huehnerhoff, B. Jordan, W. P. Jordan, G. Kauffmann, E. A. Kazin, D. Kirkby, M. A. Klaene, J.-P. Kneib, J.-M. Le Goff, K.-G. Lee, D. C. Long, C. P. Loomis, B. Lundgren, R. H. Lupton, M. A. G. Maia, M. Makler, E. Malanushenko, V. Malanushenko, R. Mandelbaum, M. Manera, C. Maraston, D. Margala, K. L. Masters, C. K. McBride, P. McDonald, I. D. McGreer, R. G. McMahon, O. Mena, J. Miralda-Escudé, A. D. Montero-Dorta, F. Montesano, D. Muna, A. D. Myers, T. Naugle, R. C. Nichol, P. Noterdaeme,

S. E. Nuza, M. D. Olmstead, A. Oravetz, D. J. Oravetz, R. Owen, N. Padmanabhan, N. Palanque-Delabrouille, K. Pan, J. K. Parejko, I. Pâris, W. J. Percival, I. Pérez-Fournon, I. Pérez-Ràfols, P. Petitjean, R. Pfaffenberger, J. Pforr, M. M. Pieri, F. Prada, A. M. Price-Whelan, M. J. Raddick, R. Rebolo, J. Rich, G. T. Richards, C. M. Rockosi, N. A. Roe, A. J. Ross, N. P. Ross, G. Rossi, J. A. Rubiño-Martin, L. Samushia, A. G. Sánchez, C. Sayres, S. J. Schmidt, D. P. Schneider, C. G. Scóccola, H.-J. Seo, A. Shelden, E. Sheldon, Y. Shen, Y. Shu, A. Slosar, S. A. Smee, S. A. Snedden, F. Stauffer, O. Steele, M. A. Strauss, A. Streblyanska, N. Suzuki, M. E. C. Swanson, T. Tal, M. Tanaka, D. Thomas, J. L. Tinker, R. Tojeiro, C. A. Tremonti, M. Vargas Magaña, L. Verde, M. Viel, D. A. Wake, M. Watson, B. A. Weaver, D. H. Weinberg, B. J. Weiner, A. A. West, M. White, W. M. Wood-Vasey, C. Yeche, I. Zehavi, G.-B. Zhao, and Z. Zheng. The Baryon Oscillation Spectroscopic Survey of SDSS-III. *AJ*, 145:10, January 2013. doi: 10.1088/0004-6256/145/1/10.

[48] A. J. S. Hamilton. Measuring Omega and the real correlation function from the redshift correlation function. *ApJ*, 385:L5–L8, January 1992. doi: 10.1086/186264.

[49] N. Palanque-Delabrouille, C. Yèche, A. Borde, J.-M. Le Goff, G. Rossi, M. Viel, É. Aubourg, S. Bailey, J. Bautista, M. Blomqvist, A. Bolton, J. S. Bolton, N. G. Busca, B. Carithers, R. A. C. Croft, K. S. Dawson, T. Delubac, A. Font-Ribera, S. Ho, D. Kirkby, K.-G. Lee, D. Margala, J. Miralda-Escudé, D. Muna, A. D. Myers, P. Noterdaeme, I. Pâris, P. Petitjean, M. M. Pieri, J. Rich, E. Rollinde, N. P. Ross, D. J. Schlegel, D. P. Schneider, A. Slosar, and D. H. Weinberg. The one-dimensional Lyα forest power spectrum from BOSS. *A&A*, 559:A85, November 2013. doi: 10.1051/0004-6361/201322130.

[50] A. M. Hopkins and J. F. Beacom. On the Normalization of the Cosmic Star Formation History. *ApJ*, 651:142–154, November 2006. doi: 10.1086/506610.

[51] M. Rauch, M. G. Haehnelt, and M. Steinmetz. QSO Metal Absorption Systems at High Redshift and the Signature of Hierarchical Galaxy Formation. *ApJ*, 481: 601–624, May 1997. doi: 10.1086/304085.

[52] A. Boksenberg and W. L. W. Sargent. Properties of QSO Metal-line Absorption Systems at High Redshifts: Nature and Evolution of the Absorbers and New Evidence on Escape of Ionizing Radiation from Galaxies. *ApJS*, 218:7, May 2015. doi: 10.1088/0067-0049/218/1/7.

[53] S. Vikas, W. M. Wood-Vasey, B. Lundgren, N. P. Ross, A. D. Myers, Y. AlSayyad, D. G. York, D. P. Schneider, J. Brinkmann, D. Bizyaev, H. Brewington, J. Ge, E. Malanushenko, V. Malanushenko, D. Muna, D. Oravetz, K. Pan, I. Pâris, P. Petitjean, S. Snedden, A. Shelden, A. Simmons, and B. A. Weaver. Moderate C IV

Absorber Systems Require 10^{12} M Dark Matter Halos at z ˜ 2.3: A Cross-correlation Study of C IV Absorber Systems and Quasars in SDSS-III BOSS DR9. *ApJ*, 768: 38, May 2013. doi: 10.1088/0004-637X/768/1/38.

[54] B. Lundgren, Y. AlSayyad, J. Ge, F. W. Hamann, B. Ménard, J. Miralda, A. D. Myers, I. Paris, I. P. i. Rafols, P. Petitjean, M. Pieri, N. Ross, D. P. Schneider, J. Tinker, S. K. Vikas, D. Wake, W. M. Wood-Vasey, D. G. York, G. Zhu, and SDSS-III BOSS Collaboration. The Clustering and Evolution of Mg II and C IV Absorption Systems in the BOSS Quasar Spectra. In *American Astronomical Society Meeting Abstracts #221*, volume 221 of *American Astronomical Society Meeting Abstracts*, page 402.05, January 2013.

[55] J. N. Bahcall and L. Spitzer, Jr. Absorption Lines Produced by Galactic Halos. *ApJ*, 156:L63, May 1969. doi: 10.1086/180350.

[56] R. Lynds. The Absorption-Line Spectrum of 4c 05.34. *ApJ*, 164:L73, March 1971. doi: 10.1086/180695.

[57] W. L. W. Sargent, P. J. Young, A. Boksenberg, and D. Tytler. The distribution of Lyman-alpha absorption lines in the spectra of six QSOs - Evidence for an intergalactic origin. *ApJS*, 42:41–81, January 1980. doi: 10.1086/190644.

[58] M. Rauch. The Lyman Alpha Forest in the Spectra of QSOs. *ARA&A*, 36:267–316, 1998. doi: 10.1146/annurev.astro.36.1.267.

[59] T. Delubac, J. E. Bautista, N. G. Busca, J. Rich, D. Kirkby, S. Bailey, A. Font-Ribera, A. Slosar, K.-G. Lee, M. M. Pieri, J.-C. Hamilton, É. Aubourg, M. Blomqvist, J. Bovy, J. Brinkmann, W. Carithers, K. S. Dawson, D. J. Eisenstein, S. G. A. Gontcho, J.-P. Kneib, J.-M. Le Goff, D. Margala, J. Miralda-Escudé, A. D. Myers, R. C. Nichol, P. Noterdaeme, R. O'Connell, M. D. Olmstead, N. Palanque-Delabrouille, I. Pâris, P. Petitjean, N. P. Ross, G. Rossi, D. J. Schlegel, D. P. Schneider, D. H. Weinberg, C. Yèche, and D. G. York. Baryon acoustic oscillations in the Lyα forest of BOSS DR11 quasars. *A&A*, 574:A59, February 2015. doi: 10.1051/0004-6361/201423969.

[60] Michael Blomqvist, David Kirkby, Julian E. Bautista, Andreu Arinyo i Prats, NicolÃąs G. Busca, Jordi Miralda-EscudÃľ, AnÅ¿e Slosar, Andreu Font-Ribera, Daniel Margala, Donald P. Schneider, and Jose A. Vazquez. Boradband distortion modeling in Lyman-α forest BAO fitting. *J. Cosmology Astropart. Phys.*, 2015:034, November 2015. doi: 10.1088/1475-7516/2015/11/034. URL http://stacks.iop.org/1475-7516/2015/i=11/a=034.

[61] J. E. Bautista, N. G. Busca, J. Guy, J. Rich, M. Blomqvist, H. du Mas des Bourboux, M. M. Pieri, A. Font-Ribera, S. Bailey, T. Delubac, D. Kirkby, J.-M. Le Goff, D. Margala, A. Slosar, J. A. Vazquez, J. R. Brownstein, K. S. Dawson, D. J. Eisenstein, J. Miralda-Escudé, P. Noterdaeme, N. Palanque-Delabrouille, I. Pâris, P. Petitjean, N. P. Ross, D. P. Schneider, D. H. Weinberg, and C. Yèche. Measurement of BAO correlations at $z = 2.3$ with SDSS DR12 \lya-Forests. *ArXiv e-prints*, February 2017.

[62] H. du Mas des Bourboux and co-authors. Measurement of the baryon acoustic oscillations correlation at $z = 2.40$ with BOSS DR12 from the LyA-forest - quasar cross-correlation. *in prep*, 2017.

[63] S. Alam, F. D. Albareti, C. Allende Prieto, F. Anders, S. F. Anderson, T. Anderton, B. H. Andrews, E. Armengaud, É. Aubourg, S. Bailey, and et al. The Eleventh and Twelfth Data Releases of the Sloan Digital Sky Survey: Final Data from SDSS-III. *ApJS*, 219:12, July 2015. doi: 10.1088/0067-0049/219/1/12.

[64] A. S. Bolton, D. J. Schlegel, É. Aubourg, S. Bailey, V. Bhardwaj, J. R. Brownstein, S. Burles, Y.-M. Chen, K. Dawson, D. J. Eisenstein, J. E. Gunn, G. R. Knapp, C. P. Loomis, R. H. Lupton, C. Maraston, D. Muna, A. D. Myers, M. D. Olmstead, N. Padmanabhan, I. Pâris, W. J. Percival, P. Petitjean, C. M. Rockosi, N. P. Ross, D. P. Schneider, Y. Shu, M. A. Strauss, D. Thomas, C. A. Tremonti, D. A. Wake, B. A. Weaver, and W. M. Wood-Vasey. Spectral Classification and Redshift Measurement for the SDSS-III Baryon Oscillation Spectroscopic Survey. *AJ*, 144:144, November 2012. doi: 10.1088/0004-6256/144/5/144.

[65] J. E. Gunn, M. Carr, C. Rockosi, M. Sekiguchi, K. Berry, B. Elms, E. de Haas, Ž. Ivezić, G. Knapp, R. Lupton, G. Pauls, R. Simcoe, R. Hirsch, D. Sanford, S. Wang, D. York, F. Harris, J. Annis, L. Bartozek, W. Boroski, J. Bakken, M. Haldeman, S. Kent, S. Holm, D. Holmgren, D. Petravick, A. Prosapio, R. Rechenmacher, M. Doi, M. Fukugita, K. Shimasaku, N. Okada, C. Hull, W. Siegmund, E. Mannery, M. Blouke, D. Heidtman, D. Schneider, R. Lucinio, and J. Brinkman. The Sloan Digital Sky Survey Photometric Camera. *AJ*, 116:3040–3081, December 1998. doi: 10.1086/300645.

[66] M. Fukugita, T. Ichikawa, J. E. Gunn, M. Doi, K. Shimasaku, and D. P. Schneider. The Sloan Digital Sky Survey Photometric System. *AJ*, 111:1748, April 1996. doi: 10.1086/117915.

[67] J. E. Gunn, W. A. Siegmund, E. J. Mannery, R. E. Owen, C. L. Hull, R. F. Leger, L. N. Carey, G. R. Knapp, D. G. York, W. N. Boroski, S. M. Kent, R. H. Lupton, C. M. Rockosi, M. L. Evans, P. Waddell, J. E. Anderson, J. Annis, J. C.

Barentine, L. M. Bartoszek, S. Bastian, S. B. Bracker, H. J. Brewington, C. I. Briegel, J. Brinkmann, Y. J. Brown, M. A. Carr, P. C. Czarapata, C. C. Drennan, T. Dombeck, G. R. Federwitz, B. A. Gillespie, C. Gonzales, S. U. Hansen, M. Harvanek, J. Hayes, W. Jordan, E. Kinney, M. Klaene, S. J. Kleinman, R. G. Kron, J. Kresinski, G. Lee, S. Limmongkol, C. W. Lindenmeyer, D. C. Long, C. L. Loomis, P. M. McGehee, P. M. Mantsch, E. H. Neilsen, Jr., R. M. Neswold, P. R. Newman, A. Nitta, J. Peoples, Jr., J. R. Pier, P. S. Prieto, A. Prosapio, C. Rivetta, D. P. Schneider, S. Snedden, and S.-i. Wang. The 2.5 m Telescope of the Sloan Digital Sky Survey. *AJ*, 131:2332–2359, April 2006. doi: 10.1086/500975.

[68] D. G. York, J. Adelman, J. E. Anderson, Jr., S. F. Anderson, J. Annis, N. A. Bahcall, J. A. Bakken, R. Barkhouser, S. Bastian, E. Berman, W. N. Boroski, S. Bracker, C. Briegel, J. W. Briggs, J. Brinkmann, R. Brunner, S. Burles, L. Carey, M. A. Carr, F. J. Castander, B. Chen, P. L. Colestock, A. J. Connolly, J. H. Crocker, I. Csabai, P. C. Czarapata, J. E. Davis, M. Doi, T. Dombeck, D. Eisenstein, N. Ellman, B. R. Elms, M. L. Evans, X. Fan, G. R. Federwitz, L. Fiscelli, S. Friedman, J. A. Frieman, M. Fukugita, B. Gillespie, J. E. Gunn, V. K. Gurbani, E. de Haas, M. Haldeman, F. H. Harris, J. Hayes, T. M. Heckman, G. S. Hennessy, R. B. Hindsley, S. Holm, D. J. Holmgren, C.-h. Huang, C. Hull, D. Husby, S.-I. Ichikawa, T. Ichikawa, Ž. Ivezić, S. Kent, R. S. J. Kim, E. Kinney, M. Klaene, A. N. Kleinman, S. Kleinman, G. R. Knapp, J. Korienek, R. G. Kron, P. Z. Kunszt, D. Q. Lamb, B. Lee, R. F. Leger, S. Limmongkol, C. Lindenmeyer, D. C. Long, C. Loomis, J. Loveday, R. Lucinio, R. H. Lupton, B. MacKinnon, E. J. Mannery, P. M. Mantsch, B. Margon, P. McGehee, T. A. McKay, A. Meiksin, A. Merelli, D. G. Monet, J. A. Munn, V. K. Narayanan, T. Nash, E. Neilsen, R. Neswold, H. J. Newberg, R. C. Nichol, T. Nicinski, M. Nonino, N. Okada, S. Okamura, J. P. Ostriker, R. Owen, A. G. Pauls, J. Peoples, R. L. Peterson, D. Petravick, J. R. Pier, A. Pope, R. Pordes, A. Prosapio, R. Rechenmacher, T. R. Quinn, G. T. Richards, M. W. Richmond, C. H. Rivetta, C. M. Rockosi, K. Ruthmansdorfer, D. Sandford, D. J. Schlegel, D. P. Schneider, M. Sekiguchi, G. Sergey, K. Shimasaku, W. A. Siegmund, S. Smee, J. A. Smith, S. Snedden, R. Stone, C. Stoughton, M. A. Strauss, C. Stubbs, M. SubbaRao, A. S. Szalay, I. Szapudi, G. P. Szokoly, A. R. Thakar, C. Tremonti, D. L. Tucker, A. Uomoto, D. Vanden Berk, M. S. Vogeley, P. Waddell, S.-i. Wang, M. Watanabe, D. H. Weinberg, B. Yanny, N. Yasuda, and SDSS Collaboration. The Sloan Digital Sky Survey: Technical Summary. *AJ*, 120:1579–1587, September 2000. doi: 10.1086/301513.

[69] Isabelle Pâris et al. The Sloan Digital Sky Survey Quasar Catalog: twelfth data release. *Astron. Astrophys.*, 597:A79, 2017. doi: 10.1051/0004-6361/201527999.

[70] N. P. Ross, A. D. Myers, E. S. Sheldon, C. Yèche, M. A. Strauss, J. Bovy, J. A. Kirkpatrick, G. T. Richards, É. Aubourg, M. R. Blanton, W. N. Brandt, W. C. Carithers, R. A. C. Croft, R. da Silva, K. Dawson, D. J. Eisenstein, J. F. Hennawi, S. Ho, D. W. Hogg, K.-G. Lee, B. Lundgren, R. G. McMahon, J. Miralda-Escudé, N. Palanque-Delabrouille, I. Pâris, P. Petitjean, M. M. Pieri, J. Rich, N. A. Roe, D. Schiminovich, D. J. Schlegel, D. P. Schneider, A. Slosar, N. Suzuki, J. L. Tinker, D. H. Weinberg, A. Weyant, M. White, and W. M. Wood-Vasey. The SDSS-III Baryon Oscillation Spectroscopic Survey: Quasar Target Selection for Data Release Nine. *ApJS*, 199:3, March 2012. doi: 10.1088/0067-0049/199/1/3.

[71] G. T. Richards, A. D. Myers, A. G. Gray, R. N. Riegel, R. C. Nichol, R. J. Brunner, A. S. Szalay, D. P. Schneider, and S. F. Anderson. Efficient Photometric Selection of Quasars from the Sloan Digital Sky Survey. II. ˜1,000,000 Quasars from Data Release 6. *ApJS*, 180:67–83, January 2009. doi: 10.1088/0067-0049/180/1/67.

[72] J. A. Kirkpatrick, D. J. Schlegel, N. P. Ross, A. D. Myers, J. F. Hennawi, E. S. Sheldon, D. P. Schneider, and B. A. Weaver. A Simple Likelihood Method for Quasar Target Selection. *ApJ*, 743:125, December 2011. doi: 10.1088/0004-637X/743/2/125.

[73] C. Yèche, P. Petitjean, J. Rich, E. Aubourg, N. Busca, J.-C. Hamilton, J.-M. Le Goff, I. Paris, S. Peirani, C. Pichon, E. Rollinde, and M. Vargas-Magaña. Artificial neural networks for quasar selection and photometric redshift determination. *A&A*, 523:A14, November 2010. doi: 10.1051/0004-6361/200913508.

[74] J. Bovy, J. F. Hennawi, D. W. Hogg, A. D. Myers, J. A. Kirkpatrick, D. J. Schlegel, N. P. Ross, E. S. Sheldon, I. D. McGreer, D. P. Schneider, and B. A. Weaver. Think Outside the Color Box: Probabilistic Target Selection and the SDSS-XDQSO Quasar Targeting Catalog. *ApJ*, 729:141, March 2011. doi: 10.1088/0004-637X/729/2/141.

[75] I. Pâris, P. Petitjean, É. Aubourg, S. Bailey, N. P. Ross, A. D. Myers, M. A. Strauss, S. F. Anderson, E. Arnau, J. Bautista, D. Bizyaev, A. S. Bolton, J. Bovy, W. N. Brandt, H. Brewington, J. R. Browstein, N. Busca, D. Capellupo, W. Carithers, R. A. C. Croft, K. Dawson, T. Delubac, G. Ebelke, D. J. Eisenstein, P. Engelke, X. Fan, N. Filiz Ak, H. Finley, A. Font-Ribera, J. Ge, R. R. Gibson, P. B. Hall, F. Hamann, J. F. Hennawi, S. Ho, D. W. Hogg, Ž. Ivezić, L. Jiang, A. E. Kimball, D. Kirkby, J. A. Kirkpatrick, K.-G. Lee, J.-M. Le Goff, B. Lundgren, C. L. MacLeod, E. Malanushenko, V. Malanushenko, C. Maraston, I. D. McGreer, R. G. McMahon, J. Miralda-Escudé, D. Muna, P. Noterdaeme, D. Oravetz, N. Palanque-Delabrouille, K. Pan, I. Perez-Fournon, M. M. Pieri, G. T. Richards, E. Rollinde, E. S. Sheldon,

D. J. Schlegel, D. P. Schneider, A. Slosar, A. Shelden, Y. Shen, A. Simmons, S. Snedden, N. Suzuki, J. Tinker, M. Viel, B. A. Weaver, D. H. Weinberg, M. White, W. M. Wood-Vasey, and C. Yèche. The Sloan Digital Sky Survey quasar catalog: ninth data release. *A&A*, 548:A66, December 2012. doi: 10.1051/0004-6361/201220142.

[76] I. Pâris, P. Petitjean, É. Aubourg, N. P. Ross, A. D. Myers, A. Streblyanska, S. Bailey, P. B. Hall, M. A. Strauss, S. F. Anderson, D. Bizyaev, A. Borde, J. Brinkmann, J. Bovy, W. N. Brandt, H. Brewington, J. R. Brownstein, B. A. Cook, G. Ebelke, X. Fan, N. Filiz Ak, H. Finley, A. Font-Ribera, J. Ge, F. Hamann, S. Ho, L. Jiang, K. Kinemuchi, E. Malanushenko, V. Malanushenko, M. Marchante, I. D. McGreer, R. G. McMahon, J. Miralda-Escudé, D. Muna, P. Noterdaeme, D. Oravetz, N. Palanque-Delabrouille, K. Pan, I. Perez-Fournon, M. Pieri, R. Riffel, D. J. Schlegel, D. P. Schneider, A. Simmons, M. Viel, B. A. Weaver, W. M. Wood-Vasey, C. Yèche, and D. G. York. The Sloan Digital Sky Survey quasar catalog: tenth data release. *A&A*, 563:A54, March 2014. doi: 10.1051/0004-6361/201322691.

[77] R. J. Weymann, S. L. Morris, C. B. Foltz, and P. C. Hewett. Comparisons of the emission-line and continuum properties of broad absorption line and normal quasi-stellar objects. *ApJ*, 373:23–53, May 1991. doi: 10.1086/170020.

[78] K. L. Cooksey, M. M. Kao, R. A. Simcoe, J. M. O'Meara, and J. X. Prochaska. Precious Metals in SDSS Quasar Spectra. I. Tracking the Evolution of Strong, 1.5 $<$ z $<$ 4.5 C IV Absorbers with Thousands of Systems. *ApJ*, 763:37, January 2013. doi: 10.1088/0004-637X/763/1/37.

[79] Pierre Laurent et al. A 14 h^{-3} Gpc^3 study of cosmic homogeneity using BOSS DR12 quasar sample. *JCAP*, 1611(11):060, 2016. doi: 10.1088/1475-7516/2016/11/060.

[80] V. D'Odorico, F. Calura, S. Cristiani, and M. Viel. The rise of the CIV mass density at z $=<$ 2.5. *MNRAS*, 401:2715–2721, February 2010. doi: 10.1111/j.1365-2966.2009.15856.x.

[81] L. Mas-Ribas, J. Miralda-Escudé, I. Pérez-Ràfols, A. Arinyo-i-Prats, P. Noterdaeme, P. Petitjean, D. P. Schneider, D. G. York, and J. Ge. The Mean Metal-line Absorption Spectrum of Damped Lyman Alpha Systems in BOSS. *ArXiv e-prints*, October 2016.

[82] P. Dirac. *General Theory of Relativity.* Princeton University Press, 1996.

[83] A. Lichnerowicz. *Elements de calcul tensoriel.* Armand Colin, 1955.

[84] R. DâĂŹInverno. *Introducing EinsteinâĂŹs Relativity.* Clarendon Press, 1992.

[85] E. W. Kolb and M. S. Turner. *The Early Universe.* Westview, 1994. ISBN 0201116030.